Learning-based Control and Sensing for Soft Robotic Systems

by

Justin Di-Lang Ho

A thesis submitted in partial fulfillment of the requirements
for the degree of Master of Philosophy
at The University of Hong Kong

September 2019

Abstract of thesis entitled

Learning-based Control and Sensing for Soft Robotic Systems

Submitted by

Justin Di-Lang Ho

for the degree of Master of Philosophy

at the University of Hong Kong

September 2019

The recent emergence of soft robotics has led to exciting developments in the robotics field. Soft robots are inherently compliant and manoeuvrable manipulators that can passively adapt to their environment - traits previously unseen in rigid-link robots. Researchers saw potential applications in areas such as minimally invasive surgery, rehabilitation, search and rescue, and underwater robotics. However, as with any emergent field, many new challenges arise in the investigation of their unique traits and how to best apply them. This thesis aims to investigate methods to tackle challenges specifically in the control and sensing of soft and flexible robotic systems.

Soft robots excel in unstructured and unpredictable environments, in thanks to their compliant and adaptable nature, however, this often comes at the cost of precise control and predictability of the system. In order to fully make use of their unique properties, accurate control should still be maintained while affected by the environment. Commonly used model-based approaches often have low tolerance to unmodelled loading, resulting in significant error when acted on by them. Therefore, in this first study we employ a nonparametric learning-based method that can approximate and update the inverse model of a redundant two-segment soft robot in an online manner. The primary contribution of this work is the application and evaluation of the proposed framework on a redundant soft robot. With the addition of redundancy, a constrained optimisation approach is taken to consistently resolve null-space behaviour. Through this control framework, the controller

can continuously adapt to unknown external disturbances during runtime and maintain end-effector accuracy. The performance of the control framework was evaluated by tracking of a 3D trajectory with a static tip load, and a variable weight tip load. The results indicate that the proposed controller could effectively adapt to the disturbances and continue to track the desired trajectory accurately.

In a following study, a general framework for the design, fabrication, and modelling of soft and flexible surface shape sensor was presented. A prototype surface shape sensor using a single FBG optical fibre was developed and its performance experimentally validated. The single-core optical fibre with fibre Bragg gratings (FBGs) is capable of detecting sparse local strains at high bandwidth using the wavelength-division multiplexing (WDM) interrogation method. The fibre was embedded into an elastomeric substrate to reconstruct its global surface morphology. Finite element analysis (FEA) was used to determine the design parameters and to validate the unique mapping from sparse strain measurements to the continuum shape of the sensor. To simplify the fabrication and error compensation process without precise/prior knowledge of the FBG locations in the sensor, machine learning-based modelling was applied. This enables real-time, robust and reliable shape reconstruction. It is demonstrated to outperform various applications of electronics-based sensors which require sophisticated electrode wiring and calibration. Experiments were performed to evaluate the sensing accuracy and repeatability. In a final study, 3D shape reconstruction of a multi-core optical fibre was conducted. Preliminary experimental evaluation of bending curvature and bending direction was performed.

(492 words)

Declaration

I hereby declare that this whole dissertation titled *Learning-based Control and Sensing for Soft Robotic Systems* is my own work, except the parts with due acknowledgement, and that it has not been previously included in a thesis, dissertation or report submitted to this University or to any other institution for a degree, diploma or other qualifications.

Signed: _____

Justin Di-Lang Ho

Acknowledgements

It felt like only yesterday when I'd finished my undergraduate degree and made the big move to Hong Kong to pursue a M.Phil. Now, after the blink of an eye, three years have passed, and I'm about to graduate with a handful of papers and bucketful of late nights in the lab under my belt. These last three years have been intense, exciting, and extremely rewarding. I wouldn't have made it through without the help of my mentors, peers, and a few too many cups of coffee.

To start with, I would like to thank my supervisor and mentor Dr. Ka-Wai Kwok. Throughout these three years he has taught me infinitely more than what I could have imagined before joining his lab. I'm deeply grateful for his patience, wisdom, and immense enthusiasm. I would also like to thank my co-supervisor, Professor James Lam, for his great support.

To all my colleagues in the lab past and present, I have to say a massive thank you. Whether it's teaching me Cantonese slang, how a Kalman filter works, or blowing water during long nights at the lab, your support and comradery made my research experience an unforgettable one.

Lastly, I have to thank my parents, my family in Hong Kong, and my girlfriend Gigi for their unwavering support. Your care and guidance are what made this entire journey possible.

Table of Contents

List of Figures

List of Tables

List of Abbreviations

3D	Three Dimensional
ANN	Artificial Neural Network
BBR	Broadband Reflectors
DOF	Degrees of Freedom
DTG	Draw Tower Gratings
eGaIn	Eutectic Gallium Indium
EM	Electromagnetic
FBG	Fibre Bragg Grating
FEA	Finite Element Analysis
FNN	Feedforward Neural Network
MEMS	Microelectromechanical Systems
NN	Neural Network
OFDR	Optical Frequency Domain Reflectometry
PCC	Piecewise Constant Curvature
RMSe	Root Mean Square Error
RTV	Room Temperature Vulcanisation
SLA	Stereolithography Apparatus
SNR	Signal-to-Noise Ratio
WDM	Wavelength Division Multiplexing

CHAPTER 1
INTRODUCTION

1.1 MOTIVATION AND OBJECTIVES

The emergence of soft robotics in recent years has been an exciting development for the robotics field. Their inherent simplicity, flexibility, and ability to passively adapt to their environment are traits that were unseen in traditional rigid-link robots. Researchers saw potential applications in fields such as minimally invasive surgery, rehabilitation, search and rescue, and underwater robotics. But as with any emergent field such as soft robotics, many new challenges arise in the investigation of their unique traits and how to best apply them.

The modelling and control of soft robotics is a challenging task due to their inherent material properties. A key benefit of soft robotics is their ability to passively conform to their surroundings, however, to maintain accurate control while doing so is still a fundamental challenge. Analytical models generally provide the basis for accurate control in rigid robots, however the analogue for soft robots can be overly complex as a result of their non-linear elasticity and typical fluidic actuation. Current analytical approaches for soft robotics often come with major generalisations of the robot behaviour and quickly become invalidated in the case of contact with the environment. In other cases, they can be impractical to apply in real-time feedback control due to their computational intensity.

Sensing is also a highly challenging area in soft robotics, as traditional encoders and other rigid sensors are impractical to implement on soft-bodied structures. Taking advantage of their mechanical compliance, open-loop control is commonplace in soft robotics. Alternatively, some are controlled with feedback using indirect variables such as actuation pressure that do not take into account the true robot posture. Although sensors have been developed for the purpose of monitoring soft robots, few are easily integrated due to size, reliance on external sensing, or cumbersome wiring.

The objective of this work is to investigate solutions in the modelling and control of soft robots under external disturbance, and to address shortcomings in current soft sensor. The primary contributions of this work are as follows:

Modelling and control

- Design and implementation of a general learning-based framework, which enables robust control of a multi-segment soft continuum robot by adapting to unmodelled loading via online learning.
- Consistent resolution of null-space behaviour, which can resist variable distributions of sampled learning data.
- Experimental validation of the proposed controller, which evaluates the performance of a six-chamber continuum robot while following a 3-D trajectory with the addition of an unmodelled, variable weight tip load.

Soft sensing

- Development of a design framework for FBG-based surface morphology sensors. A single-core optical fibre with sparsely distributed FBGs was used to detect surface morphology in real-time.
- FEA to determine sensor design parameters with embedded FBGs. The mapping between surface deformation and fibre responses were proven to be unique for the proposed fibre layout.
- Machine learning-based modelling to enable more robust and reliable shape reconstruction without explicit knowledge of the FBG configuration/allocation.
- Preliminary experimental validation of 3D shape sensing using a multi-core fibre.

1.2 THESIS ORGANISATION

Chapter 2 presents a novel study into the modelling and control of a redundant soft manipulator while under the effect of external disturbance. The chapter begins with a review of current modelling and control approaches for soft robotics, followed by the design, implementation, and validation of a learning-based framework that enables improved 3D trajectory following accuracy while under the effect of different tip loading. The work is based on the first-authored paper "*Localised Online Learning-Based Control of a Soft Redundant Manipulator Under Variable Loading*".

Chapter 3 is composed of two sections. The first focuses on the development of a soft surface shape sensor that leverages finite-element modelling and machine learning. In this work, a single-core fibre with sparsely distributed fibre Bragg gratings (FBGs) is used to reconstruct dense information of the substrate's surface. The second section is an initial investigation into 3D shape sensing using a multi-core fibre with FBGs. A shape reconstruction algorithm was implemented with preliminary experimental evaluation conducted. The first section of this work is based on the Co-first-authored paper "*Real-time Surface Shape Sensing for Soft and Flexible Structures using Fiber Bragg Gratings*".

Chapter 4 provides concluding statements of the thesis as a whole and touches on future research directions.

1.3 PUBLICATIONS IN STUDY PERIOD

1.3.1 First-authored papers

1) J. D.L. Ho, K.H. Lee, W.L. Tang, K.M. Hui, K. Althoefer, J. Lam, and K.W. Kwok, "*Localised Online Learning-Based Control of a Soft Redundant Manipulator Under Variable Loading*", **Advanced Robotics**, 2018.
(DOI: 10.1080/01691864.2018.1528178)

2) T.L.T. Lun*, K. Wang*, J. D.L. Ho*, K.H. Lee, K.Y. Sze, and K.W. Kwok, "*Real-time Surface Shape Sensing for Soft and Flexible Structures using Fiber Bragg Gratings*", **IEEE Robotics and Automation Letters (RA-L)**, 2019.
(DOI: 10.1109/LRA.2019.2893036)
*Co-first authors (My primary contributions in this publication were in experimental setup, experimental validation, and general manuscript writing)

1.3.2 Co-authored papers

3) G. Fang, X. Wang, K. Wang, K.H. Lee, J. D.L. Ho, H.C. Fu, D.K.C. Fu, and K.W. Kwok, "*Vision-based Online Learning Kinematic Control for Soft Robots using Local Gaussian Process Regression*", **IEEE Robotics and Automation Letters (RA-L)**, 2019.

4) Z. Guo, Z. Dong, K.H. Lee, C.L. Cheung, H.C. Fu, J. D.L. Ho, H. He, W.S. Poon, D.T.M. Chan, K.W. Kwok, "*Compact Design of a Hydraulic Driving Robot for Intra-operative MRI-guided Bilateral Stereotactic Neurosurgery*", **IEEE Robotics and Automation Letters (RA-L)**, vol. 3, no. 3, pp. 2515-2522. 2018.
ICRA Best Conference Paper Award (out of 2,539 papers)
Finalist (out of 3) for the Best Medical Robotics Paper Award

5) H.C. Fu, J. D.L. Ho, K.H. Lee, Y.C. Hu, S. K.W. Au, K.J. Cho, K.Y. Sze, and K.W. Kwok, "*Interfacing Soft and Hard: A Spring Reinforced Actuator*", **Soft Robotics** (In press).

6) C.L. Cheung, J. D.L. Ho, V. Vardhanabhuti, H.C. Chang, and K.W. Kwok, "*Design and Fabrication of Wireless Multilayer Tracking Marker for Intraoperative MRI-guided Interventions*", **IEEE/ASME Transactions on Mechatronics (TMech)** (Reviewed and resubmitted).

7) Z. He, Z. Dong, G. Fang, J. D.L. Ho, C.L. Cheung, H.C. Chang, C.N. Chong, J. Y.K. Chan, D. T.M. Chan, and K.W. Kwok, "*Design of a Percutaneous MRI-guided Needle Robot with Soft Fluid-driven Actuator*", **IEEE Robotics and Automation Letters (RA-L)** (Submitted for review).

8) G. Fang, K. Wang, X. Wang, C.K. Chow, K.H. Lee, J. D.L. Ho, X. Xie, W.L. Tang, L. Liang, H.C. Chang, C.J. Juan, Y.H. Liu, and K.W. Kwok, "*Visual Servoing of MR-safe Soft Manipulator for Transoral Laser Microsurgeries*", **IEEE Robotics and Automation Letters (RA-L)** (Submitted for review).

9) X. Wang, G. Fang, K. Wang, X. Xie, K.H. Lee, J. D.L. Ho, W.L. Tang, J. Lam, and K.W. Kwok, "*Eye-in-hand Visual Servoing Enhanced with Sparse Strain Measurement for Soft Continuum Robots*", **IEEE Robotics and Automation Letters (RA-L)** (Submitted for review).

CHAPTER 2
ONLINE LEARNING-BASED CONTROL OF A SOFT REDUNDANT MANIPULATOR

2.1 INTRODUCTION AND LITERATURE REVIEW

The tentacles of octopus, an elephant's trunk, and even the human tongue are examples of joint-less, soft-bodied limbs that are dextrous manipulators while being compliant and adaptable to their environment [1]. The field of soft robotics can credit its origins to researchers that sought to mimic biological structures for their unique capabilities, resulting in a new class of robots developed with hyper-elastic bodies and embedded with fluidically driven chambers [2-5]. An early example by Wilson *et al.* [6] was inspired by the elephant's trunk and consisted of six polyurethane structures that could each bend in a single direction when pressurised to achieve dextrous manipulation (**Figure 2.1(a)**). Other examples include an actuator that could mimic the degrees of freedom (DOFs) seen in octopus tentacles such as elongation and transverse contraction [7] (**Figure 2.1(b)**), and a ruggedized trunk-like manipulator designed for the object manipulation in the field [8] shown in **Figure 2.1(c)**.

These soft robots are inherently compliant, manoeuvrable and are able to passively adapt to dynamic and unstructured environments. As a result, their prevalence in specialised applications like surgical intervention [9-12] has grown, and has drawn interest

in other fields such as underwater manipulation [7, 13, 14] and search and rescue [15, 16].

Subsequently, the growth of soft robotics field has sparked research focused on modelling the behaviour of soft continuum robots [16-20]. Analytical models capable of offering the forward mapping from robot actuation to its task space generally provide the basis for accurate and dexterous control of conventional, rigid robots. However, the analogue for modelling soft continuum robots can be prohibitively complex due to the non-linear elasticity, compliance and fluidic actuation of the robot body.

Approximations like the piecewise constant curvature (PCC) approach is commonly used to approximate the kinematic mapping of soft robots [16, 17, 21, 22]. The PCC assumption provides a simplified representation of serial-link continuum robots by assuming their segments are smoothly connected with circular bending profiles. In reference to **Figure 2.2**, one bending segment of a soft robot can be defined by the parameters: bending radius, bending angle, and bending direction, which are r, θ, and ϕ, respectively. Although the use of PCC still remains predominant due to its obtainable and closed-form solutions [23, 24], any loading to the robot that results in non-circular bending invalidates the PCC assumption, resulting in significant inaccuracies.

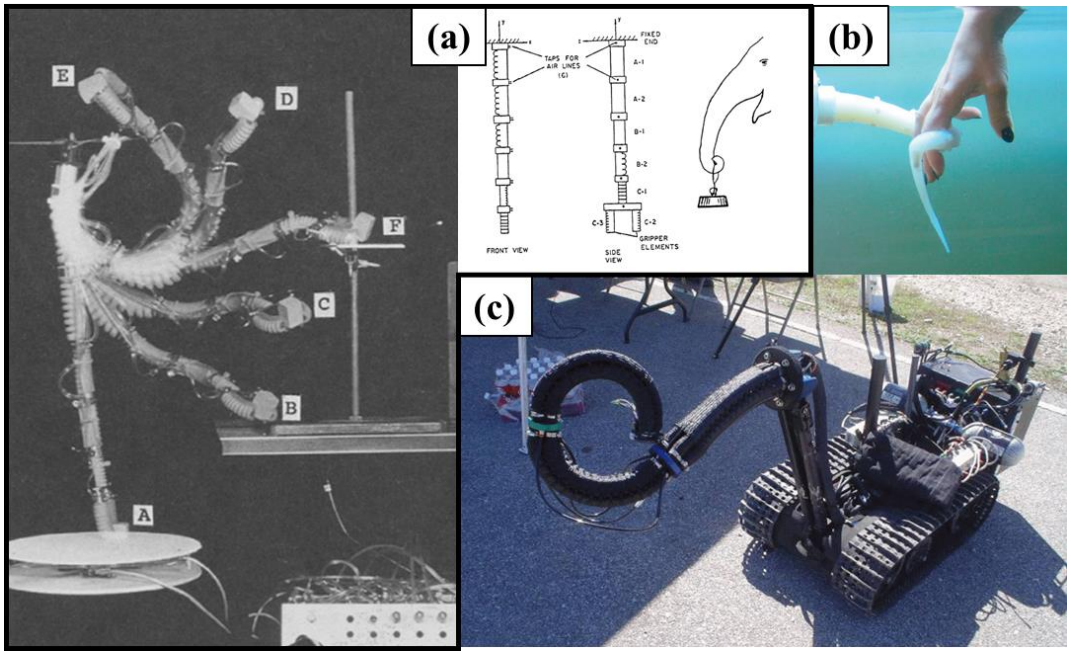

Figure 2.1 Examples of soft robotic actuators inspired by the elephant's trunk and octopus' tentacle. **(a)** An early soft robot developed in 1993 by Wilson *et al.* [6] consisting of 6 serially linked single-DOF actuators. **(b)** A bio-inspired soft robotic tentacle wrapping a hand [7]. **(c)** The OctArm continuum manipulator designed for manipulation in challenging environments [8].

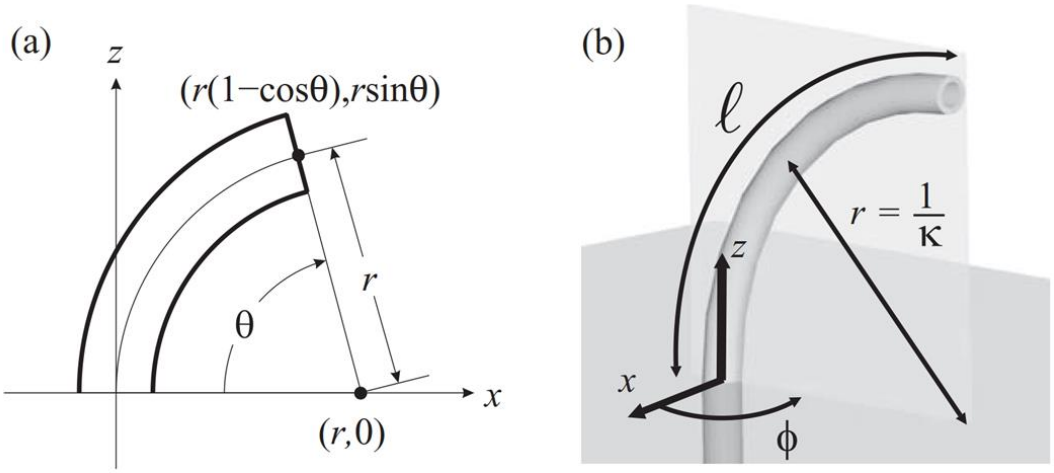

Figure 2.2 Illustration of the piecewise constant curvature approach for modelling soft robots [16], where r is bending radius, θ is bending angle, ϕ is bending direction. **(a)** 2D view when bending direction $\phi = 0$. **(b)** 3D view with neutral axis length indicated by l.

In contrast, other modelling techniques, including those based on the Cosserat rod theory, can take into account external loading such as gravity [25] as well as buoyancy and drag loading due to movement in water [26]. However, these approaches are still too computationally complex to apply in real-time robot control. Fully utilising the conformability and manoeuvrability of soft continuum robots while also maintaining end-effector accuracy is still technically challenging.

A stepping stone towards this goal is through learning-based approaches [18], which have gained popularity in soft robotics because of their ability to bypass the difficulties in modelling uncertain internal and external dynamics. Model-free learning approaches that are adaptive to dynamics present in the robot itself can avoid determining the material and geometrical specifications of the controlled soft robot, as they can be made implicit in the obtained data they learn from. Not only does this allow greater freedom in modifying the robot's structure, but it also provides leeway during construction of the robot, as material inconsistencies within segments and joints can affect bending symmetry and further introduce unmodelled dynamics.

Previously, machine learning-based methods have been used with conventional rigid-link robots, and have been able to approximate their inverse models [27-29], producing results comparable to analytical model-based solutions [30, 31]. Relating to soft continuum robots, a neural network (NN) was applied by Giorelli *et al.* [32] to control a 1-DOF planar soft robotic manipulator, with the study outlining the adaptability of machine-learning approaches to mechanical discrepancies that analytical approaches do not possess. A feedforward NN (FNN) was used to model a relationship between the desired tip position (input) and approximate cable tensions (output), as shown in **Figure 2.3**. The

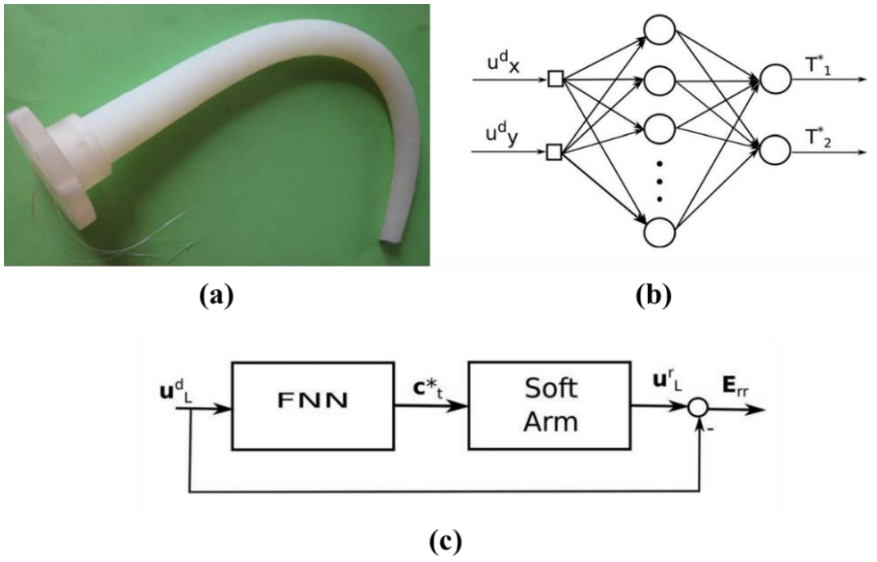

Figure 2.3 **(a)** Tendon-driven soft manipulator with 1-DOF planar bending [33]. **(b)** Feedforward NN (FNN) structure used in place of the Jacobian method. The FNN relates the desired tip positions $\boldsymbol{u}_L^d = (u_x^d, u_y^d)$ to the cable tensions $\boldsymbol{c}_t^* = (T_1^*, T_2^*)$. **(c)** Overview of control scheme.

study provided a useful preliminary application of machine-learning for soft robots, however the adaptability of the algorithm to external loading was not addressed. Another NN-based control was applied to the Festo Robotino® XT hyper-redundant robot [33], with kinematic redundancies taken into account by considering both of the robot's section trajectories. In that study, two NNs were used in tandem to adapt to hysteresis and other modelling uncertainties. However, the kinematic control was computationally intensive, making useful real-time control unfeasible at that stage. A number of other NN-based approaches have been used to learn the inverse kinematics of soft continuum robots [34-36], however the presence of external disturbances were not accounted for in these studies.

Recently, Lee *et al.* [37] proposed a generic control framework based on [30, 38] that is able to directly learn the inverse model of a soft continuum robot for task-space control in an online manner, without knowing the robot's geometric parameters. Finite-element analysis was also used to initialise the learning algorithm to eliminate the need for random exploration [39]. The study applied locally-weighted models in order to estimate the inverse kinematics and control the tip orientation (pitch and yaw) of a single-segment soft manipulator, and was able to maintain tip orientation accuracy even in the presence of unknown loading on the robot body as shown in **Figure 2.4(b)**. In contrast to NN methods, where the model structure is typically determined before the training process, nonparametric regression allows for the optimal model structure to be determined from the training data. Furthermore, the use of such an online learning algorithm allows for rapid updating of the individual local inverse models, which in turn enables adaptation to any change in external loading.

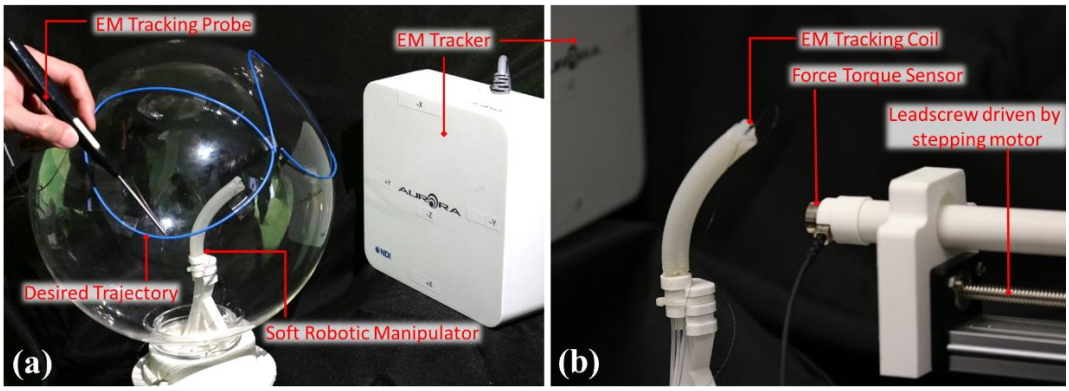

Figure 2.4 In a study by Lee *et al.* [37], a single-segment soft robot was able to compensate for an unmodelled external force with a learning-based approach. **(a)** Registration of the desired trajectory. **(b)** External force applied by a leadscrew and measured with a force sensor.

In this paper, we extend the control framework in [37] to a multi-segment soft continuum robot, also addressing the over-actuated and redundant nature of multiple bending segments. In contrast to the previous study where only the orientation of a single segment actuator was controlled, this study applies 3D positional control to a two-segment actuator. This extension presents the opportunity for more dexterous soft robot tasks, e.g. intraluminal endoscopy, where views behind or around soft-tissue bodies may be otherwise impaired with single segment robots. Workspace exploration is required to train the learning algorithm, with the collection of generated offline pre-training data necessary to learn the proposed controller. Validation of the learned controller is performed through 3D positional trajectory tracking of the soft robot. The primary contributions of this work are as follows:

- Design and implementation of a general learning-based framework, which enables robust control of a multi-segment soft continuum robot by adapting to unmodelled loading via online learning.
- Consistent resolution of null-space behaviour, which can resist variable distributions of sampled learning data.
- Experimental validation of the proposed controller, which evaluates the performance of a six-chamber continuum robot while following a 3-D trajectory with the addition of an unmodeled, variable weight tip load.

2.2 METHODS

2.2.1 Design and Fabrication of a Two-segment Soft Manipulator

The soft robot used in this study is constructed from moulded RTV (Room Temperature Vulcanization) silicone rubber (Dragon Skin 10, Smooth-on Inc.) segments and 3D printed joining components. Each segment comprises of three cylindrical fluidic chambers spaced 120° apart around the section perimeter, with a total of six chambers. Each chamber is constrained radially by a helically wound fibre to limit the chamber expansion to only the axial direction. This facilitates omnidirectional bending of the robot segments when different inflation pressures are provided to each chamber. Each segment can achieve a maximum bending angle of approximately 100° in any direction. An overview of the soft robot and its dimensions is shown in **Figure 2.5**.

The robot is fabricated using a multi-step moulding process wherein the individual air chambers are first moulded separately before combining them in a final mould. The moulds consist of 3D printed parts for forming the outer surface, and metal rods to create hollow channels. The fabrication process for a bending segment consists of the following steps: 1) Moulding of individual air chambers, 2) manual winding of fibre reinforcement around air chambers, 3) moulding of robot segment by encapsulating fibre-reinforced air chambers, 4) demoulding and removal of metal rods. The 3D printed moulds for the air chambers were designed with helical ridges to enforce equal spacing of the fibre reinforcement and increases convenience during manual winding of the thread. A diagram outlining the fabrication process for a bending segment is shown in **Figure 2.6**.

Two bending segments were connected in series by an SLA (stereolithography apparatus) 3D printed coupling, which allows each air tube of the distal (relative to the robot base) segment to feed to the centre cavity of the proximal segment. By using a two-segment soft robot, we have a system with greater dexterity which allows for improved 3D positional control of the tip and presents an opportunity to employ the null-space behaviour to meet a secondary goal. A 3D printed tip is attached to the top of the distal segment to allow mounting of the positional tracking sensor and additional tip loading (static and fluid) as shown in **Figure 2.7**. The bottom of the robot is fixed to a 3D printed base that remains stationary. The outer diameter of the robot is 27 mm and has a total length of 155 mm.

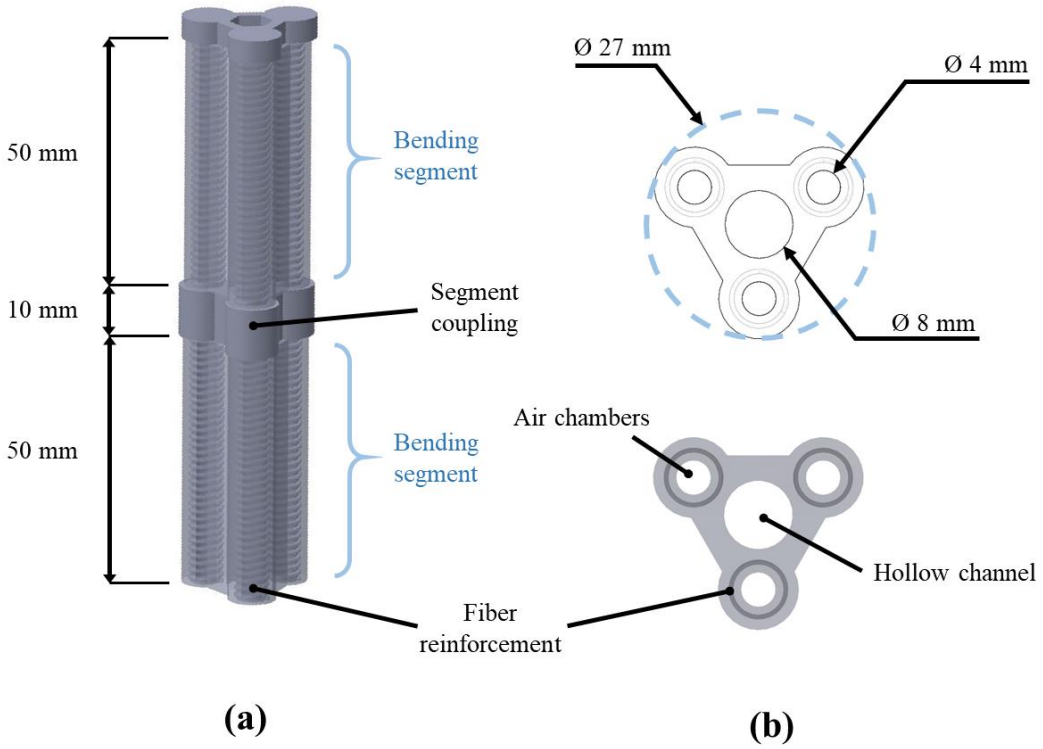

Figure 2.5 Overview of the two-segment soft robot. **(a)** The robot consists of two bending segments connected in series by 3D printed coupling. Six individually actuated air chambers are used to actuate the robot, with three chambers in each bending segment. Threaded fibre reinforces the chambers by restricting radial expansion while allowing elongation. **(b)** Cross section of the bending segment. The air chambers are spaced equally at 120° and provide omnidirectional bending when differential actuation pressures are given. A hollow channel at the centre of the bending segments allow pneumatic tubing of the upper segment to pass through.

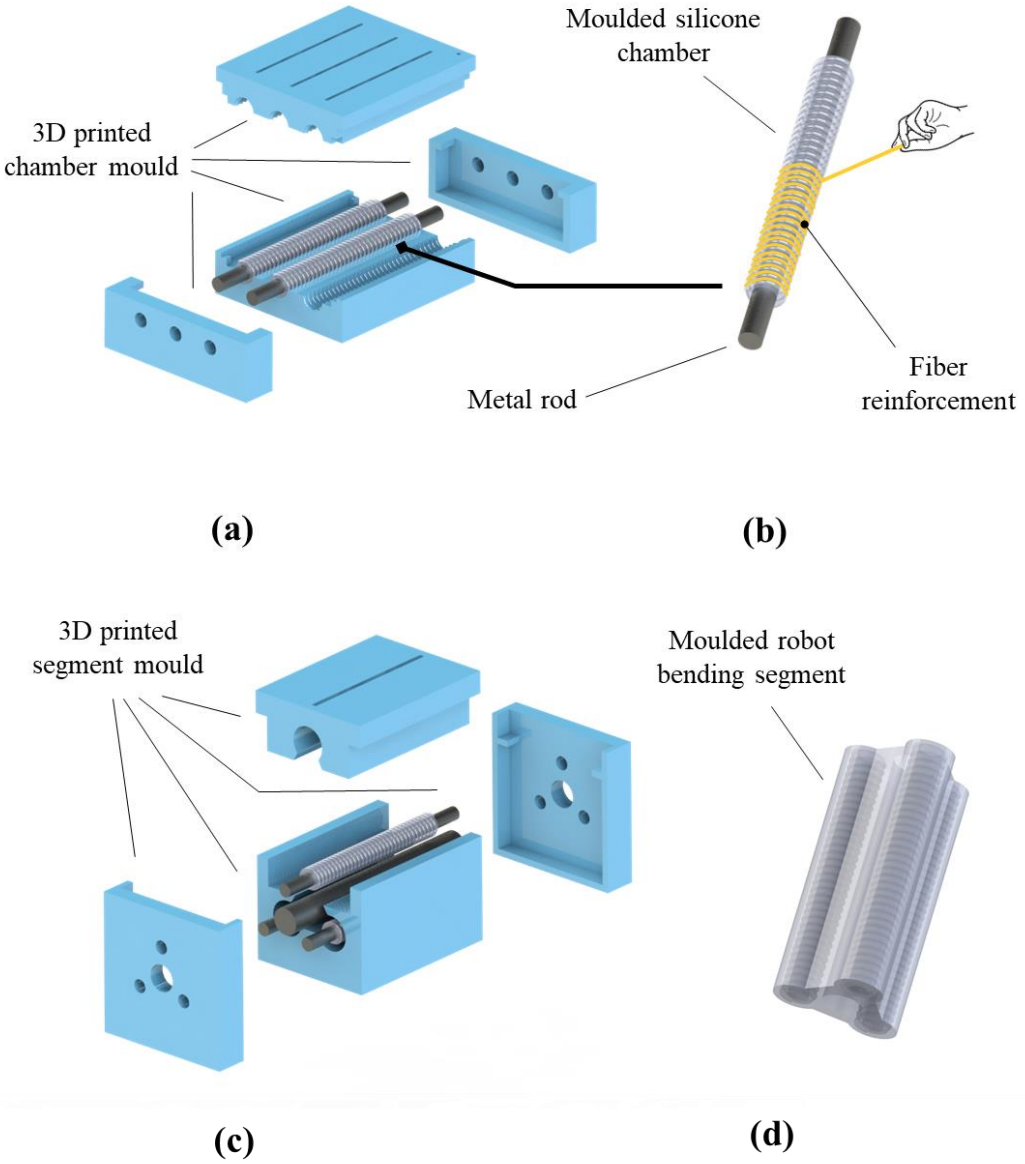

Figure 2.6 Fabrication steps for a single bending segment of the soft robot. **(a)** Individual chambers are moulded around metal rods. **(b)** Fibre reinforcement is manually wound around the moulded silicone chamber. **(c)** Three chambers are combined into a single bending segment through a second mould. **(d)** Metal rods are removed to create hollow channels for actuation and tubing pass-through.

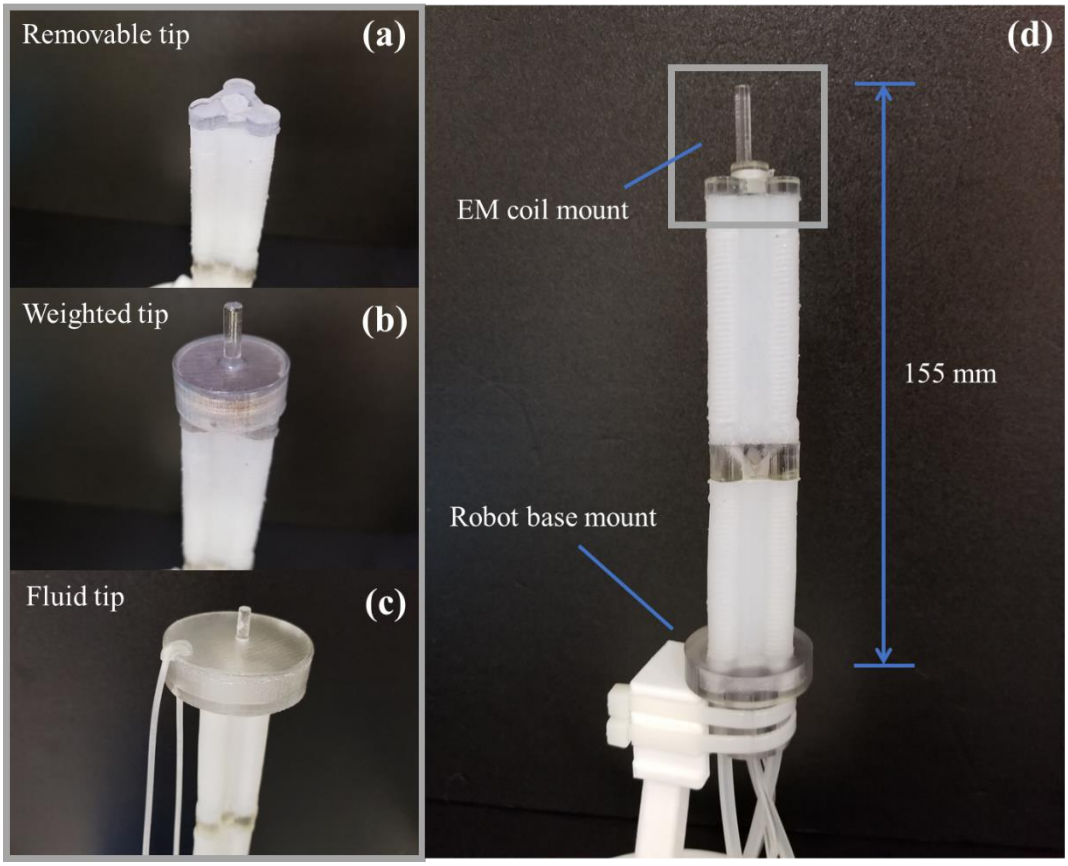

Figure 2.7 **(a)** Plug-in tip allows easy switching to other tip types for experimental validation. **(b)** 14.2 g weighted tip, **(c)** fluid tip weighing 14 g when empty, with maximum weight of 32 g when full of water. **(d)** Soft robotic continuum robot with SLA 3D printed coupling and mounts.

2.2.2 Robot Parameter Definition

To mathematically describe the motion of the robot, we let $u_k \in U$ be the chamber volumes at time step k where U denotes the control space. The distal tip position of the soft robot at equilibrium of the fluidic chambers is represented by the task space coordinate $p_k \in \mathrm{R}^3$. The discrete time transition between robot tip states and chamber volumes within the time step k to $k+1$ is $p_{k+1} = p_k + \Delta p_k$ and $u_{k+1} = u_k + \Delta u_k$, respectively. **Figure 2.8** is an illustration of this motion transition between two robot configurations. To describe the new robot tip position after a change of chamber volume from the previous tip position, a forward transition model of the soft robot can be defined as:

$$p_{k+1} = f(p_k, \Delta u_k) \tag{2.1}$$

The inverse transition model we aim to estimate determines the required change in chamber volume for a movement of the robot tip Δp_k:

$$\Delta u_k = \phi(\Delta p_k, u_k) \tag{2.2}$$

Note that due to the redundancy of the system, the mapping between the forward and inverse model is not one-to-one, which makes it challenging to find a consistent inverse transition model.

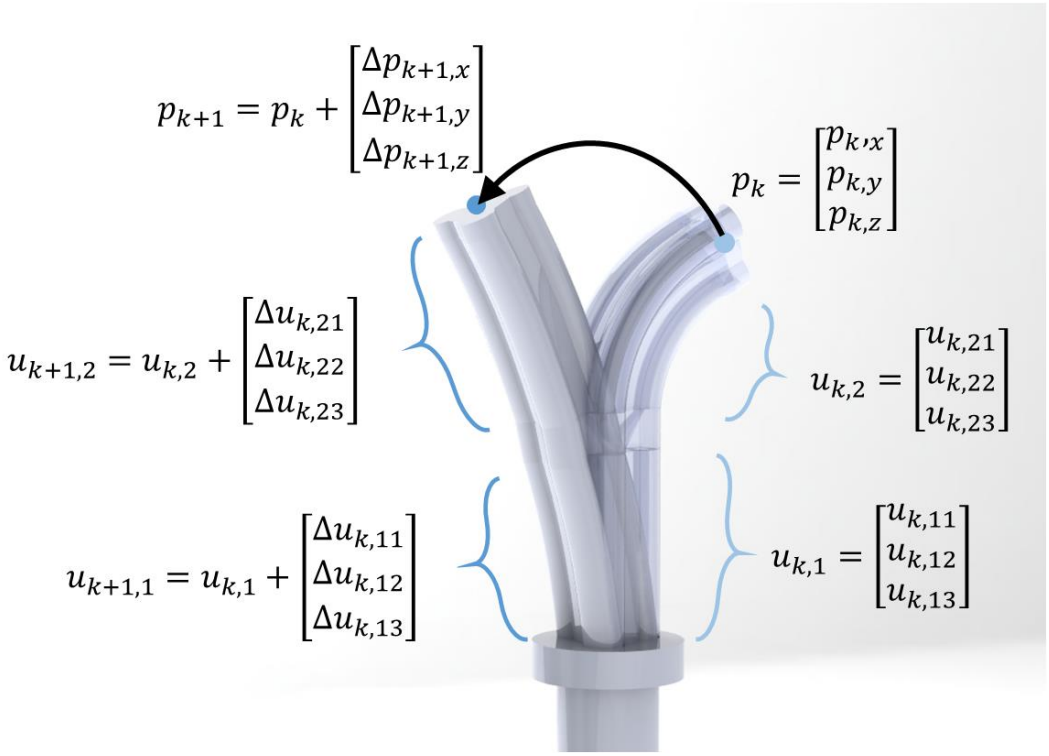

Figure 2.8 Labelled illustration of the robot motion transition for a two-segment soft robot. Pictured is the transition from state $(p_k, u_k) \rightarrow (p_{k+1}, u_{k+1})$. Inflation of the fluidic chambers of the first and second segments are labeled $u_{k,1}$ and $u_{k,2}$, respectively.

2.2.3 Overview of Online Learning Algorithm

The objective is to control the soft robot accurately in the task space motion transition coordinate Δs_k, while under unknown loading. For this reason, an online learning algorithm based on the work found in [30] is adapted for usage on our redundant two-segment soft continuum robot. The underlying goal of the algorithm is to estimate the global inverse mapping of the soft robot by combining a large set of localized linear controllers. This technique is based on the key idea that in a localized region of robot configuration, a valid inverse solution can be obtained because the inverse kinematics mapping forms a convex function with respect to the variables $\Delta p, p, \Delta u, u$.

The proposed control framework is split into two main phases: 1) incremental learning of the local forward models, followed by 2) batch learning of the linear inverse controllers that are only valid within a local region.

The first phase aims to acquire an appropriate local linearization of the forward motion mapping $(p_k, \Delta u_k, u_k) \rightarrow \Delta p_k$, which is nonlinear in general. Such local linearization can determine how many linear models are required to approximate the motion mapping, as well as the valid region of each linear model. Thus, a localized regression method, namely Locally Weighted Projection Regression (LWPR) [40], is employed to learn the forward motion mapping. LWPR provides a piecewise linear function approximation of the nonlinear mapping and automatically determines the valid local regions that each models should affect. The learnt piecewise linear models are in the form:

$$\Delta p_k = [p_k, \Delta u_k, u_k]\hat{\beta}_{FK}^i \tag{2.3}$$

where $\hat{\beta}_{FK}^i$ are the linear parameters of the local forward models. The subscript FK is shorthand for *forward kinematics*. The symbol i is the model index, and k is the current time step.

For a non-redundant robotic system, direct usage of the locally learnt forward models is possible due to the one-to-one mapping between the configuration space and operation space, meaning that linear combinations of the locally learnt models will be consistently resolved. However, for a redundant system, invalid solutions would arise from non-convex training data, which brings the need to consider the spatial localisations of the learnt models. Therefore, for each piecewise linear model in the LWPR forward model, we assign a linear controller to approximate the global inverse mapping, using the same local valid regions. We wish to determine the local inverse transition models also positioned in p_k and u_k space; this can be described by the following linear controller:

$$\Delta \mathrm{u}_k = \left[\Delta \mathrm{p}_{ref,k}, p_k, u_k\right]\beta_{IK}^i \tag{2.4}$$

where β_{IK}^i is the parameter of the local inverse model for which its calculation will be described in further detail in the following sections. The subscript IK is shorthand for *inverse kinematics*.

2.2.4 Algorithm Implementation

2.2.4.1 Combining the local controllers

To construct a global controller, such that the required actuator transition Δu_k can be found for a desired tip transition $\Delta p_{ref,k}$, a weighted linear combination of the local inverse transition models is solved in the form:

$$\Delta u_k = \frac{\sum_{i=1}^{n} w^i(p_k, u_k)\left[\Delta p_{ref,k}, p_k, u_k\right]\beta_{IK}^i}{\sum_{i=1}^{n} w^i(p_k, u_k)} \tag{2.5}$$

In the first step of the proposed control framework, the local forward models are learnt through LWPR, which determines an appropriate number of models as well as their locally valid region. Each local model and its region, also known as a receptive field (RF), is governed by a Gaussian kernel, and is weighted to each training data point based on the robot configuration variables p_k and u_k, calculated by the following equation:

$$w^i(p_k, u_k) = \exp\left\{\frac{1}{2}\left(\begin{bmatrix} p_k \\ u_k \end{bmatrix} - c^i\right)^T D^i \left(\begin{bmatrix} p_k \\ u_k \end{bmatrix} - c^i\right)\right\} \tag{2.6}$$

where i denotes the RF being weighed against, c^i is the RF's center in p_k and u_k space, and D^i is the distance matrix which governs the shape of the RF. Besides the weighted mean of Δu_k, the weighting $w^{\mathrm{i}}(p_k, u_k)$ is also employed to determine relative influence of each data point to the RFs when calculating the global inverse solution.

2.2.4.2 Selecting null-space behaviour with constrained optimization

When solving for a global controller, there is no guarantee that a consistent inverse solution is found among different local controllers due to the infinite possible solutions in a redundant system. In [30], two particular methods are outlined to overcome the redundancy problem: the first is by biasing the original training data to only allow a single inverse solution, and the second is to introduce a reward/cost function to draw the system to a desired solution. Although the first approach can be useful for simplified tasks, the benefits of using a redundant actuator are mostly lost when restricted to a single solution and can result in the task not being accomplished properly.

Therefore, to ensure consistent null-space behaviour through the second approach, the task is formulated as a constrained optimization problem, where we aimed to minimize the cost function below:

$$C_k(\Delta u_k) = \left(\Delta u_k - \Delta u_{0,k}\right)^T N\left(\Delta u_k - \Delta u_{0,k}\right) \tag{2.7}$$

where $\Delta u_{0,k} = v(p_k, u_k)$ is the actuator-space attractor that draws the robot to a desired configuration, and $N > 0$ is a positive definite weighting matrix. The cost function in (2.7) assigns cost to each incoming training data point. It assigns higher cost for incoming Δu_k values that are further away from the desired pose, as defined in the function $v(p_k, u_k)$. This enables systematic resolution of the redundancy problem, while allowing a

flexible definition of the user-desired null-space behaviour. A secondary control objective can hence be achieved by associating the null-space attractor, $\Delta u_{0,k}$ to the robot characteristics or the task's requirement. One typical example of the null-space behaviour is to attract the robot configuration towards a rest pose u_0, as defined in (2.8). For a fluid-driven robot, a reasonable choice of rest position is to minimize the overall inflated chamber pressures:

$$\Delta u_{0,k} = K_a(u_k - u_0) \tag{2.8}$$

where K_a is the attractor gain. Thus, all the training data is given a cost that is based on the configuration space variables u_k, p_k and Δu_k. To solve the constrained optimization problem in (2.7), we first define:

$$\min_{\Delta u_k} \quad C_k(\Delta u_k) \tag{2.9}$$

$$\text{subject to} \quad \Delta u_k = \left[\Delta p_{ref,k}, p_k, u_k\right]\beta_{IK}^i$$

The constrained optimization problem can be solved by converting the cost function into an immediate reward:

$$r(u_k) = \sigma_i \exp\left[-0.5\sigma_i^2 C_k(\Delta u_k)\right] \tag{2.10}$$

where σ_i^2 is the mean cost for a particular local model, used to increase learning speed:

$$\sigma_i^2 = \sum_{k=1}^{n} w^i(p_k, u_k) C_k \Big/ \sum_{k=1}^{n} w^i(p_k, u_k) \tag{2.11}$$

where *n* is the total number of training samples. By changing to an immediate reward, we can find a solution which minimizes the following sum:

$$\sum_{k=1}^{n} r(u_k) w^i(p_k, u_k)\left(\Delta u_k - \left[\Delta p_{ref,k}, p_k, u_k\right]\beta_{IK}^i\right) \tag{2.12}$$

The local model parameter in (2.4) is found by the reward-weighted regression formula, for each local controller model, i:

$$\beta_{IK}^i = \left(X^T W^i X\right)^{-1} X^T W^i Y \tag{2.13}$$

where $X_k = [\Delta p_{ref,k}, p_k, u_k]$ and $Y_k = [\Delta u_k]$ are rows of the training datasets X and Y, respectively, and $W^i = \text{diag}(r(u_1)w_1^i, \dots, r(u_n)w_n^i)$. The weighting coefficient matrix, W^i, is a diagonal matrix that applies weighting between each local controller, i, to each training sample. For each local controller, the corresponding weighting coefficient matrix is determined by multiplying the reward of each training data point by the weighting of that point relative to the local controller. The reward as shown in (2.10) regulates the redundancy of the system by giving more importance to training data that exhibits the desired null-space behaviour as defined in (2.8)**.** The weighting function defined in (2.6) more strongly considers the weights of training points closer in p_k, u_k space to the local controller. Finally, a consistent global controller is derived from the weighted average of all the learnt local inverse models as in (2.5). The pseudo-code for the online learning process of the controller is detailed in **Algorithm 1**, where there are m total local models.

Algorithm 1: Algorithm for online learning of consistent inverse motion mapping.

For each new training sample $[\Delta p_{ref,k}, p_k, \Delta u_k, u_k]$

Add $(p_k, \Delta u_k, u_k) \rightarrow \Delta p_{ref,k}$ to the forward model through LWPR

Update no. of forward models *m* and their local weightings $w^i(p_k, u_k)$

Evaluate actuator-space attractor:

$$\Delta u_{0,k} = K_a(u_k - u_0)$$

Compute cost:

$$C_k(\Delta u_k) = (\Delta u_k - \Delta u_{0,k})^T N(\Delta u_k - \Delta u_{0,k})$$

For each model $i = 1,2,3, \dots, m$

Calculate mean cost:

$$\sigma_i^2 = \sum_{k=1}^n w^i(p_k, u_k) C_k \,/\, \sum_{k=1}^n w^i(p_k, u_k)$$

Calculate reward of each data point:

$$r(u_k) = \sigma_i \exp\left(-0.5\sigma_i^2 C_k(u_k)\right)$$

Solve the following weighted regression problem with steps 10-14:

$$\sum_{k=1}^n r(u_k) w^i(p_k, u_k) \left(\Delta u_k - [\Delta p_{ref,k}, p_k, u_k]^T \beta_{IK}^i\right)$$

Add sample point to weighted regression so that:

$$X_k = [\Delta p_{ref,k}, p_k, u_k]$$

$$Y_k = [\Delta u_k]$$

$$W^i = \text{diag}r\left((u_1)w_1^i, \dots, r(u_n)w_n^i\right)$$

Update inverse mapping parameter by reward-weighted regression:

$$\beta_{IK}^i = (X^T W^i X)^{-1} X^T W^i Y$$

end

end

2.3 EXPERIMENTS, RESULTS, AND DISCUSSION

2.3.1 Experimental Platform Setup

The two-segment robot was actuated pneumatically by a set of stepper-motor driven linear actuators. Each linear actuator consisted of a stepper motor coupled to a leadscrew, which controlled the stroke of a pneumatic cylinder (**Figure 2.9(a)**). The robot has 6 input DOFs, with each of the 6 chambers of the soft robot paired with a single linear actuator.

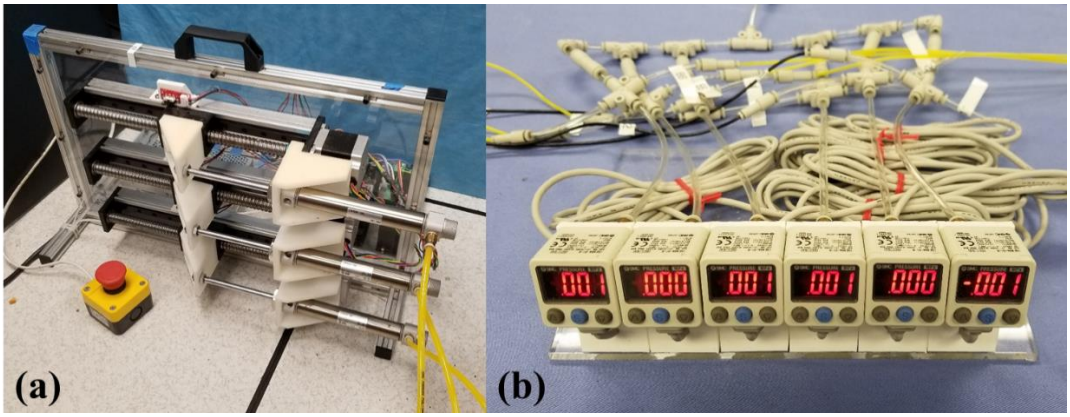

Figure 2.9 Overview of actuation setup. **(a)** Air chambers of the soft robot are controlled by modulating the volume in pneumatic cylinders, which are mounted to stepper motor-driven linear drives. **(b)** Pressure sensors (ISA80 Series, SMC) monitor the pre-pressure level of each air chamber.

The soft robot was actuated volumetrically, with the stepper motor positions used as a proxy for the actual cylinder volume. Each chamber was pre-pressurised to 0.040 MPa to improve the bending response of the soft robot to input pressure change. The chambers were monitored with pressure sensors (ISA80 Series, SMC) connected through pneumatic tubing as in **Figure 2.9(b)**. An omnidirectional bending angle of up to 100° was attainable by each segment of the soft robot. The tip position of the robot was tracked by an electromagnetic (EM) tracking system (NDI Medical Aurora Tabletop Field Generator). Two 6-DOF tethered sensor (0.8 mm diameter x 9 mm length) were attached to the robot: one at the robot tip, and another at the base of the robot as illustrated in **Figure 2.10**. The EM tracking system provides a tracking accuracy of 0.80 mm for position, and 0.70° for orientation at an update rate of 40 Hz. It provides the necessary positional data for feedback control and also online learning of the controller. The NDI system is designed for accurate tracking even when surrounded by tissue and bone during surgery and is robust in most environments that do not have large ferromagnetic objects.

The local online learning algorithm was implemented in the Matlab environment, and applied the open-source library for LWPR [41].

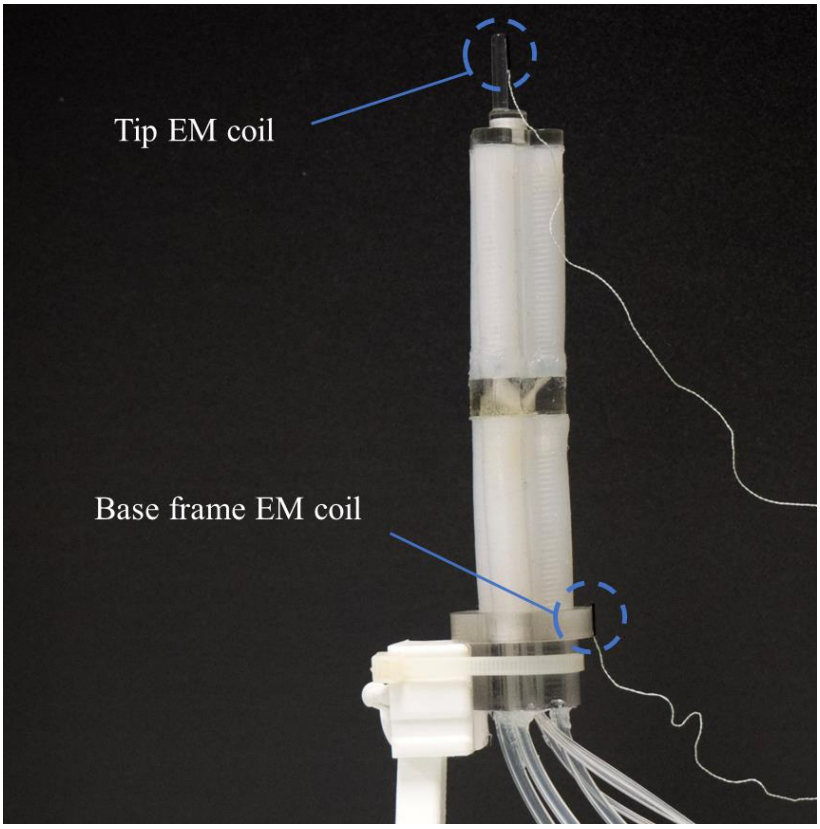

Figure 2.10 EM positional tracking coils mounted at the robot tip and base. A 6-DoF coil at the base offers a static frame of reference for all the measured tracking data in real time.

2.3.2 Training Data Acquisition and Model Pre-training

In order to effectively generate a functional global controller, pre-training data that sufficiently characterizes the robot's workspace and possible configurations should be obtained. Learning of the forward models was first performed offline with uniformly distributed random waypoints in actuator-space that were generated and connected by straight line trajectories. This formed the pre-training exploration data. For the purpose of this study, 80 random waypoints were enough to provide a large enough selection of forward mappings so that consistent inverse controllers could be learnt. An alternative controller initialization can be achieved by motor babbling, where small, random movements of the robot are used to learn the controller online. However, offline pre-training was favoured in this study to better evaluate the null-space behaviour of the controller. Additionally, if purely online learning is used, redundant configurations are less likely to be observed, limiting the manoeuvrability of the robot and generality of the system. In this study, the tip position, p_k, is a 3x1 vector of the x-y-z Cartesian tip position tracked by the tip EM coil as in **Figure 2.10.** The chamber volumes, u_k, are a 6x1 vector which describes the current inflation state of each chamber of the robot (3 chambers per robot segment).

Validation of the learned forward models was performed by splitting the obtained training data into a training and test set, at 80% and 20%, respectively. The root-mean-square error (RMSe) of the predicted forward model outputs, Δp, versus the number of training iterations (epochs) for the training data, test data, and combined data is shown in **Figure 2.11.** A total of 15 training iterations were processed, resulting in 139 receptive fields generated for each output dimension. The RMSe of all three types of data was lowest at 11 epochs, with the testing set converging to approximately 1 mm. To further validate the pre-trained model, the predicted outputs of the global inverse model was compared against the learned forward model using the combined test set. The resulting regression plots and histograms for each task space dimension are shown in **Figure 2.12**. The error bounds for each dimension of the learned inverse model were under 0.5 mm. Outliers predominantly seen in the *x* and *y* regression plots may be due to the redundancy of the two-segment robot platform. Some robot poses from the randomly sampled testing data may not have a suitable prediction because that particular pose may not have been used in training of the learning model. The cluster of high-error outputs at very small tip movement steps may be due to a localised area of the training data, where actuation is near the rest pose of one or both robot segments. Paired with the fact that the sampled data is direction-dependent (e.g. some training waypoints may move the robot primarily along either the *x*-axis or *y*-axis), the desired tip motion along only one direction may not be achievable with the pre-trained model alone. This may result in large deviation, namely the outliers seen in **Figure 2.12**.

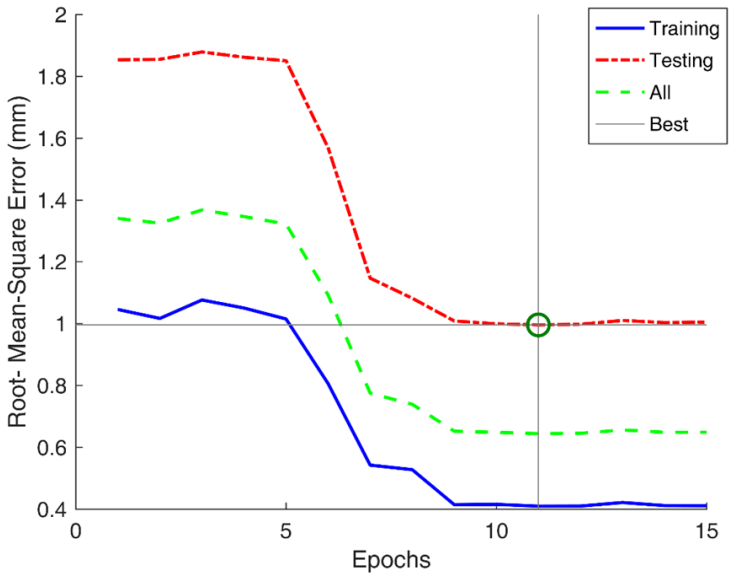

Figure 2.11 Validation of the forward model that was trained through LWPR. The original data set was split into 80% training and 20% training data. The root-mean-square error is with respect to the forward model output, Δp. The error of all three sets of data was lowest at 11 epochs, indicated by the vertical grey line.

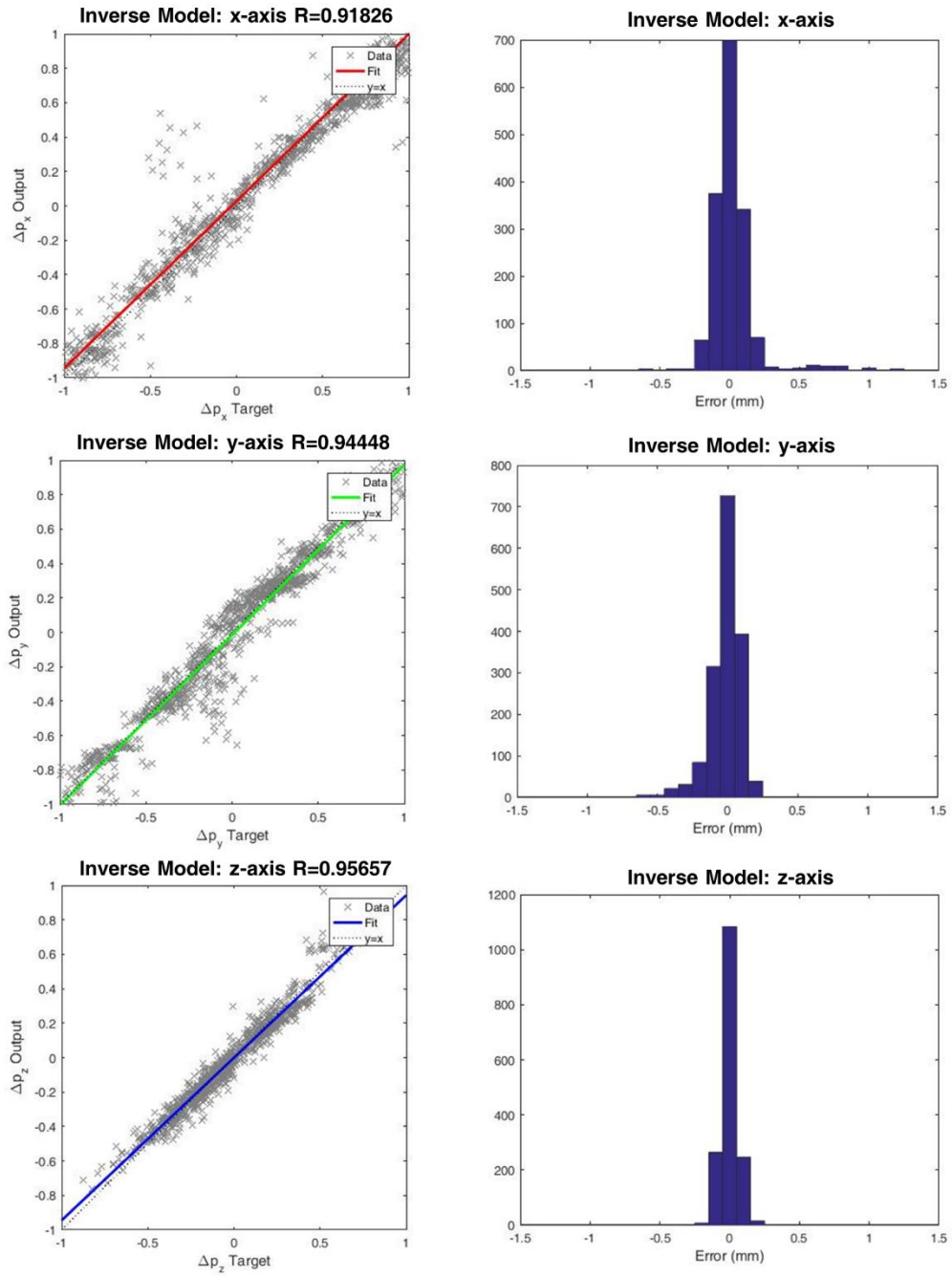

Figure 2.12 Regression plots **(left)** and histograms **(right)** for the tip transition variable Δp in each coordinate axis (x, y, z).

2.3.3 Controller Implementation

Evaluation of the proposed control framework is performed on a two-segment soft continuum robot. Two tracking exercises are presented to assess the accuracy of the learnt inverse kinematics as well as its ability to adapt to an unknown disturbance. The trajectory following is achieved through resolved motion rate control [42], and the desired task space displacement Δs_k is defined by the proportional feedback controller:

$$\Delta p_k = K_P\left(p_k^{ref} - p_k\right) \tag{2.14}$$

where K_P is the proportional gain, p_k^{ref} is the desired tip position, p_k is the 3D tip position at the current time-step. This desired task space displacement is the input to the learned global controller, which outputs the estimated stepper motor commands Δu. A simple proportional controller was used as opposed to a PI or PID controller, so that the performance of the learning-based modelling could be clearly seen and not be dominated by the closed-loop feedback. However, only using proportional control comes at the cost of overall tracking accuracy and control stability. For the accuracy evaluation, the tracking error is calculated by the Euclidean distance between the desired tip position and the achieved tip position at each time step. The block diagram of the implemented control loop is shown in **Figure 2.13.**

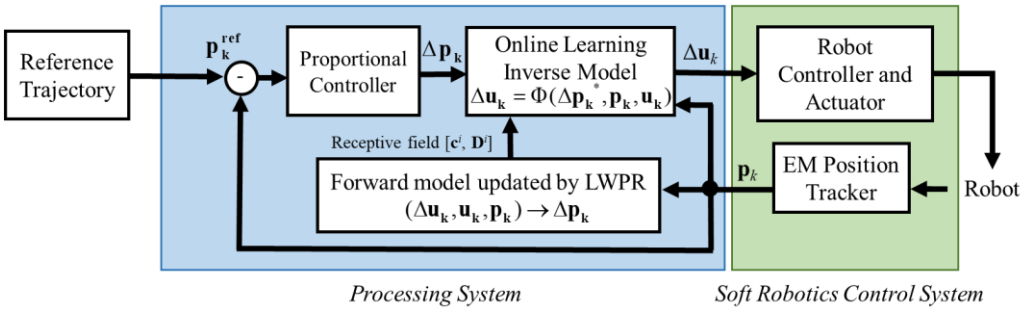

Figure 2.13 Schematic of the proposed control system architecture that facilitates online updating of the learned controller. The controller is constantly updated with incoming real-time data provided by the EM position tracker.

2.3.4 Trajectory Tracking Experiments - Static Tip Load

A comparison between the online-updating controller and the offline-learned controller was performed by trajectory tracking of a 3D path under two scenarios: 1) only using the pre-trained model with no online learning, i.e. 'offline', 2) online learning while an unknown tip mass is added to the robot.

The goal of these two experiments is to evaluate the effects of updating the pre-trained model in an online manner and providing a comparison to only using the pre-trained model. The test trajectory is a rectangular shape of sides 25 mm x 100 mm projected to the 3D workspace of the robot, which was approximated from the pre-training data. In each test scenario, the controller was run for 3 complete cycles, which had a total runtime of 400 s. Initially in each test, the robot was allowed to track to the first point of the desired trajectory until the error converged, at which point data acquisition was initiated and the desired trajectory point began to increment. The same error-proportional gain and pre-

trained model was used for both experiments. In the following experimental sections, *offline* denotes the absence of online learning during trajectory tracking, and *online* denotes that online learning was enabled.

2.3.4.1 No tip load – offline

For the first experiment, only the offline pre-trained model was implemented into the robot controller. Online learning was disabled, and robot was free to track the target trajectory with no additional external disturbances. The tracking performance of the first experiment is presented in **Figure 2.14.** The average error was not observed to improve between the first and last trajectory cycle, with a mean absolute error of ±4.56 mm, and ±5.53 mm, respectively. A recurring error pattern could be seen in each cycle, which depicts the repeatability of the learned controller. The tracking error could be attributed to a lack of densely populated receptive fields in those regions resulting in poorly defined inverse solutions. Other controller errors are also expected due to the hysteretic effects of the soft robot body which the proportional controller could not compensate for.

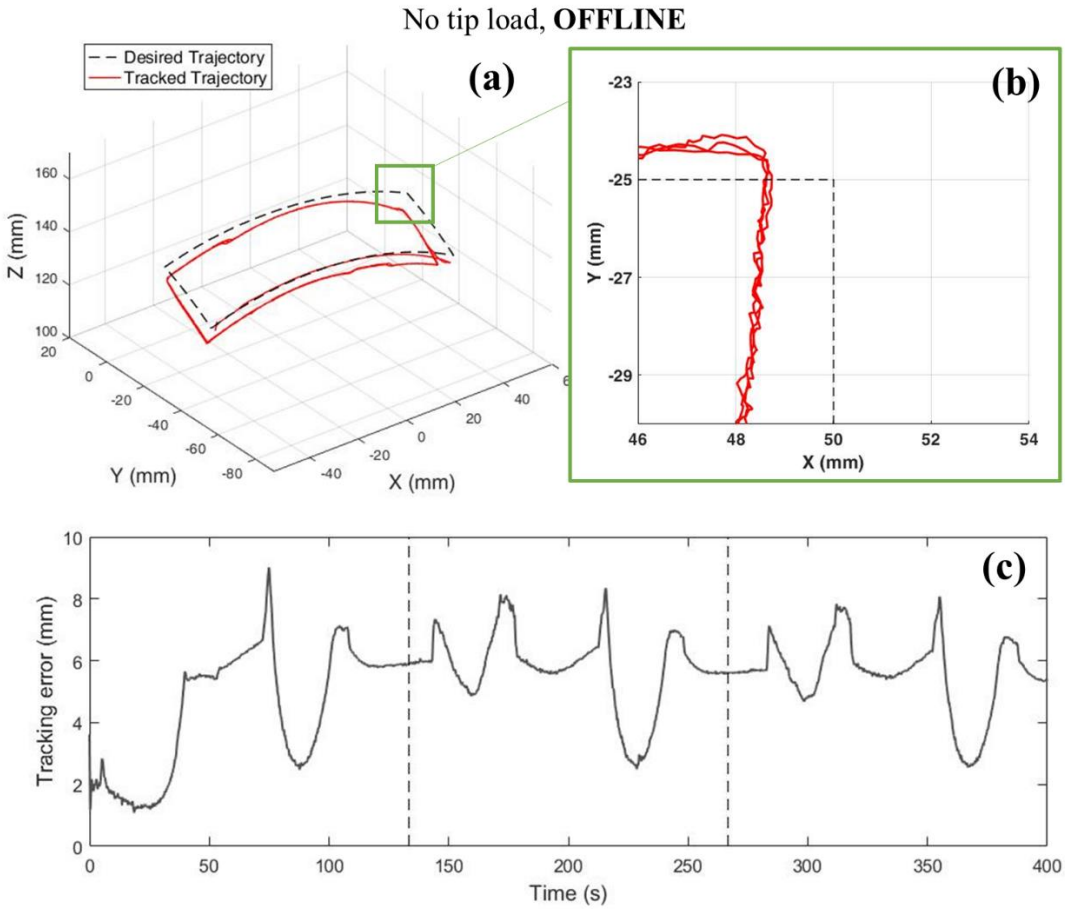

Figure 2.14 Experimental result for trajectory tracking with no additional tip loading using the pre-trained model, without online learning. **(a)** The actual tracked trajectory overlaid on the desired trajectory. **(b)** Close-up view of the corner tracking performance. **(c)** The Euclidean tip tracking error over time. The dotted lines indicate the start and end of each trajectory cycle.

2.3.4.2 Static tip load – online learning

For the second experiment, an additional tip mass was added to the robot tip, as illustrated in **Figure 2.7(b)**. The total additional mass was 14.2 g and was not previously presented to the model during pre-training. The same pre-trained model applied in experiment 1 was used as a baseline for the online learning in this experiment. When online learning, a fixed number of training points are used to weight the influence of the local models. For this experiment, a maximum of 425 incoming training points was used in a first-in-first-out basis, where the oldest data points were removed first when exceeding the maximum of 425. For each cycle of trajectory tracking, approximately 400 new training points were accumulated. The average online update frequency was 23 Hz. With the additional tip weight, the starting tracking error increased from approximately 2 mm as seen in the first experiment to 5 mm. By the inclusion of online learning in this controller, the real-time data obtained from the tracked tip position and actuator volumes could be input to the online learning algorithm, enabling incremental improvements to the overall learned inverse model. This could be observed in the results presented in **Figure 2.15**. The mean absolute tracking error of every cycle could be seen to decrease significantly, starting at ±4.42 mm in the first cycle and reducing to ±1.63 mm in the third cycle.

A comparison of the tracking performance with and without online learning are shown in **Table 2.1**. Overall, online learning of the original pre-trained model could be seen to improve the tracking performance through continuous online updating of the inverse model, even in the presence of a previously unknown external disturbance.

Table 2.1 Summary of trajectory tracking performance for the no tip load (offline) and tip load (online) scenarios.

Controller setting	*Error absolute mean and standard deviation (mm)*			*Maximum absolute error (mm)*		
	1st cycle	*2nd cycle*	*3rd cycle*	*1st cycle*	*2nd cycle*	*3rd cycle*
No tip load ***OFFLINE***	±4.56 (σ = 1.99)	±5.72 (σ = 1.18)	±5.53 (σ = 1.12)	±9.02	±8.34	±8.07
Static tip load ***ONLINE***	±4.42 (σ = 1.08)	±3.33 (σ = 1.14)	±1.63 (σ = 0.54)	±7.90	±6.87	±3.55

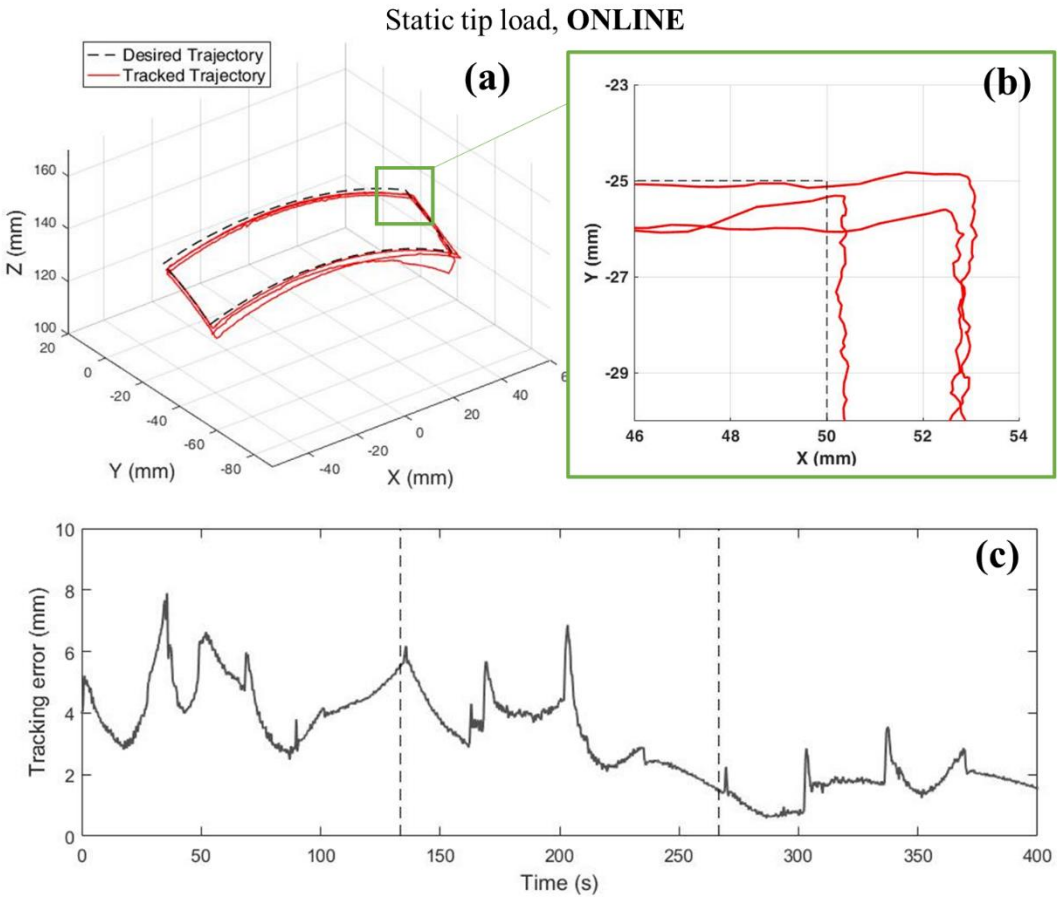

Figure 2.15 Experimental result for trajectory tracking with additional tip loading using the pre-trained model and updated with online learning. The algorithm can adapt to the tip disturbance in real-time, providing improved tracking performance. **(a)** The actual tracked trajectory overlaid on the desired trajectory. **(b)** Close-up view of the corner tracking performance. **(c)** The Euclidean tip tracking error over time. The error can be seen to consistently decrease over the 3 cycles.

2.3.5 Trajectory Tracking Experiments - Varying Tip Load

To further investigate the control framework's behaviour, a series of trajectory following tasks were performed while a variable fluid tip load as in **Figure 2.7(c)** was added to the robot tip. The fluid tip has an empty weight of 14 g and has a maximum weight of 32 g when full (corresponding to an internal volume of 18 mL). Three experiments were performed for 3D trajectory tracking with the varying tip load: 1) only the empty (0% filled) fluid tip container added to the robot tip with no online learning, 2) increasing fluid load with no online learning, 3) increasing fluid load with online learning enabled.

For this set of experiments, the test trajectory is a rectangular shape with sides 40 mm x 60 mm that was projected on the workspace of the robot. The robot was allowed to run for 4 cycles. The same control parameters were used in the three scenarios, with only the option of online learning differing between them. The training data used for the pre-trained model were based on 320 random waypoints, which resulted in 352 receptive fields

generated. A tabulated summary of the tracking results is shown in **Table 2.2**, and the actual tracked trajectories and absolute Euclidean tracking errors over time are shown in **Figure 2.17**.

2.3.5.1 Empty fluid container tip – offline

In the first scenario, only the pre-trained model was used, with no online updates made during the experiment. This '*offline'* controller setting is akin to implementing a model-based kinematic model, e.g. PCC, where no online updates are made to the model during runtime. The fluid container tip was empty for all four cycles of trajectory tracking, weighing approximately 14 g. Overall, the tracking performance for each cycle was seen to be relatively periodic as seen in **Figure 2.17(a)**, with the mean absolute error remaining around the 6-7 mm range. No notable improvement could be seen between each cycle, however the mean absolute and max absolute error increased between cycle 1 and 2. This is likely because the robot was allowed to track to the first point until error converged before data acquisition began and the remainder of the trajectory was tracked. The primary source of error in the trajectory tracking can be attributed to the additional unmodelled tip load due to the empty fluid container tip. The tip load induces unmodelled loading to the entire robot body, creating a large disparity between the original pre-trained kinematic model's estimation, and the actual robot configuration.

Unlike the static tip load experiment in **Section 2.3.4.2** where the tracking error would reduce over each cycle due to the online learning, we can see a consistent offset of the tracked trajectory versus the desired trajectory.

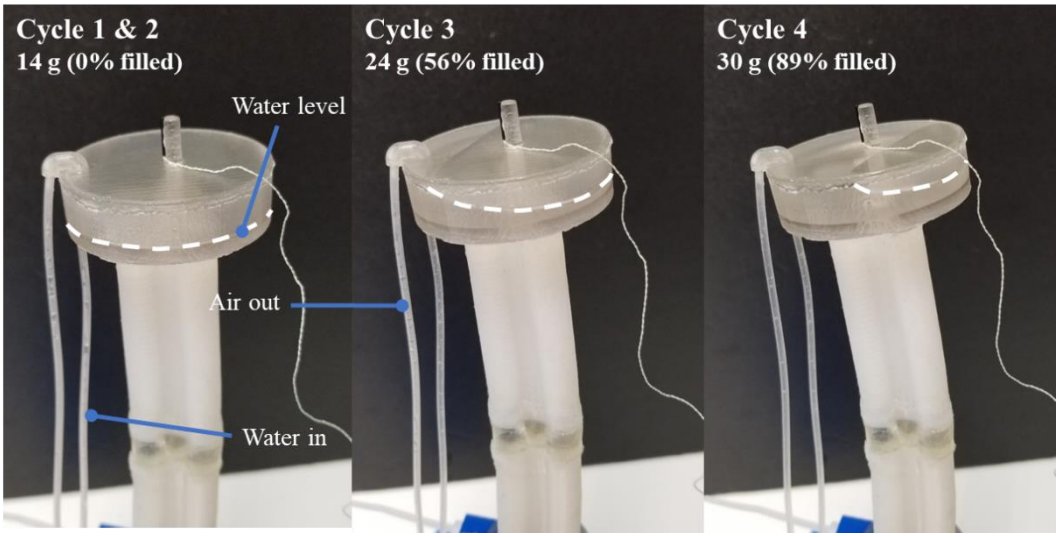

Figure 2.16 Variable fluid tip load used for experiments. The tip load was varied by injecting water at an approximate rate of 0.6 mL/s at the beginning of cycle 3 and 4. The empty fluid tip is 14 g and has a maximum weight of 32 g when full. For the trajectory tracking experiments under varying tip load, 10 g is added to the tip load in cycle 3, and 6 g is added in cycle 4.

2.3.5.2 Increasing fluid load – offline

For the second scenario, a varying tip load was applied to the robot tip by increasing the fluid volume in the fluid tip in accordance to **Figure 2.16**. To fill the fluid tip, water was injected through the 'water in' tube at a rate of approximately 0.6 mL/s. For the first two cycles of trajectory tracking, the fluid tip was empty (0% filled), which is the same conditions as the first two cycles of the previous experiment in **Section 2.3.5.1.** In cycle 3 and 4, the fluid levels in the tip were increased by an additional 10 g of water from the beginning of cycle 3 at a rate of ~0.6 mL/s, with a total tip load of 24 g. This corresponds to 56% of the entire fluid tip cavity filled. At the start of cycle 4, an additional 6 g of water was added to the fluid tip, corresponding to a total additional tip weight of 30 g, or 89% filled. At 30 g, the fluid tip is an additional 72% of the robot body mass (41.71 g), presenting substantial loading to the robot tip. Depicted in **Figure 2.16** is the deformation caused by the fluid load when the robot is at the *neutral, unactuated* position. When tracking the trajectory, the moment caused by the load is larger due to the robot bending and induces significant unmodelled deformation.

In the first two cycles, it can be seen that the tracking error and path taken was very similar to the results in **Section 2.3.5.1** This is because the controller setting and tip load are the same between the two experiments in the first two cycles. When fluid level was increased in the tip load in cycle 3, the errors also increased, eventually leading to instability in the 4th cycle which is seen in the left-hand side of the tracked trajectory path in **Figure 2.17(b)**. A major source of the instability can be attributed to the inability of the offline controller to track the desired trajectory due to large corrective overshoot from the error induced by the tip load. Also, the fluid tip is only partially filled, leading the centre of mass to constantly change as the robot configuration changes, further amplifying any instability.

2.3.5.3 Increasing fluid load – online learning

In the third scenario, online learning was enabled during trajectory tracking while the fluid load was increased in accordance to **Figure 2.16**. The same pre-trained model use in the previous two scenarios was also used here. For online learning, the maximum number of data points was set to 550. For each cycle of trajectory tracking, approximately 300 new training points were accumulated. Similar behaviour to the online static tip load experiment in **Section 2.3.4.2** can be seen, with the error reducing in each cycle. Over the four cycles, the average tracking error reduced from ±4.16 mm to ±0.98 mm. In contrast to the independent test in **Section 2.3.5.2** that demonstrates offline tracking with increasing fluid load, the online learning controller was able to avoid instability, and even reduce the overall

tracking error. The tracked trajectory and error can be seen in **Figure 2.17(c)**.

In this third scenario, the update rate was limited to approximately 7 Hz, i.e. each online update took ~0.143 s to complete. A notable limitation of the online learning is that the update speed is directly tied to the number of stored training data points and local models, because the weighting of each data point to each local controller must be made at each update, in accordance to the weighting function (2.6**)**. The online update rate for this controller was significantly lower than that in **Section 2.3.4.2** because 352 local controllers were used in the pre-trained model, compared to 139 local controllers. This extensive computation time is a bottleneck for the online learning framework, as too many local models or stored data points would cause the update rate to slow to impractical speeds. A potential method for easing the computational intensity is through the use of training data sparsification. This would involve limiting and selectively processing training data obtained online so that only the 'most important' training points would be used.

In general, the online learning experiments performed in this study highlight the difficulties of using a standard, non-adaptive controller for control of a soft robot under external disturbance. High unmodelled morphological change can cause typical feedback controllers utilizing Jacobians to exhibit inaccurate or unstable trajectory tracking because they assume low error configurations, which is not true for soft robots under any notable levels of loading. However, through online learning the robot configuration error can be minimized by effectively updating the Jacobian to adapt to disturbances based on real-time tracking data. For more extreme cases of deformation, the controller can potentially fail to track the target trajectory. This could be caused by the robot configuration lying far outside of the pre-trained local linear models, or due to limitations of the robot actuation (e.g. upper pressure limit of the robot chambers). The tracking result of decreasing fluid load was not tested; however, the controller should be able to adapt similarly to the increasing load over each subsequent cycle, if the rate of decrease is the same as the increase used here.

Table 2.2 Summary of trajectory tracking performance for experiments with variable fluid tip load.

Controller setting	*Error absolute mean and standard deviation (mm)*				*Maximum absolute error (mm)*			
	1st cycle	*2nd cycle*	*3rd cycle*	*4th cycle*	*1st cycle*	*2nd cycle*	*3rd cycle*	*4th cycle*
Empty fluid load ***OFFLINE***	±6.01 (σ = 1.77)	±7.19 (σ = 2.17)	±7.08 (σ = 2.12)	±6.94 (σ = 2.09)	±9.73	±11.16	±11.23	±11.19
Increasing fluid ***OFFLINE***	±5.82 (σ = 1.64)	±7.24 (σ = 2.00)	±10.36 (σ = 1.22)	±12.84 (σ = 2.20)	±9.47	±11.22	±12.88	unstable
Increasing fluid ***ONLINE***	±4.16 (σ = 2.19)	±3.10 (σ = 1.94)	±1.07 (σ = 0.24)	±0.98 (σ = 0.26)	±9.72	±8.01	±2.19	±2.44

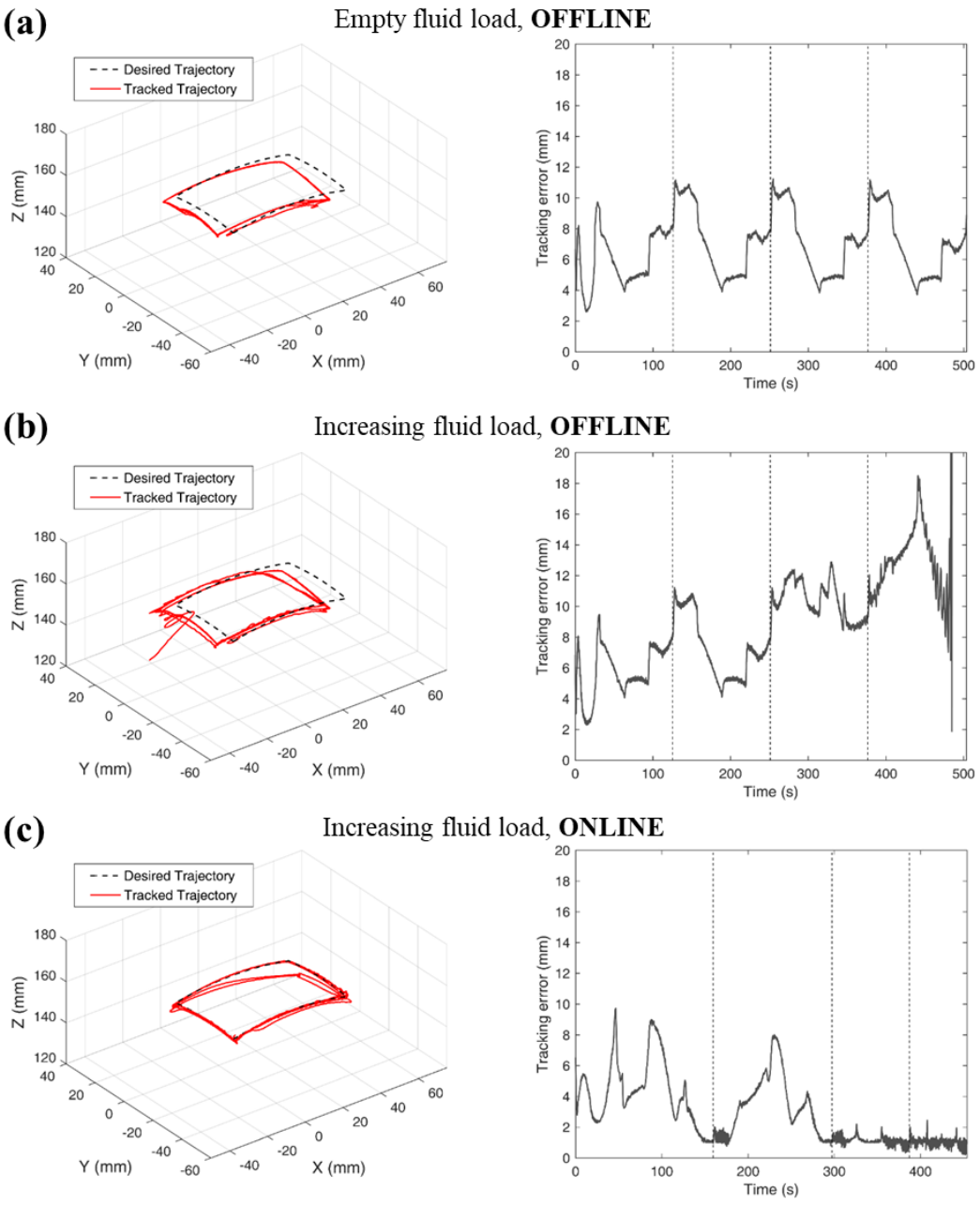

Figure 2.17 Experimental results for trajectory tracking with fluid tip load and controller conditions. The robot followed the trajectory for 4 cycles, with vertical dotted lines separating the cycles on the right graphs. **(a)** Offline trajectory tracking with empty fluid container tip weighing 14 g. A repeating error pattern is observed due to the static load. **(b)** Offline trajectory tracking with fluid tip load increased by 10 g in cycle 3, and 6 g in cycle 4. The tracking error increased with fluid load, becoming unstable in the 4th cycle. **(c)** Trajectory tracking with online learning enabled. The fluid tip load was increased by 10 g in cycle 3 and 6 g in cycle 4. Instability was avoided, and tracking error was also reduced.

2.4 CONCLUSIONS AND FUTURE WORK

In this study, we proposed and validated an online learning-based control framework to control a hyper-redundant two-segment soft robot in a 3D positional task space. The use of an online data-driven learning approach enables high adaptability to unmodelled characteristics both internal and external to the soft robot, while resolving consistent redundancy behaviour. A pre-trained inverse model was learned for the two-segment soft robot and applied in a proportional motion rate controller. For the static tip load case with online learning, the robot controller was able to adapt quickly to an unknown static tip weight/load, with the average absolute error reducing from ±4.42 mm to ±1.63 mm over three cycles of the tested 3D trajectory. A more demanding trajectory tracking task was also performed with a varying fluid tip load. Without online learning, the robot became unstable and was unable to compensate for the maximum weight by the 4th cycle. However, with the addition of online learning the robot was not only able to avoid instability, but was also able to reduce the mean absolute tracking error to < 1 mm.

Our future work includes further extension of the proposed control framework to three or more segments of a soft robot and incorporation of a greater number of task space variables to improve the manipulability of the robotic system. In the future experimental settings, we would also aim to replace the tethered EM tracking system with a self-contained sensing modality, such as a camera [43] or a fibre optic system [44] such as those based on fibre Bragg gratings [45]. This would allow evaluation of the proposed learning algorithm in application-based scenarios. Additionally, secondary objectives can be incorporated into the algorithm's cost calculation, thus providing customizability for task-specific performance. For the example case of obstacle avoidance, the robot body could be tracked with sensors (e.g. multiple EM trackers, or multi-core FBG shape sensing as shown in **Section 3.2)** and used as additional configuration-space parameters. At each time step, the cost of each training point would need to be updated, with higher cost assigned to configurations with closer proximity to the obstacles. However, the frequent cost updates may greatly increase the computation time. Improvement to the computational speed of the learning framework can be made, with a possible solution being sparsification, which is used to select only the most relevant training data for updating.

Few online learning-based control approaches have been applied to fluid-driven soft continuum robots while under external disturbance. Examples are by Fang *et al.* [46], where camera feedback is used to update and control the robot in real time, and Lee *et al.* [37], which is based on the same online learning framework used in this chapter. Other studies have applied online learning to tendon-driven continuum robots [47] where there is a linear relationship between actuator space and joint space. However, this is generally not

directly translatable to fluid-driven soft robots due to the very non-linear relationship between actuator space and joint space [18]. When the field of online learning control becomes more developed for fluid-driven soft robots, the control performance can be compared between different approaches on the same robotic platform.

In terms of application, soft manipulators are inherently non-ferromagnetic and have more easily disposable bodies which present interesting opportunities to be used in harsh environments where traditional robots are unable to be used. An example of this is under magnetic resonance imaging (MRI), where the strong magnetic field involved disallows any traditional robots. Towards MRI-guided robotic interventions [48, 49], the integration of the proposed online learning algorithm and a soft robotic manipulator could enable safe and adaptive navigation in surgery.

CHAPTER 3
FIBRE BRAGG GRATING-BASED OPTICAL SHAPE SENSING

3.1 SINGLE-CORE FIBER SURFACE SHAPE SENSING

3.1.1 Introduction and Literature Review

In recent years, there has been a trend towards integrating soft and deformable structures into robotic systems. Target applications include surgery [50] and rehabilitation [51, 52], where researchers take advantage of soft and flexible robots for their inherent mechanical compliance. However, these soft robotic systems are often controlled with feedback from either large tracking systems, using indirect variables (e.g. pressure in fibre-reinforced actuators), or in an open loop, neglecting the fact that actual robot shape and posture are inevitably affected by the environment [53, 54].

As a result, measurement of the surface shape itself has become an area of interest. Some research utilises non-contact external equipment such as mono/stereo cameras and LiDAR to reconstruct 3D surfaces [55-57]. Photogrammetry is a well-known method for reconstructing 3D point cloud data from monoscopic camera images and is often used to obtain precise 3D data of large-scale objects such as sculptures or buildings (**Figure 3.1(a)**). Motion capture systems have also been employed to collect the local position information of subjects, with reflective markers attached to the surface [58, 59]. With sufficient

reflective markers, a subsampled reconstruction of a surface can be found, with an example shown in **Figure 3.1(a)** by Huang *et al.* [60] which combines marker-based motion capture with 3D scanning to achieve highly detailed reconstruction of facial expressions. Initial designs of the Gelsight [61] shown in **Figure 3.1(b)** sensors used external CCD cameras with visual processing techniques to measure the surface shape, force and slip from image frames for tactile sensing. Similarly, GelForce [62] uses CCD cameras to detect the displacement of markers in a flexible substrate to estimate surface traction fields. Although high-resolution sensing data from camera-based systems allows reconstruction of complex deformations, these kinds of systems are inconvenient to be used in soft robotics or stand-alone robotic systems due to their bulkiness and dependence on line-of-sight.

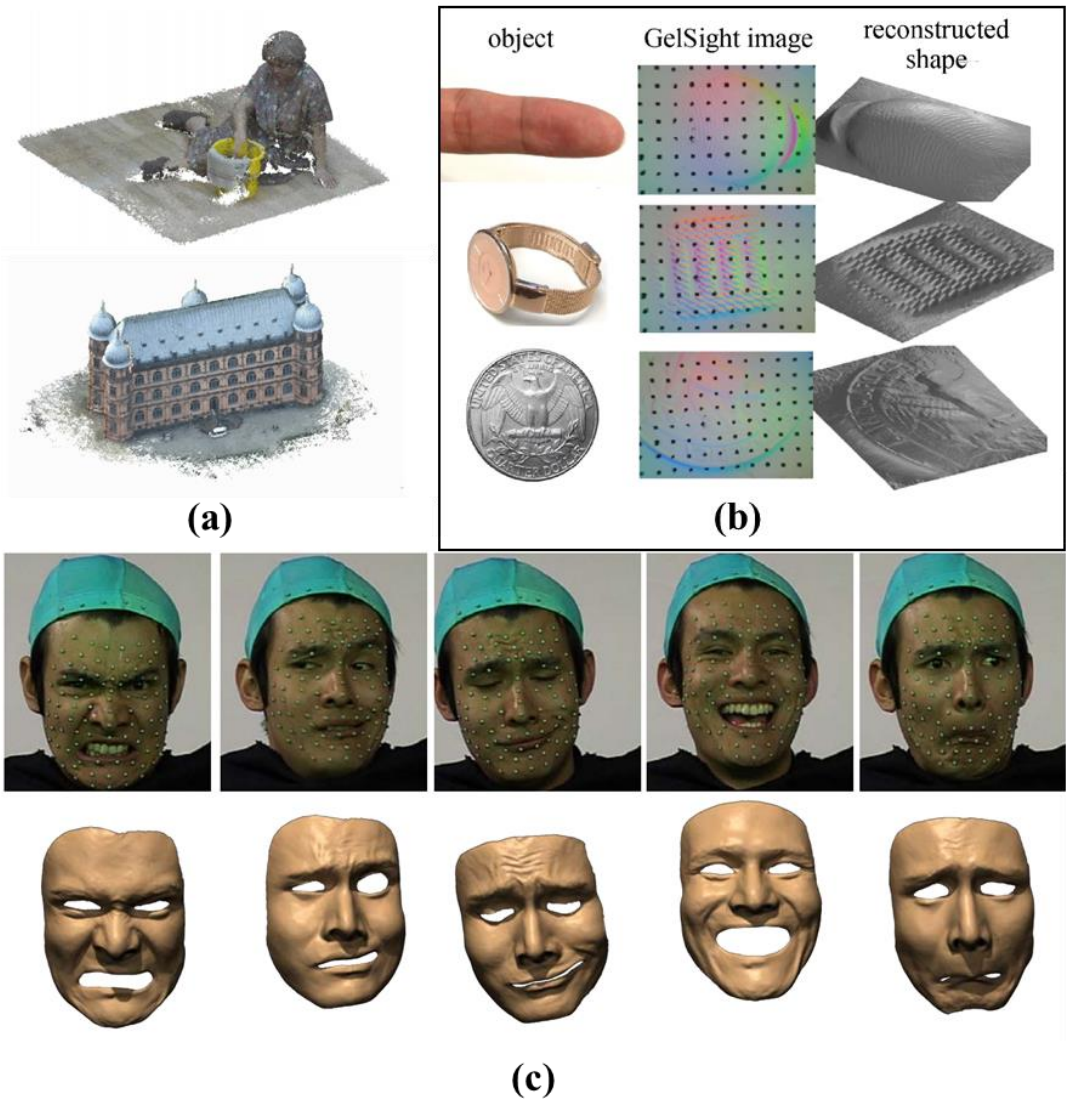

Figure 3.1 Examples of surface shape reconstruction using external sensing. **(a)** 3D point cloud data of large-scale objects reconstructed through photogrammetry [56]. **(b)** Detailed surface information from the Gelsight tactile sensor which uses CCD camera sensors [61]. **(c)** Facial expression recorded with a combination of motion capture markers and 3D scanning [60].

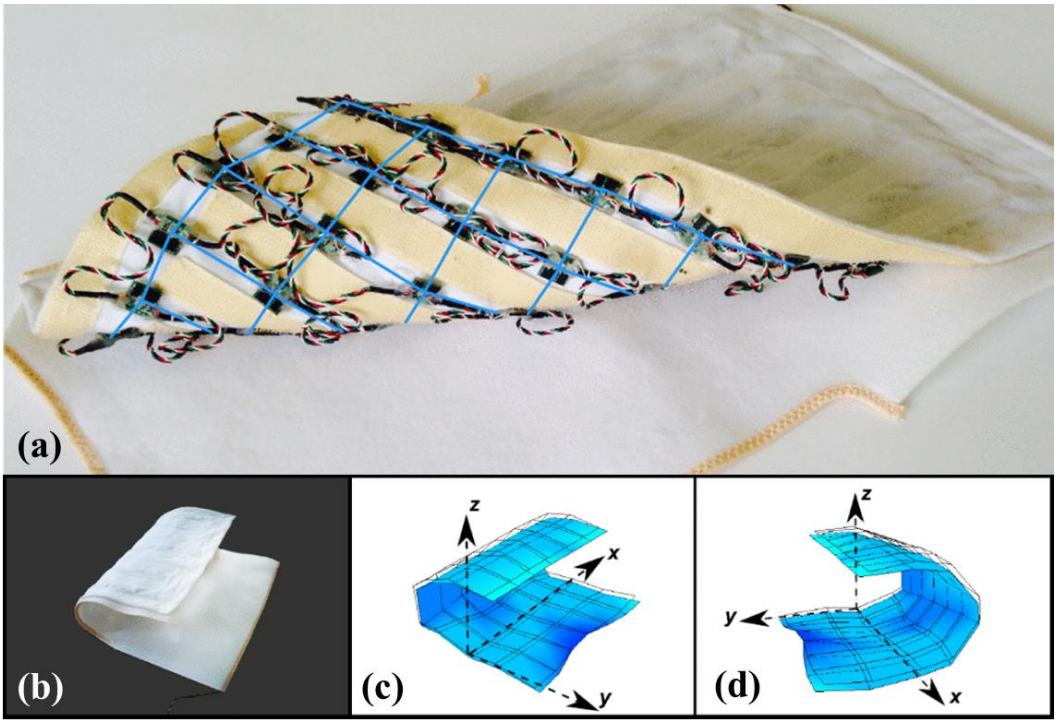

Figure 3.2 Example of a self-contained surface shape sensor. It utilises a grid of 3-axis accelerometers embedded in flexible fabric [63]. **(a)** Inside view of the accelerometer array and wiring. **(b)** Surface shape sensor bent 180°. **(c)-(d)** Virtually reconstructed surface shape.

The use of self-contained shape sensors is another approach to measuring flexible 3D objects. Small-sized contact-based sensors can be attached to objects for transducing the local position and orientation information. Microelectromechanical systems (MEMS) allow the integration of many miniaturized sensors to provide local information for global shape reconstruction. Surface shape reconstruction has been performed with a non-stretchable sheet of three-axis accelerometers arranged in a grid pattern [63, 64]. By using a high density of accelerometers (63 sensors total) they were able to reconstruct the global surface shape from local orientation measurements (**Figure 3.2**). Similarly, Cheng *et al.* [65] developed an artificial skin that consisted of rigid hexagonal sensor units based on accelerometers, which could provide the relative pose of each sensor. Saguin-Prynski *et al.* [66] described their work on 3D curve reconstruction from orientation measurements, and applied multiple curves for surface reconstruction. In work by Microsoft Research, a thin-film surface shape sensor was developed that consisted of 16 piezoelectric sensor nodes [67]. A non-stretchable plastic sheet was used as the sensor substrate with sensor nodes located around its edge, as shown in **Figure 3.3(a)**. A learning-based approach was used to model the surface shape, with ground-truth data captured with fiducial markers and stereo cameras (**Figure 3.3(b)**). Overall, a limitation of grid-type MEMS sensors is that they often have limited flexibility and stretchability due to fixed connections between nodes. Due to wiring, they are also complicated for large-scale applications.

More recently, liquid conductors, e.g. eutectic Gallium Indium (eGaIn) have been embedded in elastomeric substrates to measure strain in fully-soft sensors [68, 69]. These sensors are inherently compliant and have been designed as artificial skins that can be integrated into completely soft systems, like soft robots [70]. Their underlying sensing principle is similar to traditional strain gauges and are typically designed to be sensitive in one direction. They require contact electrodes on either end of the liquid-metal channels, which can make scaling to larger or more complex designs a challenging task. An example of an eGaIn design is shown in **Error! Reference source not found.(a)**, where two orthogonal layers are used to measure strain in two directions, and one spiral layer measures pressure. The sensor can measure overall strain and pressure, but the precise points where they occur cannot be detected.

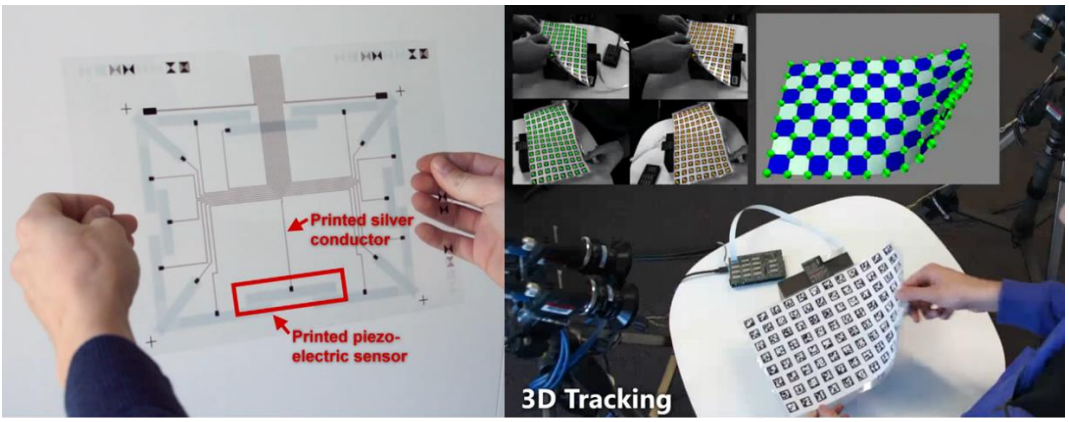

Figure 3.3 FlexSense surface shape sensor developed by Microsoft Research [67]. **(a)** Sixteen piezoelectric sensor nodes are embedded around the edge of a thin-film plastic substrate. **(b)** Ground-truth data obtained from fiducial markers and stereo cameras for the machine learning-based modelling.

Optical fibre-based sensors using fibre Bragg gratings (FBGs) are one of the sensor technologies that have proven performance in fields like civil engineering [71] and aerospace industries [72]. FBGs have excellent electromagnetic, immunity [73] and can be used in harsh environment [74], such as extreme high electromagnetic noise, vacuum and extremely low temperature. They can carry a high density of sensors on a single fibre [75] with small form factor and long-term stability [76]. 3D curve-based shape reconstruction based on FBG sensing has been increasingly applied for continuum robots [45], such as steerable interventional needles for biopsy and ablation [77]. However, these methods were specified for tube-shaped reconstruction, where FBGs are used to monitor the 3D curvature. To extend the application of FBGs in shape sensing, more designs have been proposed. Silva *et al.* [78] designed a wearable sensing glove for monitoring hand gestures and postures, in which a single FBG fibre was laid across a hand in a curvilinear layout.

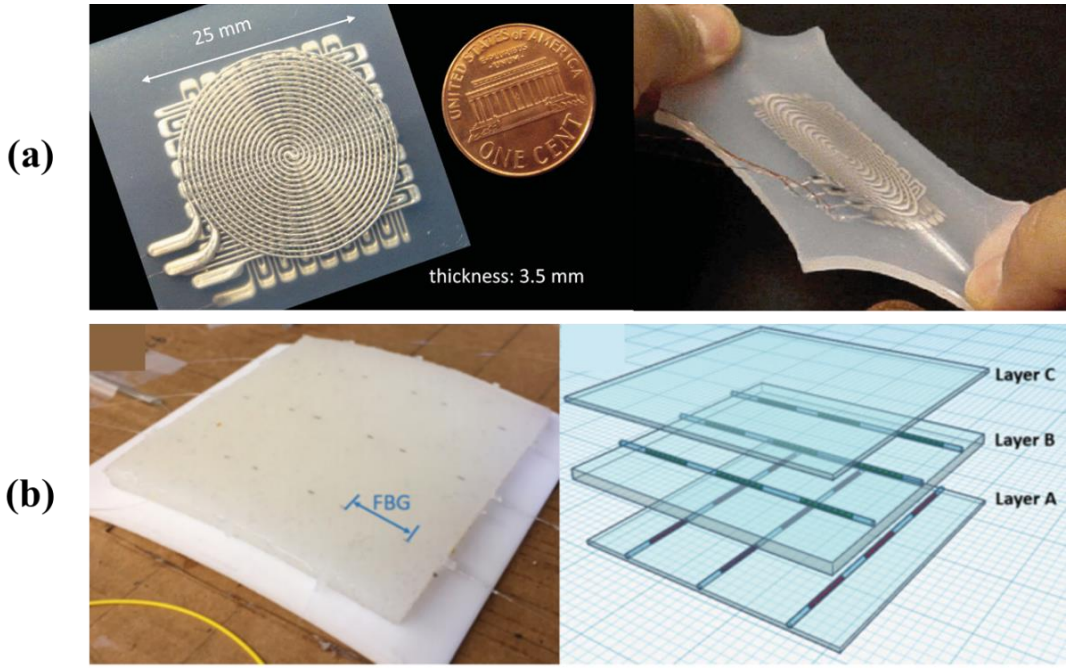

Figure 3.4 **(a)** Stretchable liquid metal (eGaIn) sensor for measuring 2D strain and 1D pressure [68]. **(b) S**urface shape sensor comprised of two orthogonal layers of FBGs [79].

In this design, the glove was able to show the hand motion in real time, however, this was achieved by measuring the bending angle of each finger joint, not from the shape of the hand itself. This creates dependence on the accurate placement of FBGs so that they align with the patient's finger joints. Xu *et al.* [79] implemented a 3D surface shape sensor (shown in Error! Reference source not found.**(b)**) where two orthogonal layers of 9 FBGs (18 FBGs total) could measure curvature in two directions at multiple points. An analytical model was used, that assumed constant-curvature bending for each FBG. It requires precise fixture of each FBG, such that the FBGs of each layer overlap. Zhang *et al.* [80] provided surface shape reconstruction algorithm for a large scale (800 × 800 mm) plate surface, with a net of orthogonal FBG strain sensors. The sensor can detect both convex and concave object surfaces, however, the use of a relatively rigid Plexiglas substrate limits the deformation to simple shapes. Additionally, for shape sensors employing orthogonal fibre layouts, the stretchability of the overall sensor substrate is limited, and depends on precise FBG positioning that strongly affects the reconstruction accuracy [81].

In this work, we design and fabricate a new flexible 3D shape sensor which can reconstruct the surface of the subject in real-time. Unlike most optical fibre-based shape sensors that can only measure the curvature change along the fibre, the proposed sensor can measure the complete 3D shape of its surface deformed by bending and twisting. A single fibre with sparsely distributed FBGs is embedded into a flat silicone rubber plate and used to measure strains on both top and bottom surfaces. Through finite element analysis

(FEA), we consider the effect of design parameters and validate the uniqueness of strain-to-shape mapping. The overall deformation is mapped to the optical signals using a machine learning approach. Although this introduces a dependence on the obtained training data, this approach can compensate for fabrication errors while eliminating the need for complex modelling and stringent allocation of FBGs. The presented sensor layout and design are easily tailor-made to specific applications. The main contributions of this work are:

- Development of a design framework for FBG-based surface morphology sensors. A single-core optical fibre with sparsely distributed FBGs was used to detect surface morphology in real-time.
- FEA to determine sensor design parameters with embedded FBGs. The mapping between surface deformation and fibre responses were proven to be unique for the proposed fibre layout.
- Machine learning-based modelling to enable more robust and reliable shape reconstruction without explicit knowledge of the FBG configuration/allocation.

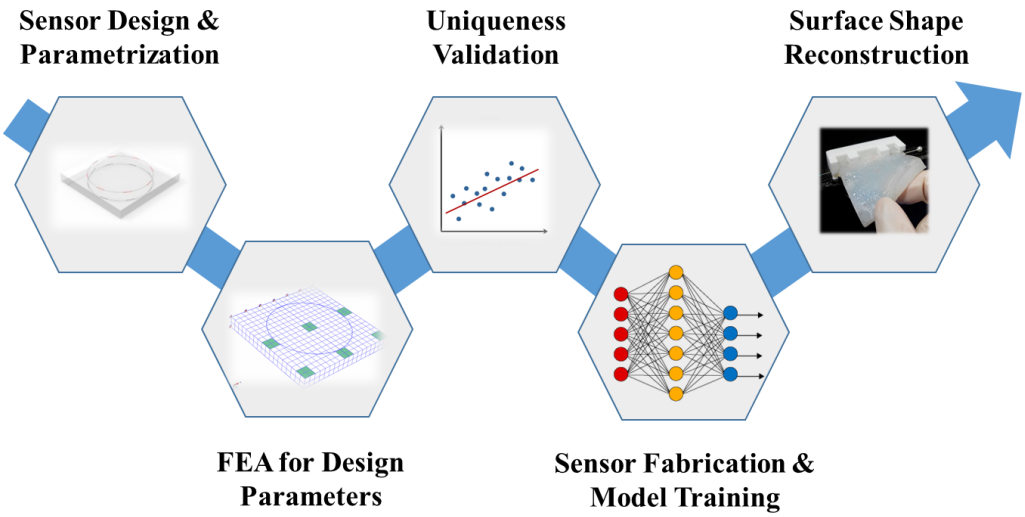

Figure 3.5 Workflow for the development of the presented surface shape sensor.

3.1.2 Sensor Design and Strain Analysis

3.1.2.1 Strain sensing with fibre Bragg gratings (FBGs)

The proposed sensing principle of our flexible shape sensor is based on the mapping between the local strains and global displacements. When the sensor is deformed by bending, twisting or other forms of deformation, the embedded FBG sensors are strained accordingly. The decomposed axial strains along the fibre are then converted to optical signals in which different strains would result in different wavelength components measured by the optical interrogator. An illustration of the operating principle of FBGs is shown in **Figure 3.6**.

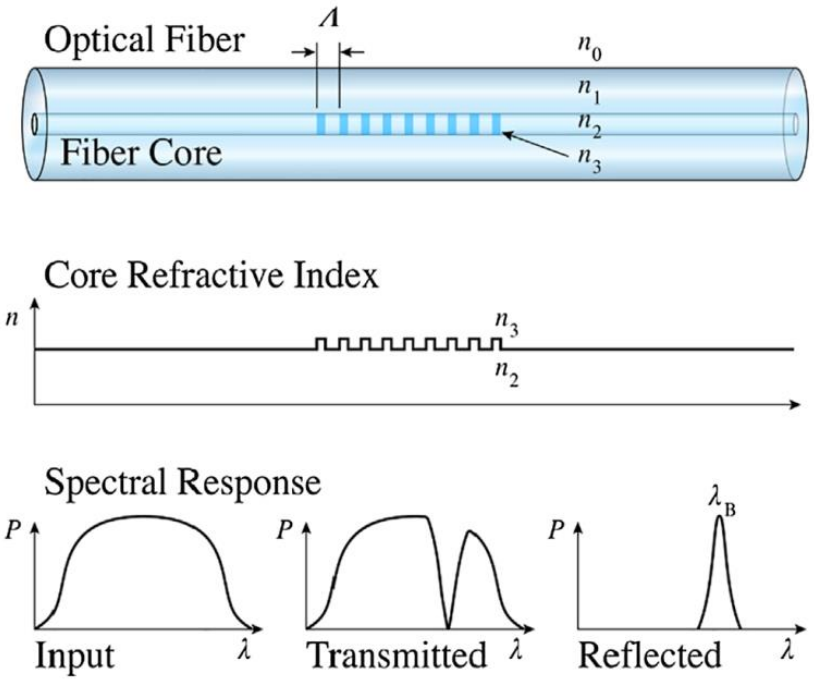

Figure 3.6 Operating principle of fibre Bragg gratings (FBGs) [82]. The gratings are periodic variations of refractive index inscribed into the fibre core and reflect a particular wavelength of light. The spacing between gratings determines the wavelength that is reflected, therefore strain can be measured based on the change in the reflected wavelength.

The shift in central wavelength of the each FBG depends on the effective refractive index and the grating period which are a function of temperature and strain. Therefore, the sensing response varies when our proposed sensor experiences temperature changes or under external forces. The mechanical strains change the grating period and the effective refractive index, resulting in shifts in Bragg wavelengths [83]. The operating principle of FBGs is illustrated in **Figure 3.6**. Including the effect of temperature, this allows strain and temperature measurements by the reflected FBG spectrum in real-time. This dependency is described as follows:

$$\frac{\Delta\lambda}{\lambda_0} = k\epsilon + \alpha_\delta \Delta T \tag{3.1}$$

where $\Delta\lambda$ is the wavelength shift, λ_0 is the base wavelength at fabrication, k = 0.78 is the gage factor, α_δ is the change of refraction index and ΔT the temperature change in K. The strain ϵ includes the mechanical-induced strain ϵ_m and the thermal strainϵ_t. Substituting $\epsilon_t = \alpha_{sp}\Delta T$ into equation (3.1):

$$\frac{\Delta\lambda}{\lambda_0} = k\epsilon_m + (k\alpha_{sp} + \alpha_\delta)\Delta T \tag{3.2}$$

where α_{sp} is the coefficient of thermal expansion of the substrate material. As the temperature has an impact on sensing signals, temperature compensation is performed to obtain precise mechanical strain measurements. An additional temperature grating is used to correct other strain measuring gratings. Substituting $\epsilon_m = 0$ into (3.2), its signal is calculated according to equation:

$$\frac{\Delta\lambda_c}{\lambda_{0c}} = (k\alpha_{sp} + \alpha_\delta)\Delta T \tag{3.3}$$

where λ_{0c} is the central wavelength of the compensation FBG. For the FBGs used in mechanical strain sensing, (3.2) can be rewritten as:

$$k\epsilon_m = \frac{\Delta\lambda_m}{\lambda_{0m}} - (k\alpha_{sp} + \alpha_\delta)\Delta T \tag{3.4}$$

and $\lambda_{0m}$is the central wavelength of the mechanical strain measuring FBG. Taking (3.3) into (3.4):

$$\epsilon_m = \frac{1}{k}\left(\frac{\Delta\lambda_m}{\lambda_{0m}} - \frac{\Delta\lambda_c}{\lambda_{0c}}\right) \tag{3.5}$$

Shifted wavelengths due to the mechanical strain ϵ_m can be calculated by subtracting the signal of the temperature-compensation FBG from the signal of the active strain-measuring FBG.

3.1.2.2 Design considerations

Flexibility – Sensors that integrate with soft, flexible structures must be adequately flexible to not inhibit the motion of the original structure. In particular for soft robotics, this integration should not alter the deformation actuated by the soft actuators. A thin optical fibre of ϕ195 μm ensures promising compliance with such morphological deformation, compared to electronics-based sensors that require complicated electrode wiring and that are inherently rigid. A single-core fibre has a high capability of multiplexing strain measurements through multiple FBGs. In our sensor design, each FBG should be short to detect local strain. The distribution of such strain sensing would be critical to reconstruct the shape in detail.

Stretchability – Stretching is a common form of deformation, especially for the motion of soft robots. Surface shape sensors are typically designed with grid-form sensing networks, however, this configuration can limit the degree of flexibility and stretchability especially when unavoidable in-plane loading exists, particularly in soft robots. Our proposed fibre layout in the sensor allows stretchability along different directions, and silicone rubber is chosen as the substrate layer for high compliance and firm bonding with common soft robots fabricated with silicone.

Reliability – The reliability of the sensor over time would define its usage in practical applications. FBGs provide excellent durability in harsh environments including dramatic temperature changes and chemical corrosions [84]. However, FBG-written fibre is still fragile under concentrated loading. In this work, Draw Tower Gratings (DTGs) are selected instead of conventional strip-and-recoat FBGs, as they offer over four times the mechanical strength.

As our first proof-of-concept sensor design, we chose a rectangular geometry for the sensor base to simplify its fabrication. The sensor base was moulded from a silicone rubber square and the FBG sensor is circularly wrapped on the top and bottom of the sensor as shown in **Figure 3.7(a)**. The FBG fibre is placed away from the midplane to enable sensor response to bending deformation. The overall design includes five layers: the middle sensor base substrate layer, two FBG sensor layers and two silicone protection layers. The protection layers are thin coatings above the FBG layers and have a small effect on sensor flexibility. The FBG sensor layer is shaped in circular form to obtain the strain information.

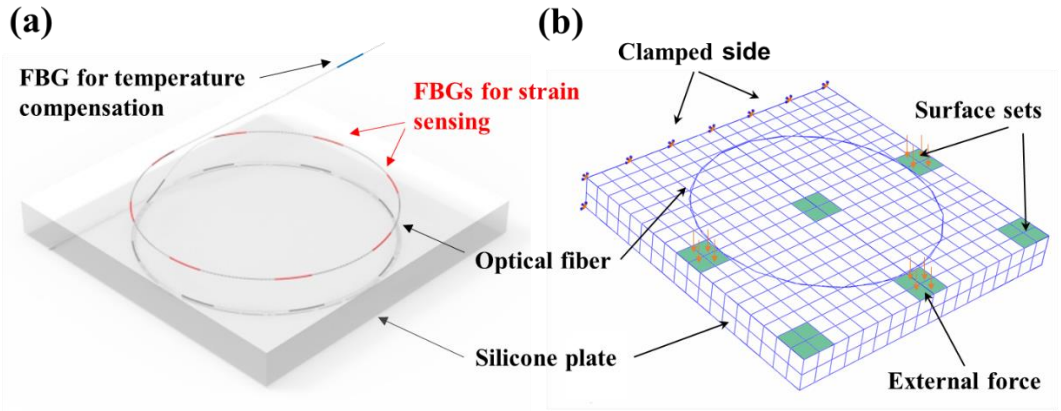

Figure 3.7 **(a)** Overview of the proposed surface shape sensor structure: a single fibre is looped in two circles away from the midplane. Each circle contains 8 FBGs. **(b)** Finite element model of the sensor. The silicone plate is discretised into 3D 8-node continuum elements and the optical fibre is discretised into 3D 2-node truss elements. 12 surface sets (6 shown in green) are predefined to apply random pressure loadings for simulating the external forces.

3.1.3 Design Study using Finite-Element-Analysis

In our work, we make use of FEA to analyse the relationship between the sensor global displacements and the local strains. Validation through FEA allows us to see the effect of parameters like sensor thickness, and to ensure unique sensor responses prior to fabrication. The side length of the square sensor was chosen to be 45 mm in our prototype. In this research, two selected parameters are studied with FEA. Proper fibre layer offset and sensor thickness are studied to evaluate the sensor performances. The estimated and predicted sensor responses of the sensor are computed with Abaqus 6.14. Only a short summary of the FEA modelling is presented in this section. For more details, please refer to the full publication [85].

3.1.3.1 FEA modelling

The finite element model of the sensor is shown in **Figure 3.7(b)**. The silicone sensor base and the sensor fibre are modelled as 3D deformable models. The protection layers (0.2 mm thick) are not included in the simplified finite element model as it has a negligible effect on the uniqueness of the sensor response.

The silicone plate model is meshed to 2×18×18 C3D8RH elements and the sensor fibre is meshed to 44 T3D2H elements which are 2-node linear 3D trusses that only allow axial strains. For silicone rubber (Smooth-On Ecoflex 0030), it is modelled as a hyperelastic material using Ogden strain energy potential. Parameters of the 3-term Ogden model are adopted from literature [86]: μ_1 = 0.024361, μ_2 = 6.6703 × $10^{-=}$, μ_3 = 0.45381 × 10^{-}, α_1 = 1.7138, α_2 = 7.0679, α_3 = -3.3659, D_1 = 3.2587, D_2 = D_3 = 0, where μs, αs and Ds are temperature-dependent material parameters. The units for μs and Ds are MPa and

$(MPa)^{-1}$ respectively, whilst αs are dimensionless. To model the mechanical behaviour of the fibre, a linear elastic model is used with elastic modulus 70 GPa and Poisson's ratio 0.16 [87].To simulate sensor response under different loading conditions, one edge of the sensor is prescribed with the clamped condition while others are free. All the simulations are done under static loading steps. To generate deformations such as bending and twisting, surface loads are applied on twelve surface sets. They are arranged symmetrically on the top and bottom surface of the sensor, with those on the top surface (green) in **Figure 3.7(b)**.

3.1.3.2 Design parameter analysis

Other than the width of the sensor, two other key parameters of the sensor should be determined in advance, i.e. the fibre layer offset h and the sensor thickness t. According to the Kirchhoff plate theory, the material element would experience a strain which increases with the offset distance from the neutral plate. Simulation with FEA was also conducted and the results were in agreement. Therefore, to maximize the sensitivity of the sensor, the fibre layer offset was set to the maximum value, i.e. the two fibre layers would be put on the upper and lower surfaces of the substrate.

Since the fibre layers were selected to be on the surface of the sensor, the overall thickness governs both the sensor sensitivity and flexibility. To investigate the effect of changing sensor thickness, sensor responses were obtained through FEA such that the sensor was placed on two supporting pins and subjected to a loading force generated by a cylinder with radius 20 mm. At step = 1.0, the sensor is bent to the same radius by pushing the cylinder. For the soft and flexible sensor, the low thickness would be an advantage when integrating the sensor on actuators and other components for flexibility. However, as single core fibre is used in this work, the fibre needs to be offset from the mid-plane and with a suitable thickness to differentiate between deformation patterns. The thickness t is determined by considering the strain patterns with varying thickness (2.5 – 7.5 mm). The range was selected by considering reasonable sensor thicknesses that would not inhibit flexible motions. The strain responses of the proposed sensor were simulated under bending for 2.5 mm, 5 mm, and 7.5 mm thicknesses, with simulated strain responses shown in **Figure 3.8**. It was found that the strain responses were greater for larger thicknesses, due to the increased offset of the fibre layers from the neutral axis. The FBGs were less sensitive to compression than tension, but the strain responses also increased with thickness. Although a higher sensitivity to strain is welcomed, the increased thickness of the sensor reduces flexibility and increases the likelihood of damaging the fibre. Therefore, 5 mm sensor thickness is selected for this prototype. Depending on the application and sensing requirement, the sensor thickness can be adjusted for optimal performance.

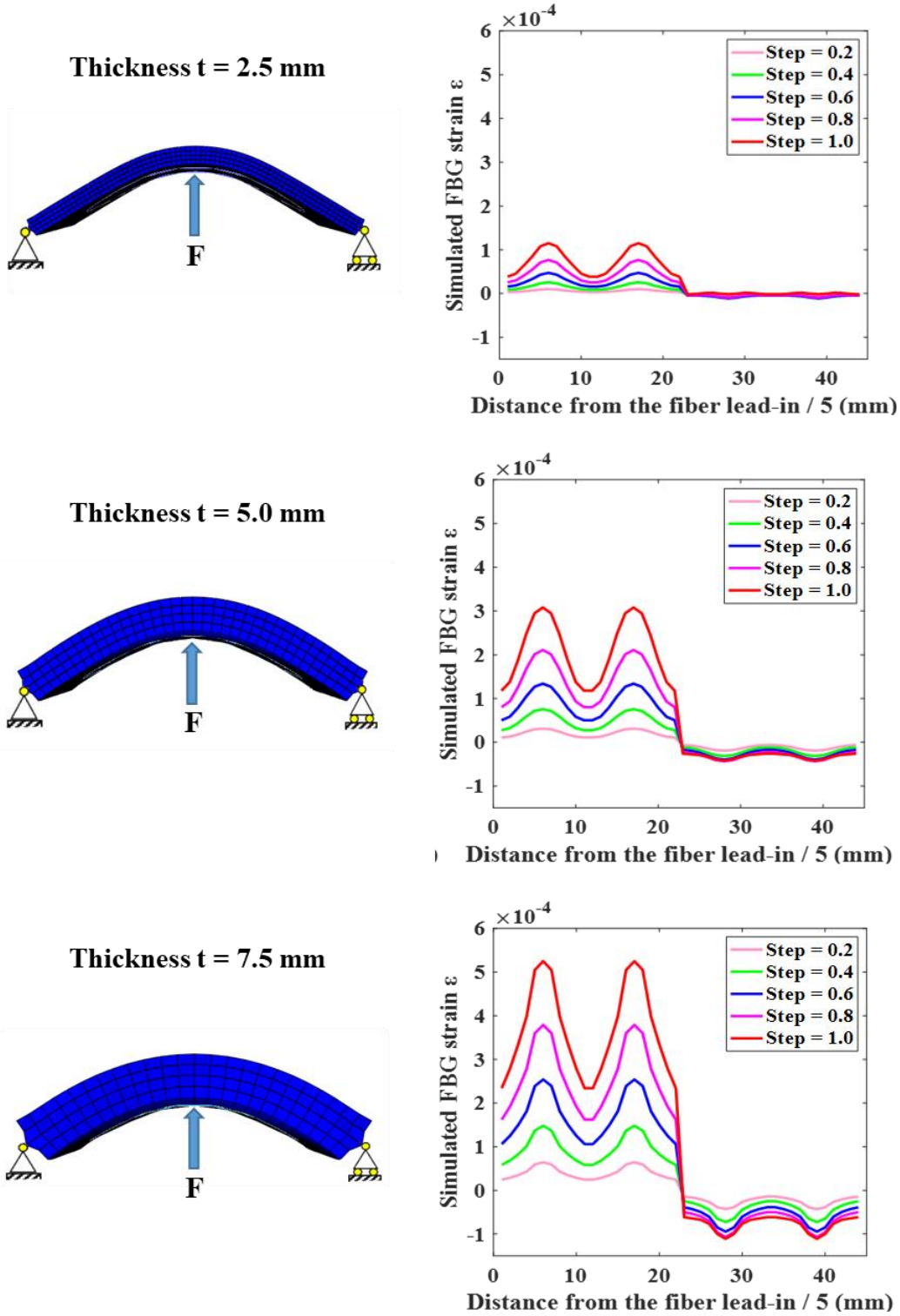

Figure 3.8 Simulated strain responses of the sensor under 3-point bending at different thicknesses. The fibre layers were located at h = ±0.5t. The magnitude of the strains increased proportionally with the sensor thickness, i.e. the sensor becomes more sensitive to deformation.

3.1.4 Data-driven uniqueness and modelling

To reconstruct the surface from local strains, a model which could map from the strain data to the surface deformation is needed and the uniqueness of the mapping should be guaranteed. Conventional methods build kinematics models with complicated mathematical analysis, which typically require highly accurate fabrication or error compensation. We apply a data-driven approach, namely an artificial neural network (ANN), to tackle the modelling problem and for validation of the sensor's uniqueness.

From the modelling perspective, data-driven approaches are beneficial for compensating errors induced during fabrication, or when sensor positions are not explicitly known. It allows flexibility in fabrication and design, making it easier to customize the sensor to different applications. For validating the sensor's uniqueness, we use data generated from our FEA model to train a separate ANN. In both ANNs, a typical multilayer feedforward network with two layers is built, but different backpropagation methods are used for uniqueness validation and modelling. The hidden layer contains 10 neurons which connect to the inputs and the second layer produce the network outputs.

3.1.4.1 Uniqueness validation with FEA

Initially in our FEA validation, bending, twisting and random loading are tested to analyse the uniqueness of the model. Pressure loading was applied to the highlighted surfaces to cause deformation, as shown in **Figure 3.7(b)**. The use of pressure loading creates a smooth deformed surface without applying a concentrated force on a particular element or node. Under different deformation patterns, the strain responses are notably different, indicating that different shapes could be reconstructed uniquely. Moreover, for the same shape in opposite directions (e.g. bending up versus bending down) similar strain response patterns are observed, but inversed, due to the double-layer fibre layout of the sensor. Three example deformations with their reciprocal deformations are shown in **Figure 3.9**. The strain in the FEA modelled fibre are the measured elastic strain component E11. It is also noted for the same deformation pattern at different magnitudes of deformation, the overall strain response patterns remain the same, while the strain peaks increase with the deformation magnitude.

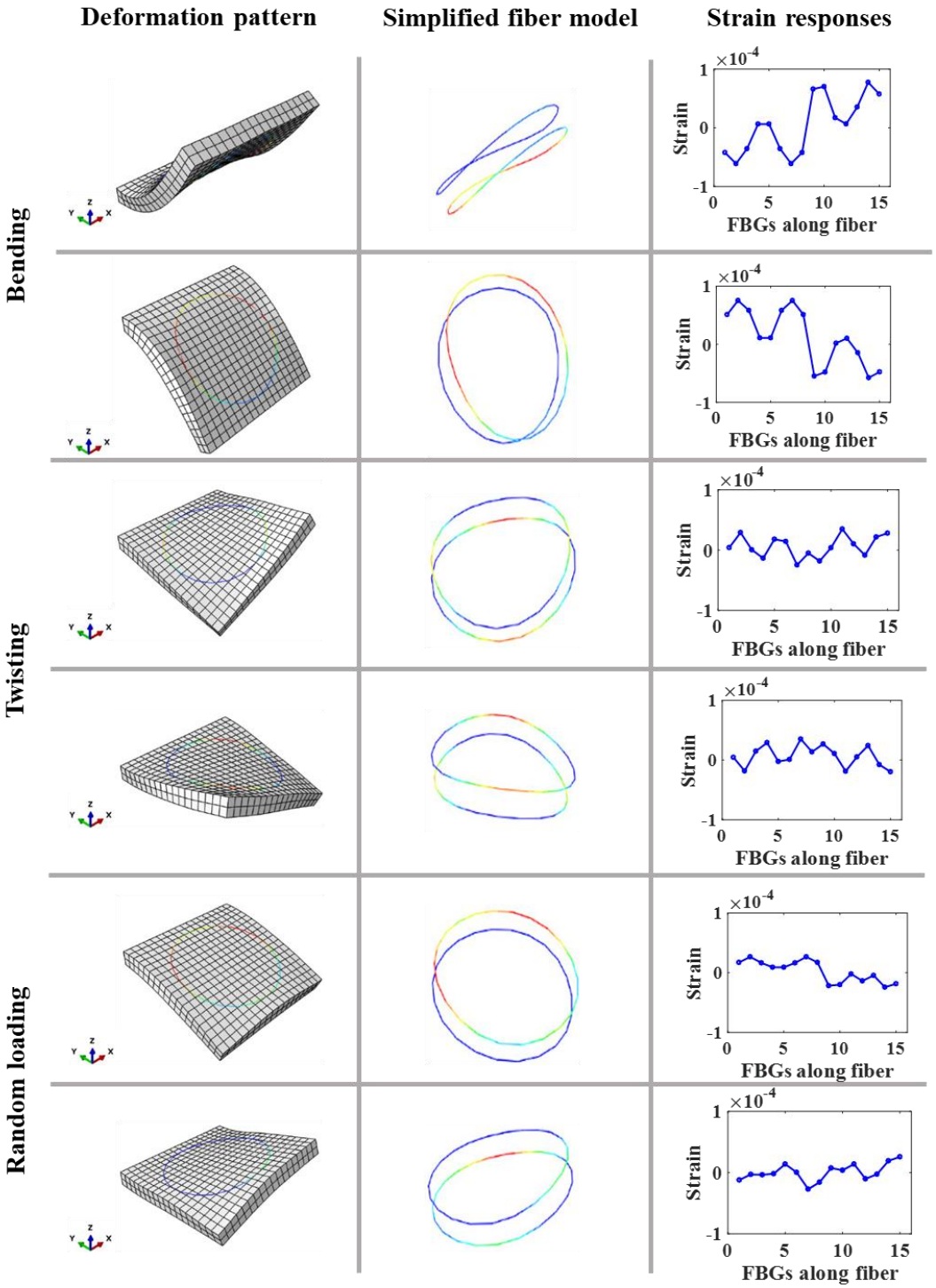

Figure 3.9 Simulated fibre strains under three types of deformation and their reciprocals. The 1st column depicts the FEA model of the deformed shape sensor. The 2nd column shows the strain induced in the simulated fibre with warmer colours indicating larger strain. The 3rd column shows the corresponding discrete strain measurements along the fibre.

3.1.4.2 Uniqueness Validation using ANN

To further validate the sensor's uniqueness, a large number of simulated strain responses and corresponding surface displacement data were extracted from the FEA model for training of an ANN. Within a defined range of pressure, 729 simulations with random pressure loadings were gathered, where each contains 10 steps, thus 7290 data sets were generated. The inputs to the neural network are the 16 sparse axial strains in fibre truss elements and the output nodes are from 1083 (19×19×3) displacement data. Scaled conjugate gradient backpropagation was used, since the network is large and requires less memory for calculations, whereas Levenberg-Marquardt (L-M) backpropagation was used for reconstructing the actual surface shape in **Section 3.1.6.2** because it requires more memory than other algorithms and we use fewer output nodes for the shape reconstruction (9×9×3=243). L-M backpropagation also has amongst the fastest training times when compared to other algorithms (e.g. scaled conjugate gradient backpropagation) in the Matlab toolbox.

The neural network performance is evaluated by mean-squared-error (MSE) between the FEA-simulated displacement in the experiment and the output displacement from the trained network. The training stops when the magnitude of performance gradient is less than $1e^{-6}$ or the validation performance stop decreasing. Cross-validation is employed to prevent over-fitting in which 70% of the data is used for network training, 15% is used for validation and the last 15% is used for testing. The results showed a good fit with a R^2 value of 0.989 and the overall errors are small. The high accuracy of regression implies that, within the sampled range, the relationship between the surface displacements and FBG strains are unique.

3.1.5 Sensor Fabrication

3.1.5.1 Fabrication approach

The fabrication can be performed as the size and other parameters have been determined. Ecoflex silicones were chosen due to their low viscosity that favours mixing and de-airing in fabrication. A mixed portion of silicones were degassed and injected into 3D-printed moulds which were coated with releasing agent. After demolding the patterned silicone plate, the top and bottom surfaces of the plate a channel was created with a needle for passing the fibre. Small pins were used to temporarily fix the fibre shape on the silicone plate, preventing the fibre from returning to its neutral position. A thin layer of silicone epoxy (ELASTOSIL® E41) was applied to partially seal the optical fibre and silicone plate. Finally, the pins were removed and two thin silicone coatings (with the same material as

the silicone plate) were placed and bonded firmly on the top and bottom surface of the silicone plate as protective layers.

In the proposed sensor layout, the embedded fibre is wound in a circular fashion, which means that the centre and corners of the sensor have no underlying FBGs. For any local deformation that occurs on the side of the sensor, strains will still be imparted to the nearby FBGs due to the inherent stiffness of the silicone substrate. For deformations at the centre of the sensor, it is expected to generate global grating responses but with lower magnitude, since the gratings are surrounding the centre but not aligned with the resultant strain in the FBGs.

3.1.5.2 Fibre specifications

The fibre is embedded with FBGs that are made from intense ultraviolet light exposure on the optical fibre core. A fixed index modulation, i.e. a grating, is created and increased the core refractive index. The fibre has a cladding diameter of 125 μm and is coated with Ormocer with total outer diameter of 195 μm. Each grating has a length of 5 mm and are separated with a 10 mm gap for the first 16 FBGs and 450 mm between 16th and 17th FBG. 16 FBGs covered two surfaces of the silicone plate to capture strain information. The remaining FBG is placed outside of the silicone substrate and used as a temperature compensation sensor by subtracting its wavelength shift from other sensor readings. This assumes that the temperature compensation FBG is unaffected when the silicone substrate is deformed. FBGs with shorter wavelengths are located nearer to the lead-in end. The number of gratings, the separation between gratings, and fibre length can be tailor-made for each desired application, providing excellent flexibility in sensor design. In this study, we use a Wavelength Division Multiplexing (WDM)-based fibre system. Although other multiplexing methods (e.g. Optical Frequency Domain Reflectometry, or OFDR) can provide a greater number of FBGs per fibre, WDM offers low cost, simplicity, and high frequency sampling [76]. An OFDR system is used for multi-core shape sensing in **Section 3.2**.

3.1.6 Experimental Setup, Results, and Discussion

3.1.6.1 Data input and sampling for model training

The unique strain-shape mapping for surface shape reconstruction was investigated with FEA alongside the analysis of different sensor parameters. The corresponding surface sensor was then fabricated. To train a model for surface shape reconstruction, ground truth data must be recorded such that the surface morphology and FBG responses are capture simultaneously. The setup for obtaining ground-truth data is depicted in **Figure 3.10**. the

fabricated sensor is clamped at one side to ease the validation. *Nine* grid points on the sensor surface were chosen, where reflective markers were attached. Their 3D positions were measured by two infrared (IR) tracking cameras (Optitrack Flex 3). The tracking rate was 100 fps and the mean positional error was 0.015 mm.

The optical fibre is connected to a WDM-based interrogation system in which an invisible broadband light (Amonics ALS-CL-18) is transmitted to the optical fibre via an optical circulator (PIOC-3-CL). Light is reflected due to the change in core refractive index which is strain dependent and is captured by a small FBG interrogator (I-MON 512 USB) from the output port of the optical circulator. The interrogator can be used with up to 70 FBGs with a wavelength resolution > 0.5 pm and a maximum measuring frequency of 3000 Hz.

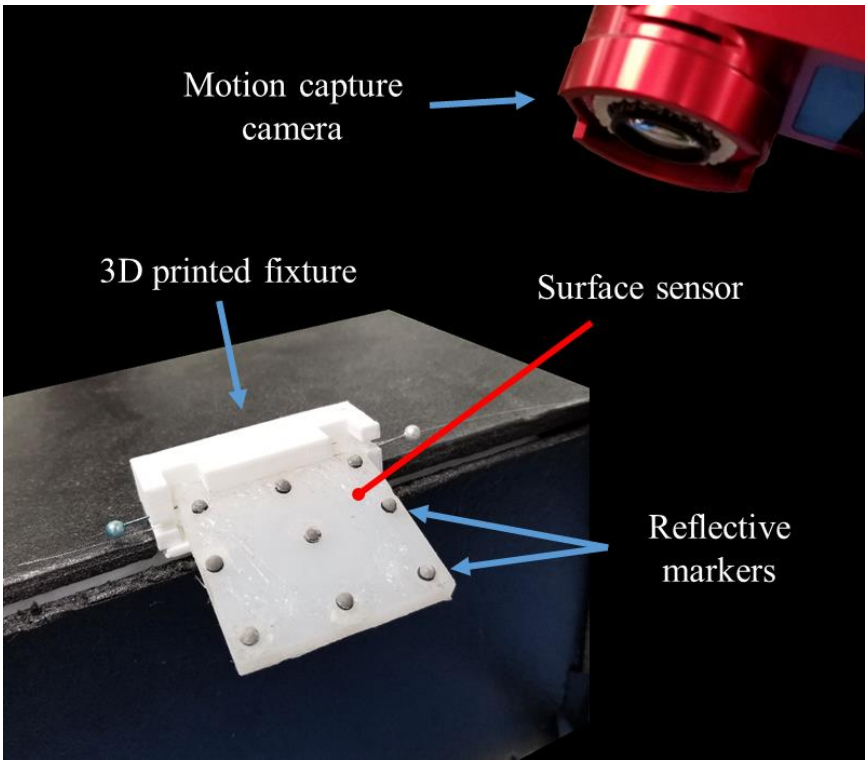

Figure 3.10 Experimental setup for the collection of ground-truth data. One edge of the sensor is fixed with a 3D printed part. A motion capture system provides the 3D position of 9 reflective markers on the surface of the sensor.

To build a learning model for surface shape sensing, 1000 IR-tracked sensor configurations, along with their corresponding Bragg spectrum, were captured, then used for ANN training with L-M backpropagation. Since there would be fabrication defects, such as fibre dislocations within the silicone substrate or uneven stiffness distribution, it is advantageous that no additional calibration is required when using this machine learning approach. Error induced by these defects are compensated by the ANN training. Defects

exist even with industrial manufacturing processes and are generally difficult to be considered in analytical models.

3.1.6.2 Surface reconstruction performance

The sensor was bent and twisted manually to form various configurations without blocking any of the 9 optical markers from the IR-tracking. At each time point, 16 Bragg wavelengths were measured. The shifted wavelengths act as inputs to the ANN, which are proportional to the actual change of strain at the corresponding FBG location. The 3D displacement of the 9 markers, twenty-seven (9×3) variables in total, are then defined as outputs. The ANN is then trained to model such a mapping from these inputs to outputs (Training time: ~4s, Window10, 8G RAM, i7-7500U). To reconstruct the surface shape, a linearly-interpolated surface is fitted from the 9 node displacements outputted from the model. Examples of the shape sensing is shown in **Figure 3.11**, where the surface is reconstructed based on displacement coordinates estimated by the ANN outputs. The reconstructed surface motion was obtained in sync with the deformation. The surface reconstruction update frequency is approximately 10 Hz within the Matlab environment and could be improved with other plotting software.

The sensing error can be obtained by comparing the ANN-estimated output coordinates with the IR-tracking ground truth. The error of each node was tested over 150 test data (not used in the ANN training), for which each sample has 9 nodes, totalling 1350 instance samples. The name of each node is illustrated in **Figure 3.12(a)**, where nodes in row A are closest to the fixed edge. **Figure 3.12(b)** shows the histogram of the nodal position errors throughout the 1350 instance samples. Majority of the node displacement errors were below 2 mm. Larger errors are seen in nodes further from the clamped side (fixed edge), i.e. nodes C1~C3. The root-mean-square error (RMSe) was about 1.8 mm for nodes C1~C3. In contrast, the nodes A1~A3, and B1~B3 had smaller errors, with RMSe at 1.17 mm across all nodes. In general, the node displacement errors increased with the distance from the fixed end. This could be attributed to the distribution of node positions in the ANN training data. Every node has the same total samples for training, however the nodes at the free end, C1~C3, have a larger displacement range, when compared with nodes A1~A3 and B1~B3. This results in less spatially dense sample points, and hence poorer training performance for the distal nodes. This may be a primary cause for the increased reconstruction error at nodes C1~C3 (**Figure 3.12(c)**).

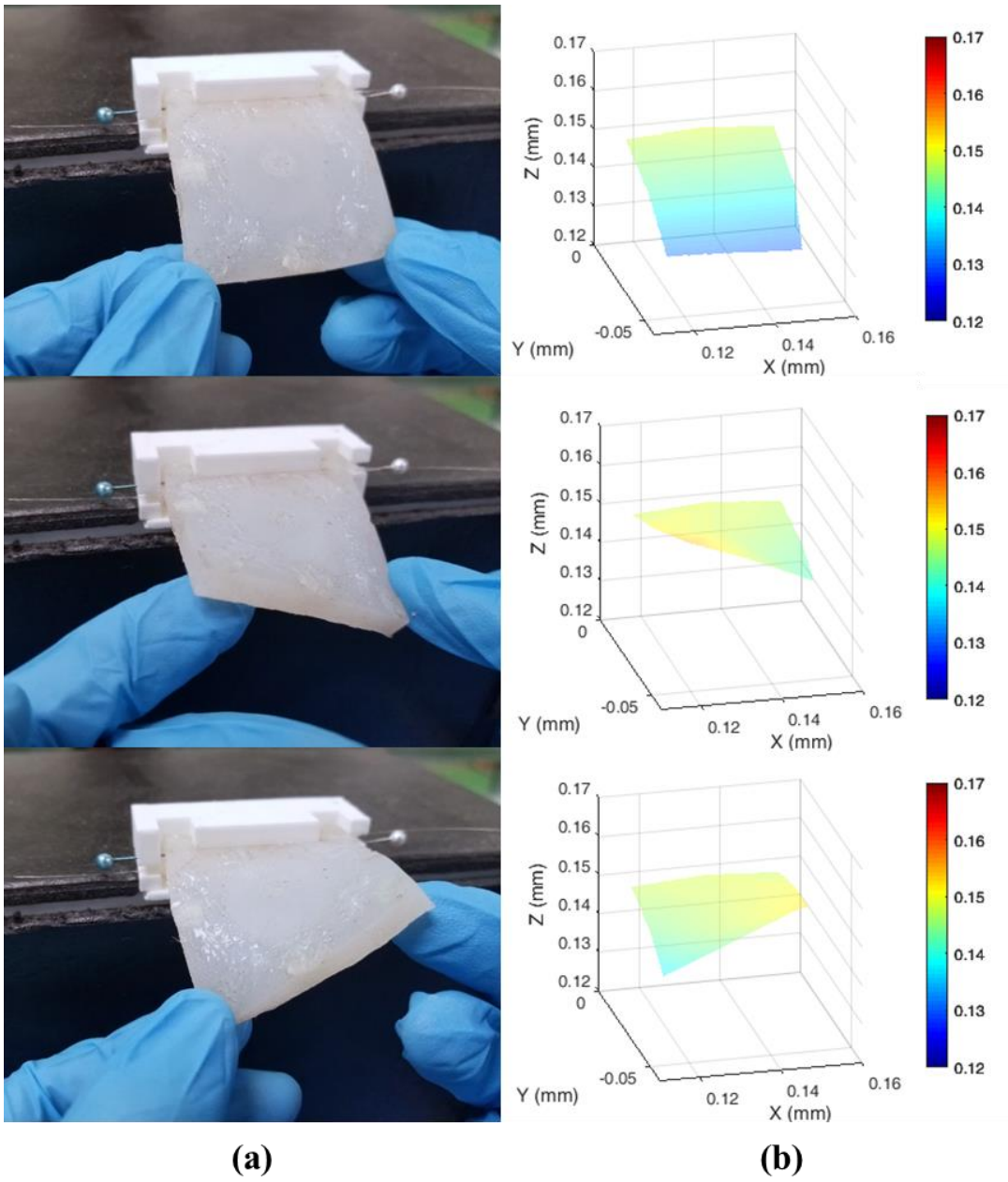

Figure 3.11 Sample shape reconstructions for the developed surface shape sensor. **(a)** Sensor deformed by hand. **(b)** Corresponding surface shape reconstructed with the trained ANN model. The colorbar indicates the depth of the reconstructed surface.

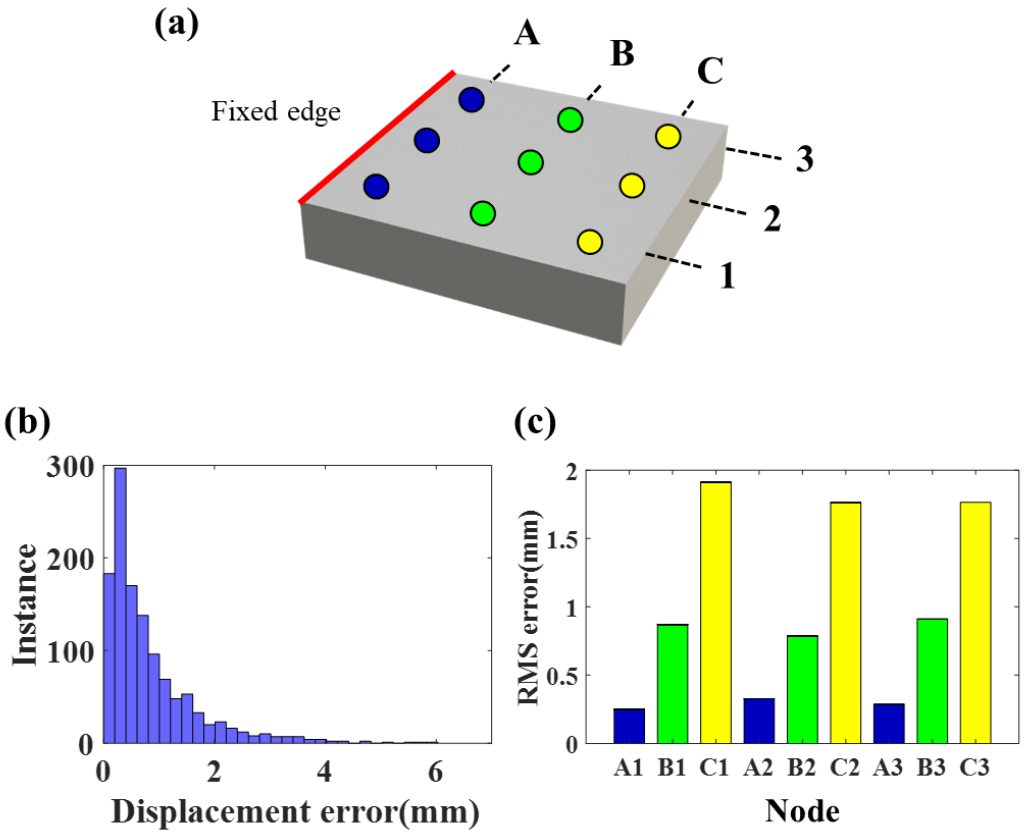

Figure 3.12 Accuracy analysis based on 1350 samples of test data. **(a)** Naming convention for the sensor nodes. The nodes in row A are closest to the fixed edge. **(b)** Histogram of the nodal displacement errors. Majority of the errors remained below 2 mm. **(c)** Distribution of nodal errors expressed as RMSe. Nodal error increased with distance from the fixed edge.

Reliability tests were performed to ensure consistent responses over a long operating period. Numerous repeated cycles of sensor motion were generated by 3 linear actuators, which pushed/pulled the nodes *C*1~*C*3 along an approximately 2 cm vertical path. As illustrated in **Figure 3.13(a)**, the sensor was bent upward, downward and finally back to the neutral position in 2 seconds. A total of 1000 bending cycles were conducted over 50 min, with Bragg wavelength responses recorded at the peak of upward motion. **Figure 3.13(c)** shows the reflected wavelength shift of eight FBGs on a layer over the cycles. It can be observed that the wavelength shift values fluctuate slightly around a constant value. The boxplots in **Figure 3.13(d)** show the distributions of the eight wavelength shifts. The wavelength fluctuations remained below 0.011 nm for all FBGs, corresponding to ~0.3 mm displacement. This indicates that the sensor can maintain stable and reliable responses throughout 1000 deformation cycles.

The signal-to-noise ratio (SNR) for the bent-up configuration is 14.9dB, calculated by comparing the vertical displacements of the distal node and noise. The hysteresis of the sensor was also evaluated by repeatedly displacing the distal side of the sensor (nodes C1 to C3) upwards by 20 mm and returning to the neutral flat position (3 cycles at ~1 Hz). The vertical displacement was provided by a linear actuator, and the vertical position of the node C2 and the wavelength shift of the FBG with largest shift was recorded. Small disparity between the bending up and return motion was found, as shown in **Figure 3.13(e)**, suggesting a low level of hysteresis in the presented sensor. To test the resolution of the sensor, a range of vertical displacement steps ranging from 0.1 mm to 1 mm were applied to the distal sensor side. The sensor could detect displacement changes down to the applied 0.1 mm displacement, suggesting that the sensor resolution is 0.1 mm or lower.

Despite the reasonable flexibility and stretchability of our sensor prototype, the allowable strain caused by purely in-plane loading is still small. It is primarily limited by the axially rigid optical fibre that constrains deformation. In combination with the sensor's small size, more complex deformations could not be measured without risk of damage to, or displacement of the fibre. The sensor flexibility could be further enhanced by altering the fibre layout, and will require consideration of other factors such as fibre length, number of FBGs, as well as the trade-off against the overall sensor sensitivity. Another limitation of the proposed sensor is the pressure sensitivity. Applying pressure to the sensor can induce strain in the FBGs without causing large deformation of the surface itself. This may cause incorrect shape reconstruction using our current approach. We will investigate techniques capable of distinguishing local pressure stimuli from the general shape reconstruction. This could enable simultaneous measurement of shape and force, which is particularly important for haptics applications, and ultimately reduce reconstruction error. Furthermore, in this work we compensate ambient temperature changes near the sensor, however there is still difficulty in compensating local temperature changes for each FBG, which is an inherent disadvantage of using one single-core fibre. Additionally, the use of a machine learning reconstruction approach places heavy reliance on the training data to achieve accurate shape reconstruction. For larger surface sensors developed with this approach that can achieve more complex bending shapes such as folding, it may be difficult to obtain sufficient training data to cover all possible deformations.

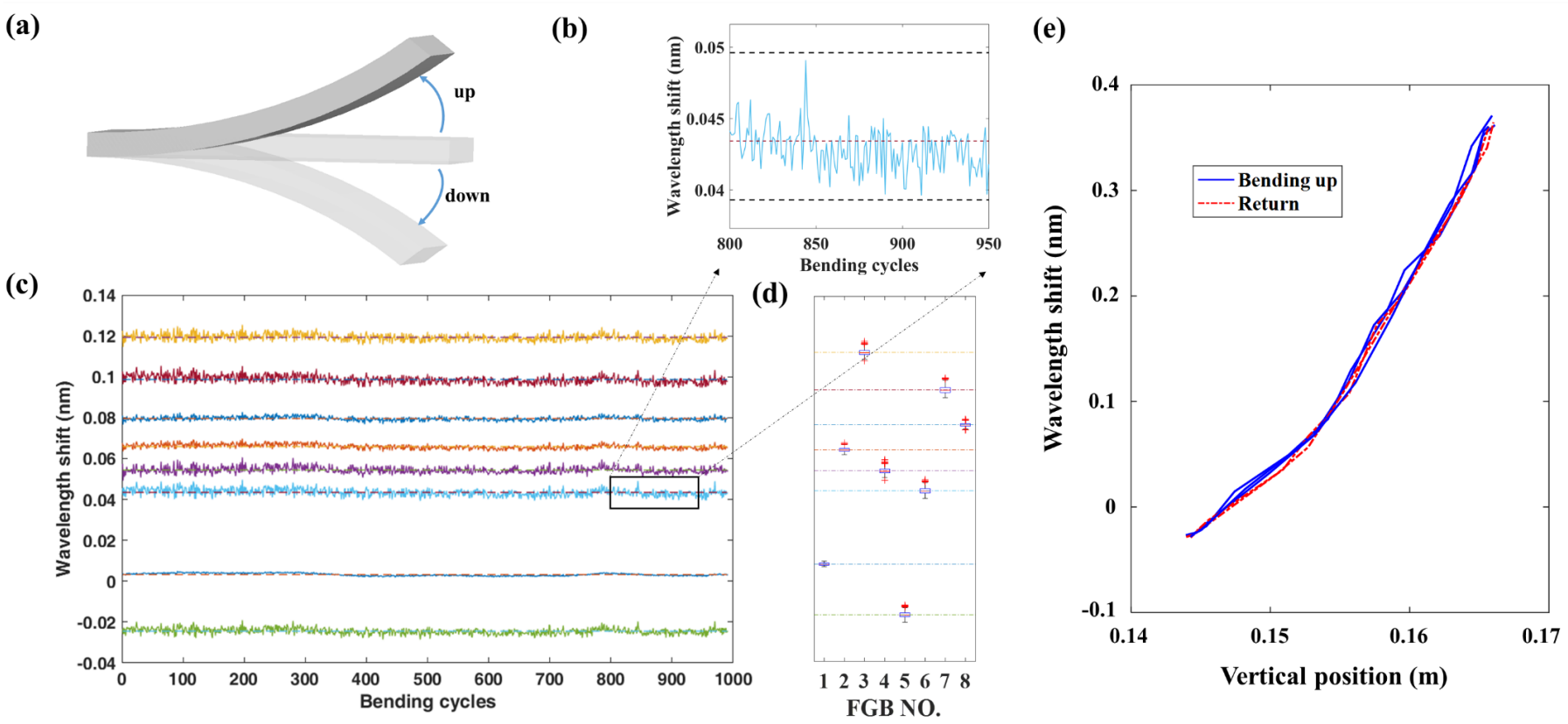

Figure 3.13 Repeatability tests of the proposed shape sensor under periodic loading. **(a)** Sensor is clamped to a fixture and bent along the free end by 3 linear actuators. 1000 cycles of such bending were conducted in 50 min. **(b)** Zoomed in view of wavelength shift fluctuation for the 6th FBG. **(c)** Wavelength shifts of the 8 FBGs on the first layer were recorded at the peak of upward bending. Over the cycles, the shift values showed small fluctuations about a constant. **(d)** Boxplots showing the distributions of wavelength shift. Fluctuation for all FBGs was less than 0.011 nm, corresponding to ~0.3 mm displacement. The standard deviation for FBGs 1-8 are as follows: 6.4×10^{-4} nm 1.2×10^{-3} nm, 1.7×10^{-3} nm, 1.6×10^{-3} nm, 1.5×10^{-3} nm, 1.8×10^{-3} nm, 1.9×10^{-3} nm, 9.6×10^{-4} nm. **(e)** Hysteresis plot comparing vertical position of the distal node C2 and wavelength shift of the FBG with largest shift. The sensor was bent up and returned to the flat position for 3 cycles.

3.1.7 Conclusions and Future Work

In this work, a high-performance surface shape sensor is presented. Provided with sparsely distributed strain measured by FBGs along a single-core optical fibre, we have demonstrated that the soft sensor surface shape can be promptly reconstructed using a machine learning algorithm. The sensor makes use of sparse FBG data provided by a WDM-based fibre system. Prior to the sensor fabrication, FEA was conducted to characterize the sensor parameters, such as to predict the sensing strains, and their accuracy, as well as the uniqueness of mapping between the fibre strains and the sensor surface. Our proposed sensor prototype is able to virtually reconstruct a flexible surface in real-time. The sensing accuracy and reliability have also been experimentally validated. The sensor achieved an accuracy of RMSe = 1.17 mm for reconstructed node displacements, which is also a reflection of the dependence on training data quality. For 1000 repeated cycles of motion applied on the sensor, the measured node displacements remained under 0.3 mm, demonstrating reliability in response to the repeated deformation. In general, these outperform various electronics-based shape sensors, (despite just very few reported) particularly in the aspects of complicated fabrication, electrodes and cables handling.

Based on the proposed design framework, a sensor could be used on the surface of a soft robot to improve interaction with the environment. We demonstrate this in a preliminary study using a single-core fibre with 16 FBGs embedded in a spiral shape on a silicone tube. In this case, only the overall bending shape of the tube was reconstructed, with ground truth data obtained using four EM trackers placed along its length. Example shape reconstructions are shown in **Figure 3.14**. Further improvement to this could aid in advanced soft robotic control where shape sensing, haptic sensing and locating contact on the soft robot body is a difficult task with current sensors. Another potential application of the sensor is for enhancing rigid-link robots. The sensor could be integrated as both a soft, pliable layer, and a surface/contact sensor for enabling close interaction with the environment. For applications as a wearable device (e.g. rehabilitation), the sensor would closely interact with the body. For complex deformations like in a shoulder joint, the original sensor shape should be customized to the anatomy, which may increase the difficulty in fabrication. Although with our framework, complex, task-specific modelling is not required, care must be taken to minimize the sensor's effect on the wearer (human or robot) and not change their intrinsic deformability.

Regarding cost, fibre-based shape sensors commonly use multiple-core fibre with OFDR-based measurement systems, which are substantially more expensive (>USD160K) and complex to implement, relative to our WDM-based, single-core system (<USD20K).

A number of limitations still exist for the proposed sensor. Firstly, by using a learning-based modelling approach, inherent disadvantages arise relating to data acquisition time and reliance on accurate training data. Additionally, the proposed sensor design has a limited ability to reconstruct very complex shapes due to the rigidity of optical fibre in combination with the small sensor size. In future studies, we will propose an FEA-based optimization scheme to investigate ideal optical fibre layouts for complex deformations or customized shape structures. Finally, we also aim to accelerate the reconstruction speed by exploring other plotting environments and implementation on higher performance hardware.

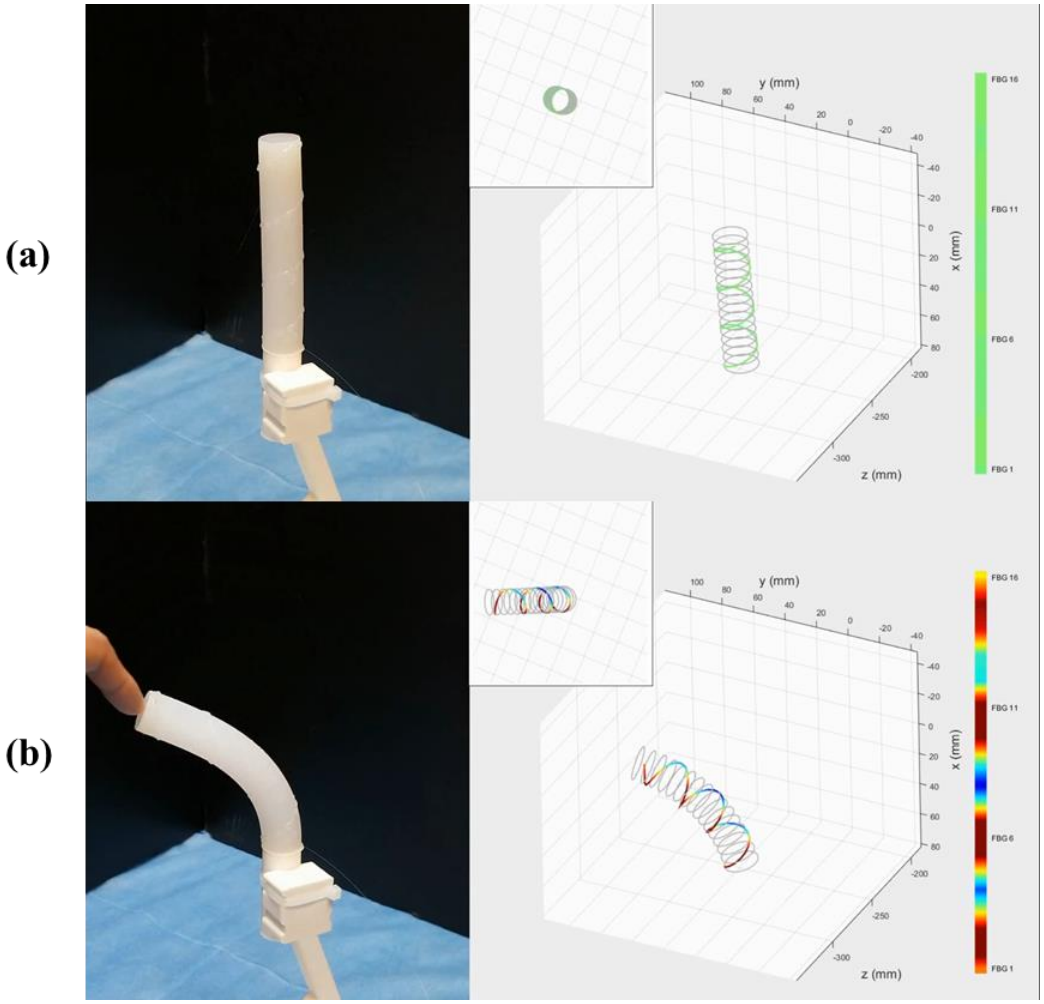

Figure 3.14 Shape sensing of a silicone tube by integrating an optical fibre in a spiral shape along its surface. The fibre was superimposed onto the reconstructed shape to display the strain measured in the FBGs. Warmer colours indicate negative strain (compression) and cooler colours indicate positive strain (tension). **(a)** Sensor at rest. **(b)** Manually deformed sensor.

3.2 MULTIPLE-CORE FIBER FOR 3D SHAPE SENSING

3.2.1 Introduction

Over the past decades, shape sensing has been an area of great interest for researchers and industry. In particular, optical fibre-based shape sensing has gained prominence for its small size, flexibility, and high multiplexing capabilities [76]. Shape sensing with optical fibre can be achieved by a one single-core optical fibre with sparse FBGs, as discussed in **Section 3.1**, however for applications such as medical robotics, a small form-factor is critical. Minimally invasive instruments such as flexible continuum manipulators [88, 89] and biopsy needles [90, 91] have strict requirements for size to minimise unnecessary harm to patients. One approach to achieve this is to combine multiple single-core fibres into a bundle [92, 93] to obtain co-located strain measurements, or by attaching multiple fibres around a flexible material [94, 95], however the longevity of these approaches rely on no creep occurring between the fibres and/or substrate material and no variation in temperature along the material [96]. A more reproducible and reliable approach is the use of fibre that is fabricated with multiple cores [97], which allows an overall smaller diameter and minimises errors introduced when manually combining fibres. The controlled and automated fabrication of this fibre type enforces consistent spacing between gratings and parallel alignment of individual cores. The differential strains measured in each sensor plane can be used to calculate local 3D curvatures and integrated along the fibre length to find the overall 3D shape. In this section, a 7-core fibre with continuous gratings for OFDR interrogation is used. The core orientations for this fibre is fixed during fabrication, however researchers have developed twisted multi-core fibre to enable robust sensing of torsion [98]. Visual comparison between untwisted and twisted core fibre is shown in **Figure 3.15**.

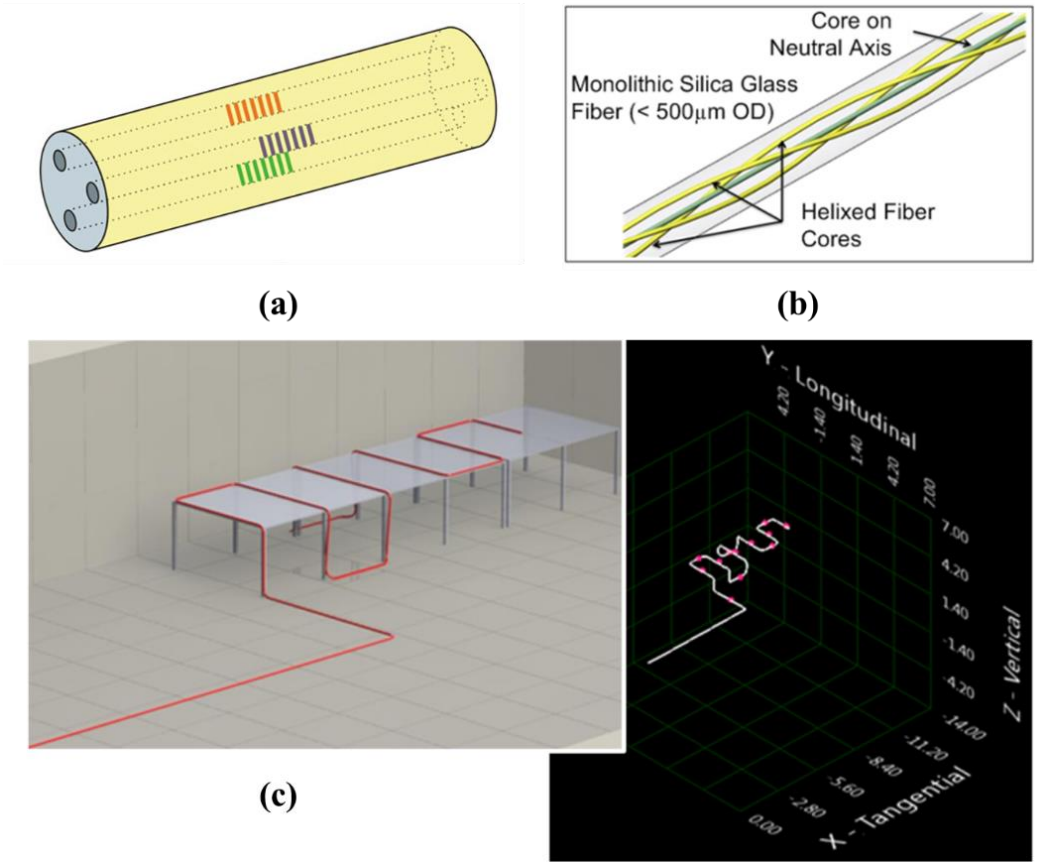

Figure 3.15 **(a)** Illustration of a tri-core optical fibre with untwisted cores [99]. **(b)** Twisted multi-core fibre and **(c)** shape reconstruction example by Luna Innovations [100]**.**

3.2.1.1 Interrogation method

The interrogation system used in **Section 3.1** utilises Wavelength Division Multiplexing, or WDM, to interrogate sparse and discrete FBG measurements [85]. In this approach, each FBG reflects a single centre wavelength of light, and the remaining light is transmitted. The location of the FBGs are defined during the fibre fabrication and multiple FBGs with different centre wavelengths can be written along a single fibre and interrogated by transmitting different laser wavelengths. The hardware used in WDM systems are commonly available, which makes this interrogation method relatively inexpensive and widely adopted. With WDM, very fast sampling speeds can be achieved (>1000 Hz) due to the nature of the interrogation method, however the number of FBGs that can be simultaneously interrogated is limited due to potential overlapping of centre wavelengths at high sensor counts. For the purpose of high resolution shape sensing, Optical Frequency Domain Reflectometry, or OFDR, is a promising alternative [100, 101]. Instead of discrete gratings with different centre wavelengths written along the fibre, continuous gratings are used instead and reflect light at only a single wavelength. A tuneable laser source is continuously swept in the frequency domain to produce backscattered light which is used to determine the local strain and its location. As a result, much higher spatial resolution

sensing can be achieved with OFDR interrogation, although this notably comes at the cost of sampling frequency, system complexity, and development cost. In this work with multi-core fibre, an OFDR interrogation system is used.

3.2.2 Multi-core Fibre and Reconstruction Method

Shape sensing is performed by obtaining off-axis strain from FBGs located in the fibre cross-section. In this study, multi-core fibre (FBGS International) with continuous gratings along the distal 1 m length is used. One core is located at the centre axis of the fibre, and 6 cores are spaced equally about the centre axis at 60° intervals, as shown in **Figure 3.16**. For shape reconstruction, only three cores are required and typically cores spaced equally at 120° are used. Hereafter, the co-located measurement of 3 cores at a position along the fibre will be referred to as a sensor triplet, and the path between two adjacent sets of sensor measurements is referred to as a segment. Two common shape reconstruction approaches for multi-core fibre have been applied by researchers in the past. The first is based on the piecewise constant curvature (PCC) model, which assumes circular bending for each fibre segment, calculating discrete curvature and bending direction measurements for each sensor triplet and summing them to obtain the overall fibre shape [102]. The second method is based on the Frenet-Serret formulas for defining 3D curves, where the effect of torsion (if measurable) can be taken into account [88, 103, 104]. The first method is used in this initial investigation for its relative simplicity.

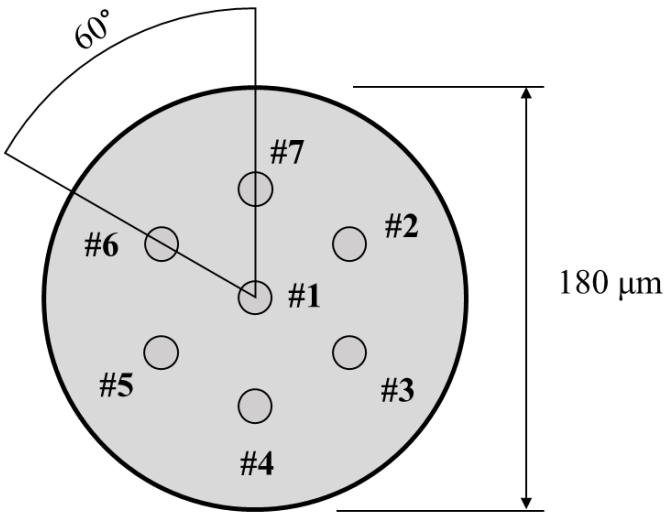

Figure 3.16 Cross-section view of 7-core fibre used in experimentation. The fibre is approximately 180 μm in diameter. Cores 2-7 are equally spaced apart at 60° and are 37 μm from the centre core. Only three off-centre cores are required to perform 3D shape reconstruction.

The principle of the shape reconstruction algorithm is to utilise the differential strain measurements within a sensor triplet to calculate the bending radius, r and bending

direction, α for the corresponding segment. Assuming that the neutral axis length, s remains constant (defined by the spacing between adjacent sensor triplets, i.e. the spatial resolution of the sensor), r and α are used to locate the next sensor triplet. Each sensor triplet's local coordinate system (x', y', z') has origin located at the center of the fiber cross-section with z' pointing towards the distal fibre end, and y' aligned with the first fibre core (arbitrarily designated). The local coordinate system of a sensor triplet is shown in **Figure 3.17(a)** and parameters shown in **Figure 3.17(b)**. When a fibre segment is bent along a curvature, the bending radius of each core is typically different (r_1, r_2, r_3), and have segment lengths differing by $\Delta s_1, \Delta s_2$ and Δs_3 as shown in **Figure 3.18**. In summary, the key formulae derived in [102] for calculating the bending radius, r, and bending direction α of each fiber segment are:

$$\tan(\alpha) = \frac{\epsilon_{13}\sin(\phi_{12}) + \epsilon_{12}\sin(\phi_{13})}{\epsilon_{23} - \epsilon_{13}\cos(\phi_{12}) + \epsilon_{12}\cos(\phi_{13})} \tag{3.6}$$

where $\epsilon_{ij} = \epsilon_j - \epsilon_i$ is the difference in strain between core number i and j, and ϕ_{12}, ϕ_{13} is the angle difference about the center core from core 1 to 2, and core 1 to 3, respectively. The same bending radius can be calculated from the differential strain of any pair of the sensor measurements. In the case that one set of differential strain are zero, another can be used. The calculation using ϵ_{12} is as follows:

$$r = \frac{a}{\epsilon_{12}}(\sigma_1 \sin(\alpha + \phi_{12}) - \sigma_2 \sin(\alpha)) \tag{3.7}$$

where $\sigma_1 = 1 + \epsilon_1$.

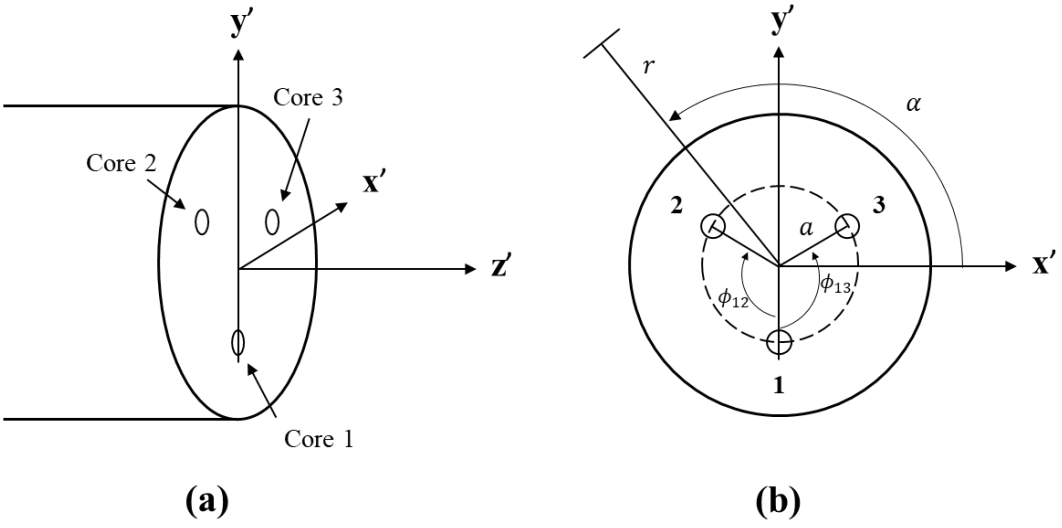

Figure 3.17 **(a)** Coordinate frame definition for a sensor triplet. **(b)** Cross-section schematic of a sensor triplet with labelled fibre cores and parameters.

The bending angle can also be calculated from one of the core strain measurements, with core 1 used below:

$$\theta = s\left(\frac{\sigma_1}{r_1}\right) \tag{3.8}$$

Finally, the coordinates for the end of the segment (and location of the next sensor triplet) relative to the sensor triplet are calculated by:

$$x' = r(1 - \cos(\theta))\cos(\alpha) \tag{3.9}$$

$$y' = r(1 - \cos(\theta))\sin(\alpha) \tag{3.10}$$

$$z' = rsin(\theta) \tag{3.11}$$

The detailed derivation of the shape reconstruction algorithm is explained in [102], along with transformations for locating the sensor frame coordinates in the origin frame.

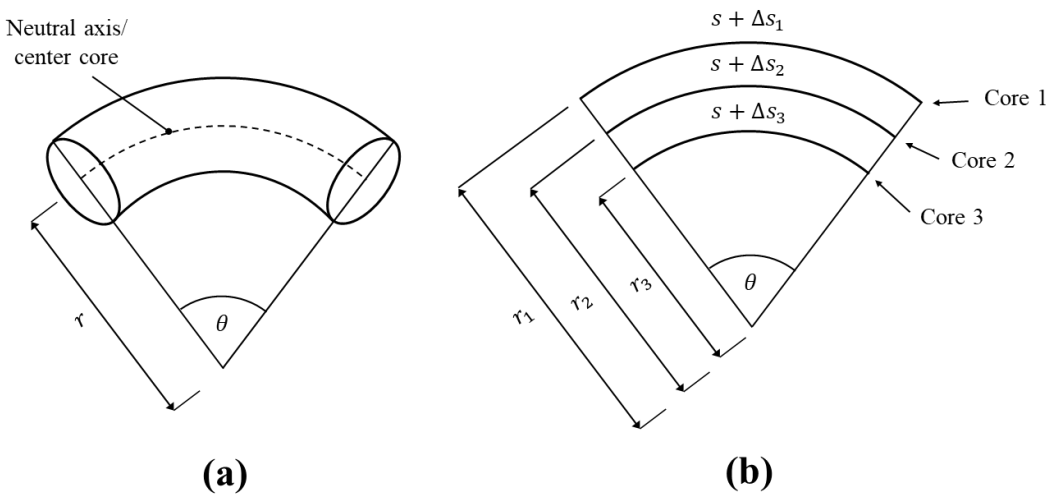

Figure 3.18 **(a)** Illustration indicating bending angle and bending radius for a fibre segment. **(b)** Diagram indicating the change in length of each fibre core for a given bending angle.

3.2.3 Experimental Setup, Results and Discussion

Similar to WDM fibre optic systems, an interrogator is also used to obtain optical signals from the fibre. In this work, an OFDR [75] system is used. Instead of discrete FBGs located along the length of the fibre, OFDR allows continuously distributed gratings along the sensing length of the fibre, in effect allowing a high number of FBGS, with high density spacing. A symmetrical 7-core fibre with approximately 1 m of continuous gratings was used in experimentation. The gratings have centre wavelength 1546 nm and strain measurements were taken at the highest spatial resolution possible, at 6.35 mm spacing

between strain measurements. The fibre is connected to the interrogator setup as in **Figure 3.19**. The multiple channels in the fibre are firstly split into individually-accessible channels through a fan-out box (FBGS International). Patch cords then pass through broadband reflectors (BBRs), which are critical to the demodulation of the FBG locations, followed by connection to the interrogator (RTS125+, Sensuron) which provides the laser source and performs real-time processing of the spectral data.

Prior to experimentation, the optical fibre was calibrated to correct for spatial offsets between each channel's data. The BBRs used to locate the FBGs are very sensitive to their position along the optical connections, which causes this offset. Specifically, slight length discrepancies of the single-core patch cords that connect the fan-out box to the BBRs is the primary source of this. A simple "pinch" test was performed to align each channel's data by inducing high local strain at a point along the sensing region. The number of strain measurements for each sensing length was 48, 32, and 17 for approximating the 300 mm, 200 mm, and 100 mm lengths, respectively. The actual sensing lengths were the number of measurements multiplied by the spacing 6.35 mm, which was 304.8 mm, 203.2 mm, and 107.95 mm, respectively.

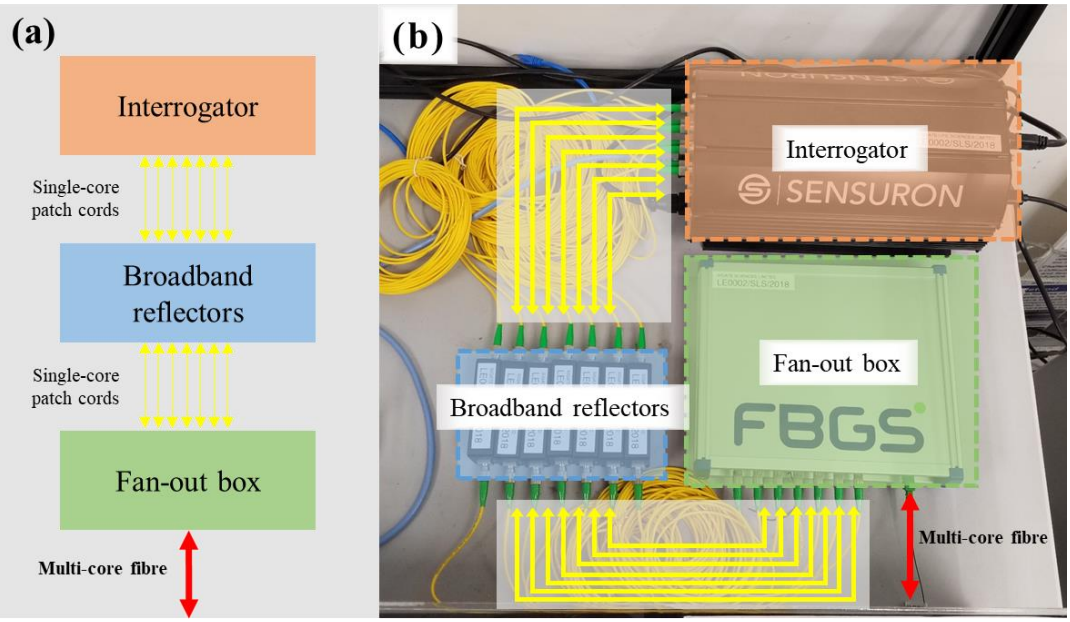

Figure 3.19 Overview of OFDR interrogation setup. **(a)** Schematic diagram. **(b)** Labelled components overlaid on photograph of real setup.

3.2.3.1 Fixed curvature tests

To validate the performance of the shape reconstruction algorithm and fibre setup, three different sensor lengths (using the same fibre), 100 mm, 200 mm and 300 mm were used. The bending curvature of each fibre length was tested by using a range of SLA 3D

printed templates with fixed curvatures. Two templates for 90° and 180° bending were fabricated for each sensing length, totalling 6 templates as seen in **Figure 3.20**. The multi-core fibre used in this work is un-twisted, which means that torsion along the length of the fibre cannot be detected and compensated. Therefore, the free-sleeved approach [103] is used, which aims to retain a constant relationship between the fibre's material frame and the natural curve frame by fixing the fibre at one end and placing it in an ideally frictionless sheath. i.e. to eliminate twisting caused by external forces. Here, Teflon sheaths are used to reduce friction along the sensing length and minimise twisting between sensor planes. A thin Teflon sheath is first used to cover the fibre and closely matches it in diameter, with inner diameter (ID) of 0.3 mm and an outer diameter (OD) of 0.65 mm. In the curvature templates, a larger Teflon sheath is placed along the bending path, with OD = 2 mm, and ID = 0.75 mm.

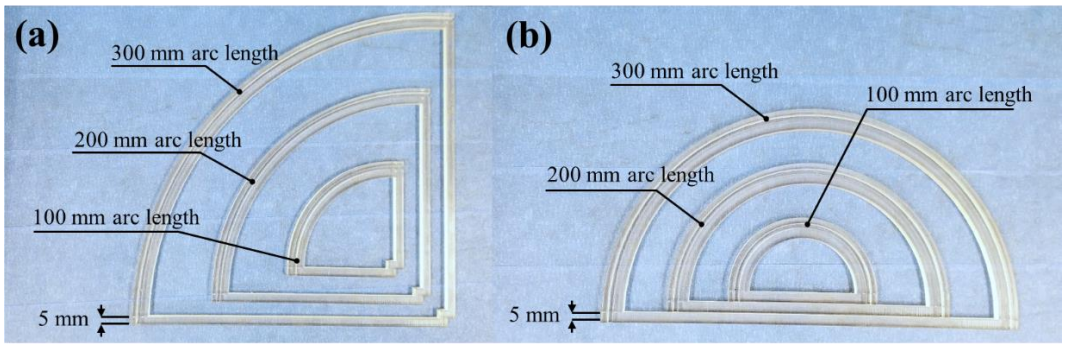

Figure 3.20 3D printed bending curvature templates for sensing lengths 300 mm, 200 mm, and 100 mm. An outer Teflon sheath is fitted along the curvature for the fibre to pass through. A straight 5 mm section is included at the beginning and end of the template. **(a)** 90° bending templates. The corresponding bending radii in descending order are: 191 mm, 127.3 mm and 63.7 mm. **(b)** 180° bending templates. The corresponding bending radii in descending order are: 95.5 mm, 63.7 mm and 31.8 mm.

During the tests, the fibre with thin Teflon sheath was inserted into the curvature template's sheath and 100 consecutive data captures were taken for each template to obtain boxplots for each sensor point. The fibre lengths were measured approximately from the first sensor location at the distal tip to the proximal end. It was noted that the last ~18 mm of the fibre was unusable due to noise, likely caused by back-reflection at the tip. The fibre was fixed at approximately 400 mm from the distal tip to prevent rotation of the base frame.

The reconstructed shapes for the curvature tests (taken at frame 50 of 100 data captures) are plotted in **Figure 3.21**. In these experiments, the fibre coordinate frame was not registered/aligned to the laboratory coordinates and the first sensor triplet coordinate frame is taken as the origin (0, 0, 0).

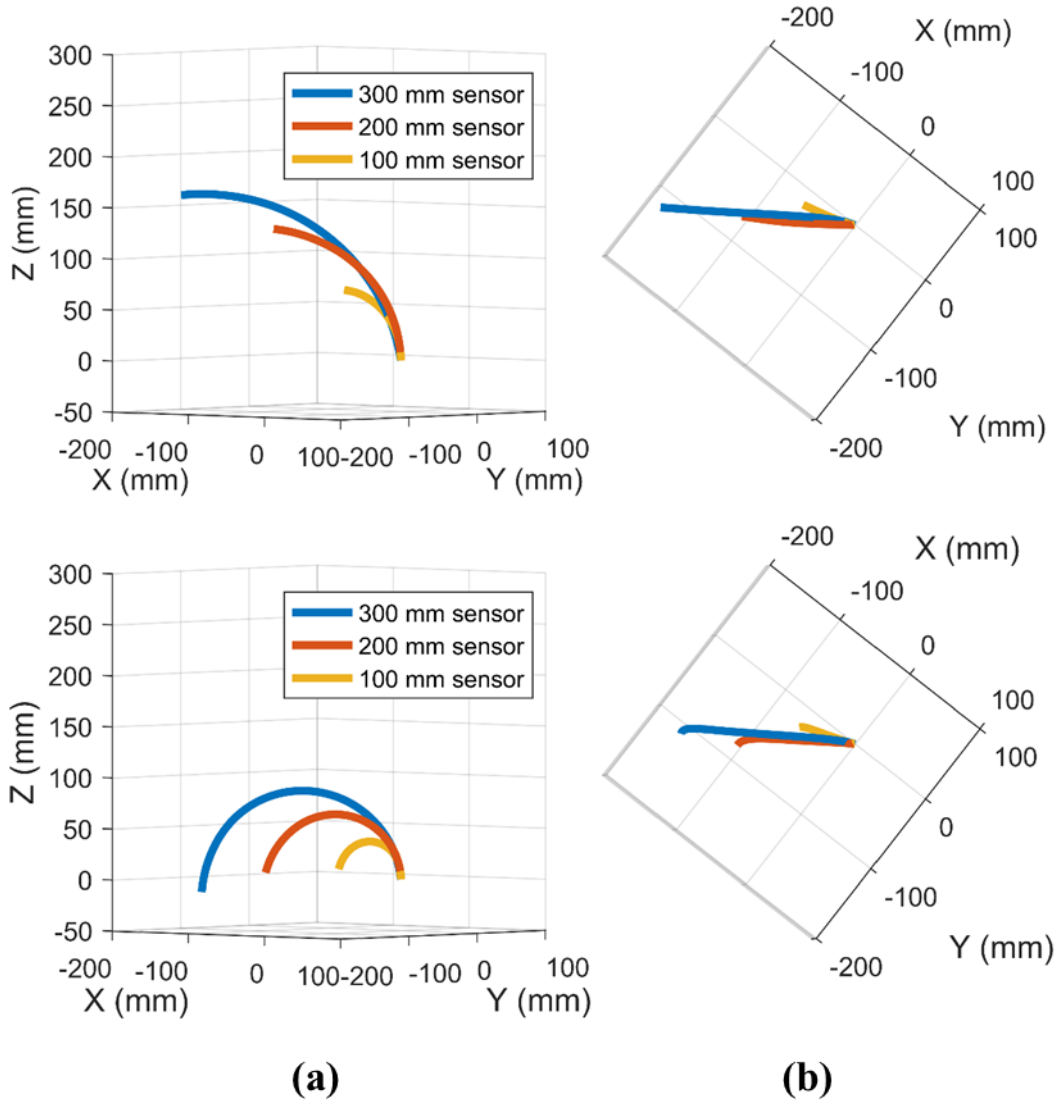

Figure 3.21 Example 3D shape reconstruction for each bending curvature test. The 50th frame of 100 data captures was used for plotting. **(a)** Front view for 90° (top) and 180° (bottom) bending for each sensor length. **(b)** Top view for 90° (top) and 180° (bottom) bending for each sensor length.

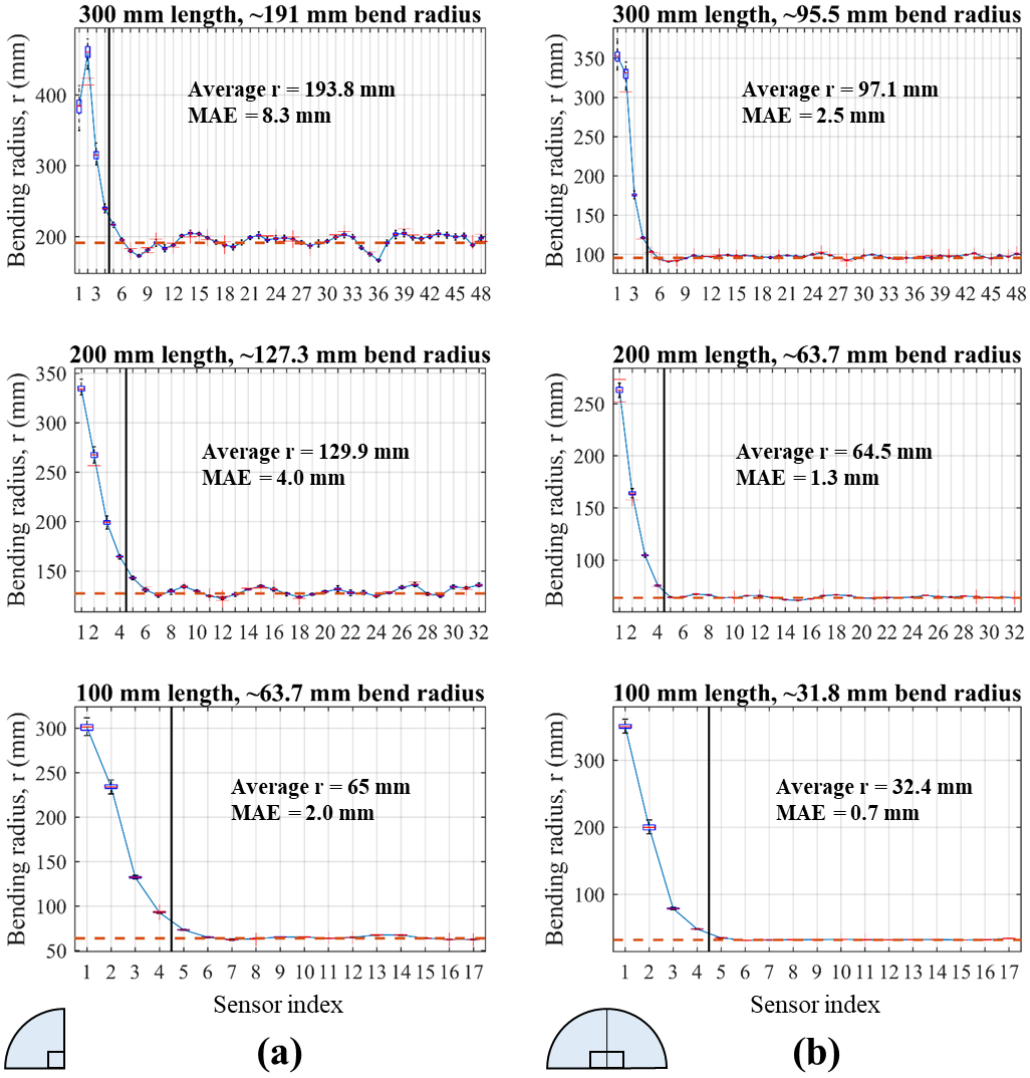

Figure 3.22 Bending radius versus sensor index for 300 mm, 200 mm, and 100 mm sensing lengths. Sensor index 1 is nearest to the fibre connector, with subsequent sensors located 6.25 mm further along the fibre towards the fibre tip. Boxplots are shown for each sensor index for data captured over 100 samples. The average bending radii and mean absolute error (MAE) is indicated in each graph. **(a)** 90° bending for each sensor length. **(b)** 180° bending for each sensor length.

The measured bending radius versus sensor index is shown in **Figure 3.22**. The sensor index starts from the proximal end of the fibre, where index 1 is nearest to the fibre connector, and the largest sensor index of each figure is located at the distal end of the fibre. The plotted points correspond to the mean bending radii taken over 100 data captures. Boxplots indicate the distribution of data for each sensor, with the central mark indicating the median, top and bottom edges of the box indicating the 75th and 25th percentiles, respectively, and whiskers extending to ± 2.7 standard deviations. Outliers are indicated with red crosses. The first four sensor measurements in each plot overall showed much higher bending radii than the remaining points and could be explained by looseness

between the fibre and Teflon sheaths, resulting in some deviation between the template curvature and the actual bending shape of the fibre. At the initial entrance to the template, the fibre gradually matches the bending curvature rather than immediately, due to this looseness. The first sensor locations may also have been slightly offset from the entrance of the template, further exacerbating the gradual transition to the true bending curvature. The overall average error between the template curvature and measured curvature was 1.62 mm, excluding the first 4 sensor measurements. The sensors over-estimated the bending radius for all the tests (i.e. the sensor measured less bending than the actual template). Possible reasons for this include incomplete calibration when aligning the channel data or the strain gauge factor is lower than the true value. Although the mean error was relatively low, the mean absolute error (MAE) showed higher fluctuation for the 90° bending tests versus the 180° bending test of the same sensing length. An apparent positive correlation was also seen between the measured bending radius error and total sensing length.

3.2.3.2 Bending direction tests

During the first set of curvature tests, the bending direction for each sensor triplet, α, was also recorded and plotted against the sensor index for 90° and 180° bending in **Figure 3.23** and **Figure 3.24**, respectively. A second set of data for the bending direction was also taken *without* an inner Teflon sheath (**Figure 3.25** and **Figure 3.26**). The experiments allow comparison of the torsional effect of a looser or tighter sleeve. In both results, the bending direction was seen to decrease along the length of the sensor, however, significantly larger fluctuation was seen with the inner sheath when compared to without the inner sheath. This is most likely due to the torsional loading applied by the sheaths as a result of friction. The thinner, inner sheath leaves less clearance between the fibre and the sheath which can result in more "choke-points" of friction as indicated by the fluctuation of bending directions in 300 mm and 200 mm tests. Comparatively, the increased clearance when using only the outer Teflon sheath demonstrated a smoother decrease in bending direction, with the exception of one point along the sensor, which appeared to be noise, as suggested by the high spread of the boxplots. The general trend of decreasing bending direction was seen over the length of the fibre, with almost linear trends seen in the experiments with no inner sheath, and the 100 mm length results for the inner sheath experiments. This may suggest a systematic error in the reconstruction algorithm, such as incorrect core data alignment during calibration. The deviation from a single bending plane can be observed in **Figure 3.21** for the results with an inner sheath.

Several more complex shapes were also qualitatively investigated as shown in **Figure 3.27**. All of the shapes were laid on a planar surface while attempting to minimise

twisting. An outer Teflon sheath (OD = 2 mm, and ID = 0.75 mm) was used. The outer sheath and fibre were fixed relative to each other at approximately 300 mm from the distal sensor triplet. The algorithm could reconstruct shapes that resemble the true fibre deformation, however, significant deviation from the bending plane is also observed in each example, visible in the far-right column of **Figure 3.27** (top-down view). In the ideal reconstruction cases for these examples, the fibre bending plane should be perpendicular to the top-down view, appearing as a single line. Error analysis was not performed for these shapes because the deviation from the correct shape is qualitatively, very large. Error analysis will be performed in future work, alongside improved shape reconstruction. The results support the hypothesis that when using the free-sleeved approach, the sheath design must be carefully considered to minimise any torsional effect on the fibre.

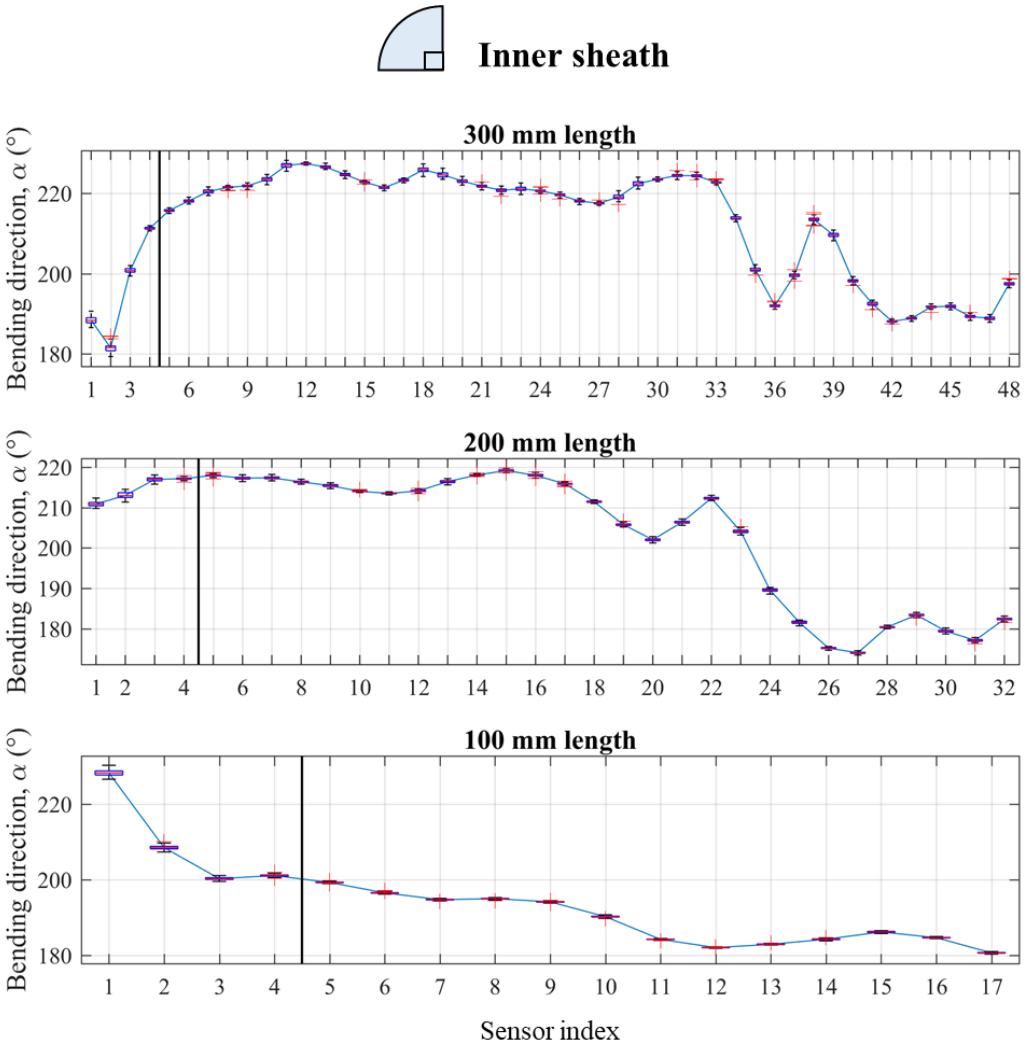

Figure 3.23 Bending direction results for 90° bending with the inner Teflon sheath for three sensing lengths. Boxplots for each sensor show the data distribution over 100 data captures.

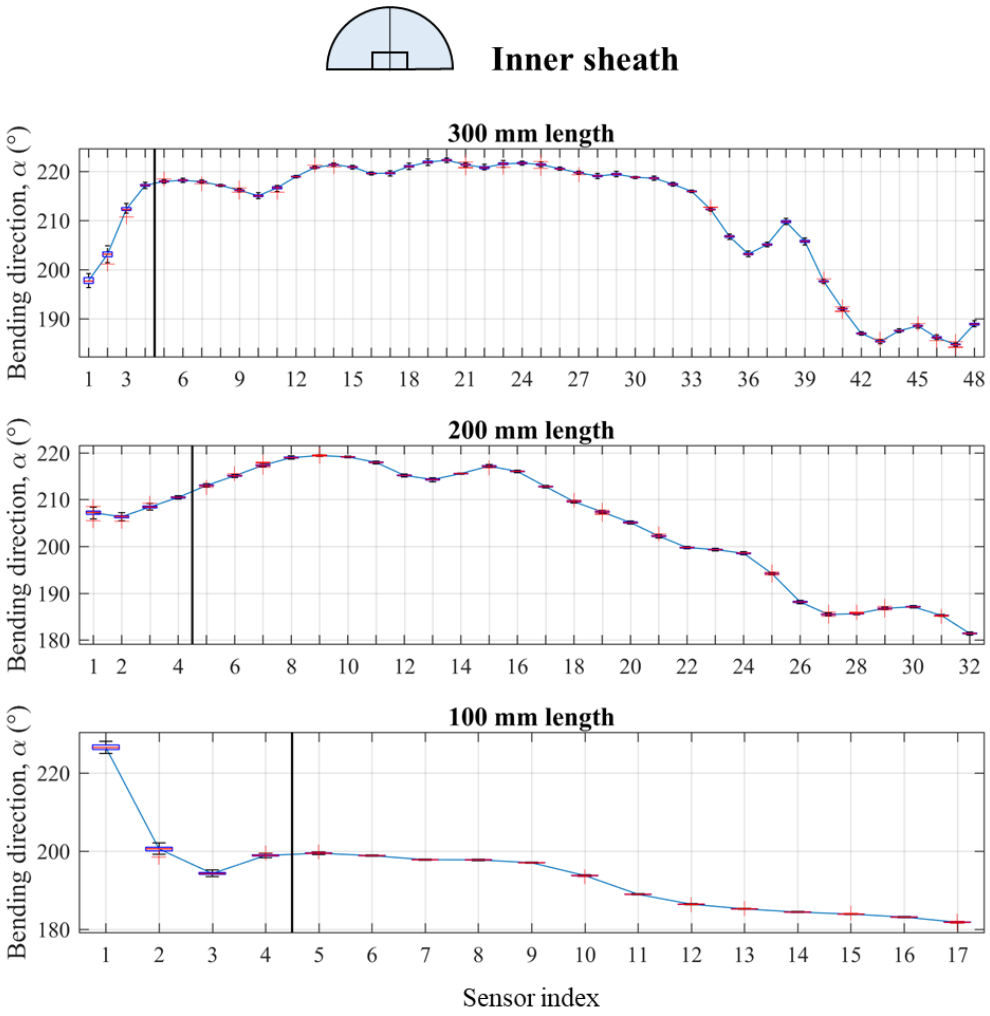

Figure 3.24 Bending direction results for 180° bending with the inner Teflon sheath for three sensing lengths. Boxplots for each sensor show the data distribution over 100 data captures.

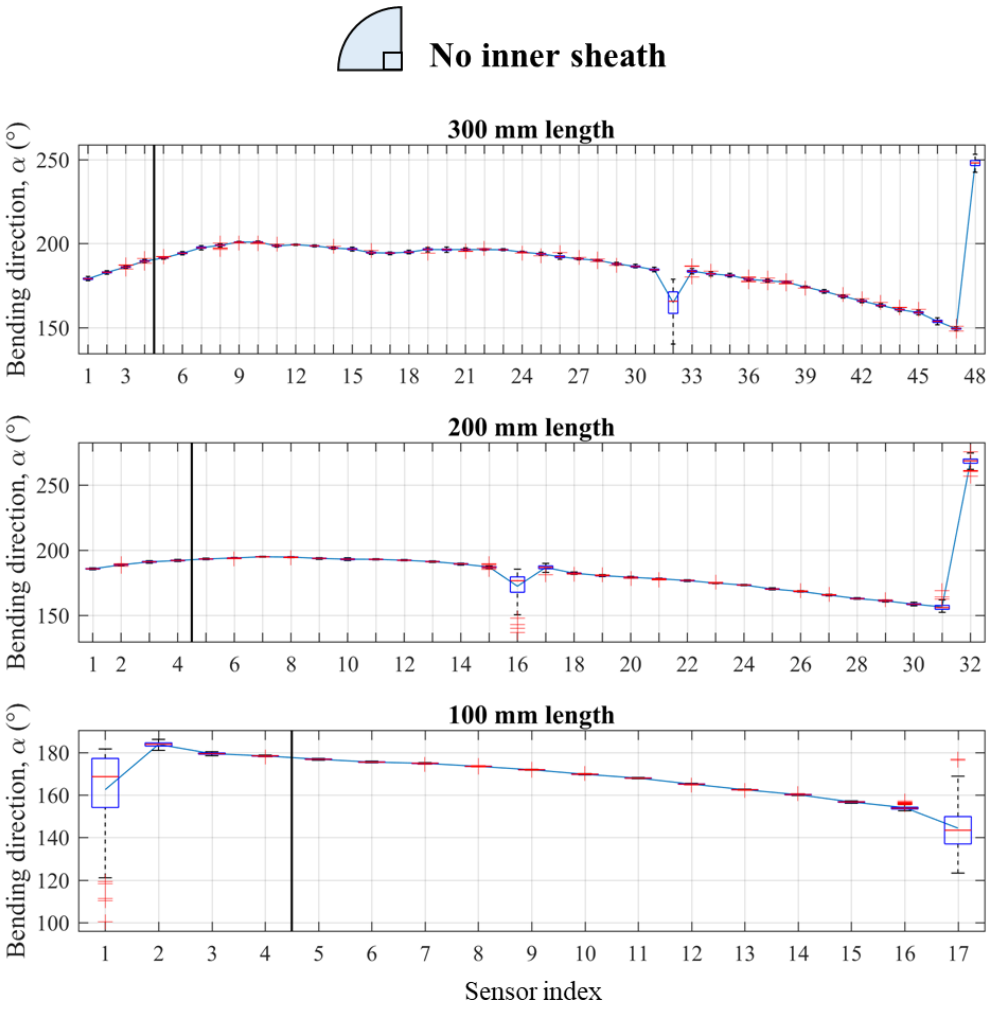

Figure 3.25 Bending direction results for 90° bending with no inner Teflon sheath for three sensing lengths. Boxplots for each sensor show the data distribution over 100 data captures.

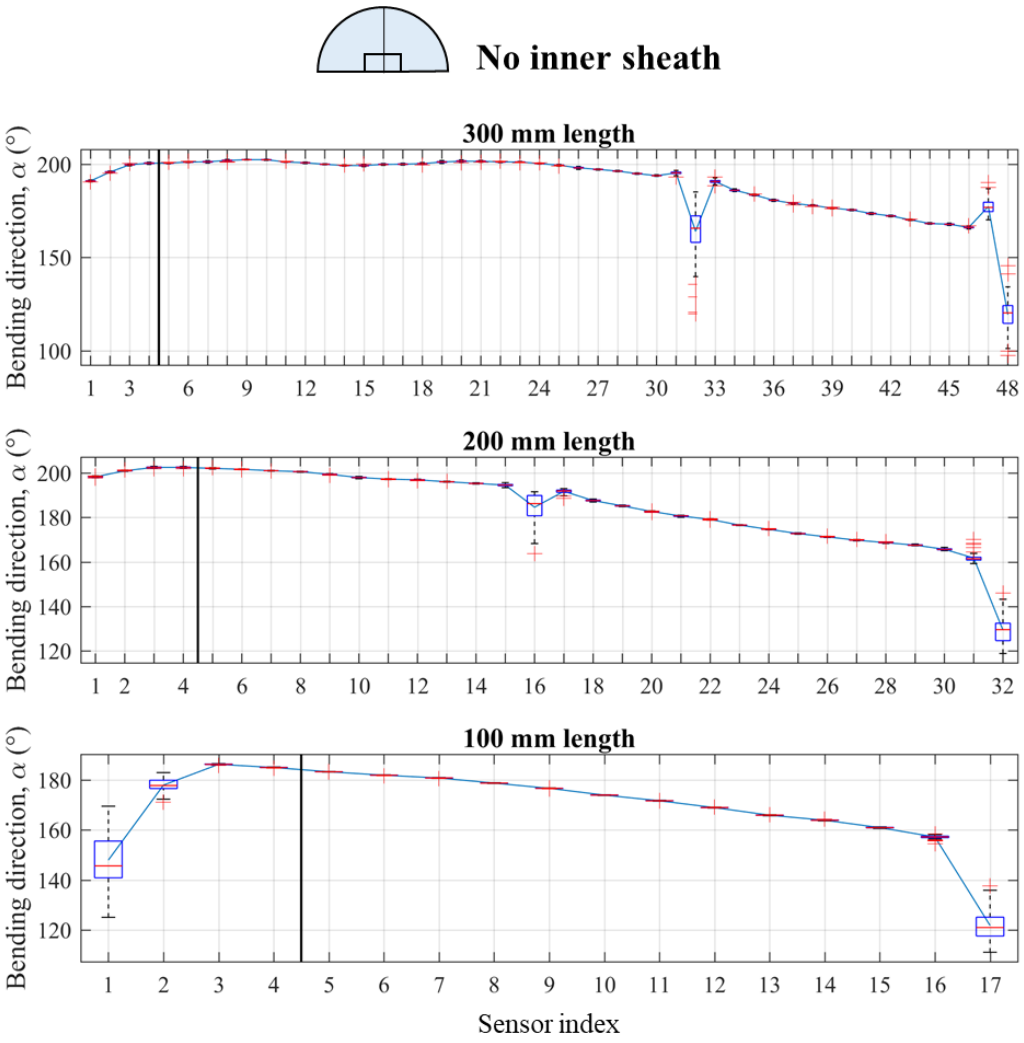

Figure 3.26 Bending direction results for 180° bending with no inner Teflon sheath for three sensing lengths. Boxplots for each sensor show the data distribution over 100 data captures.

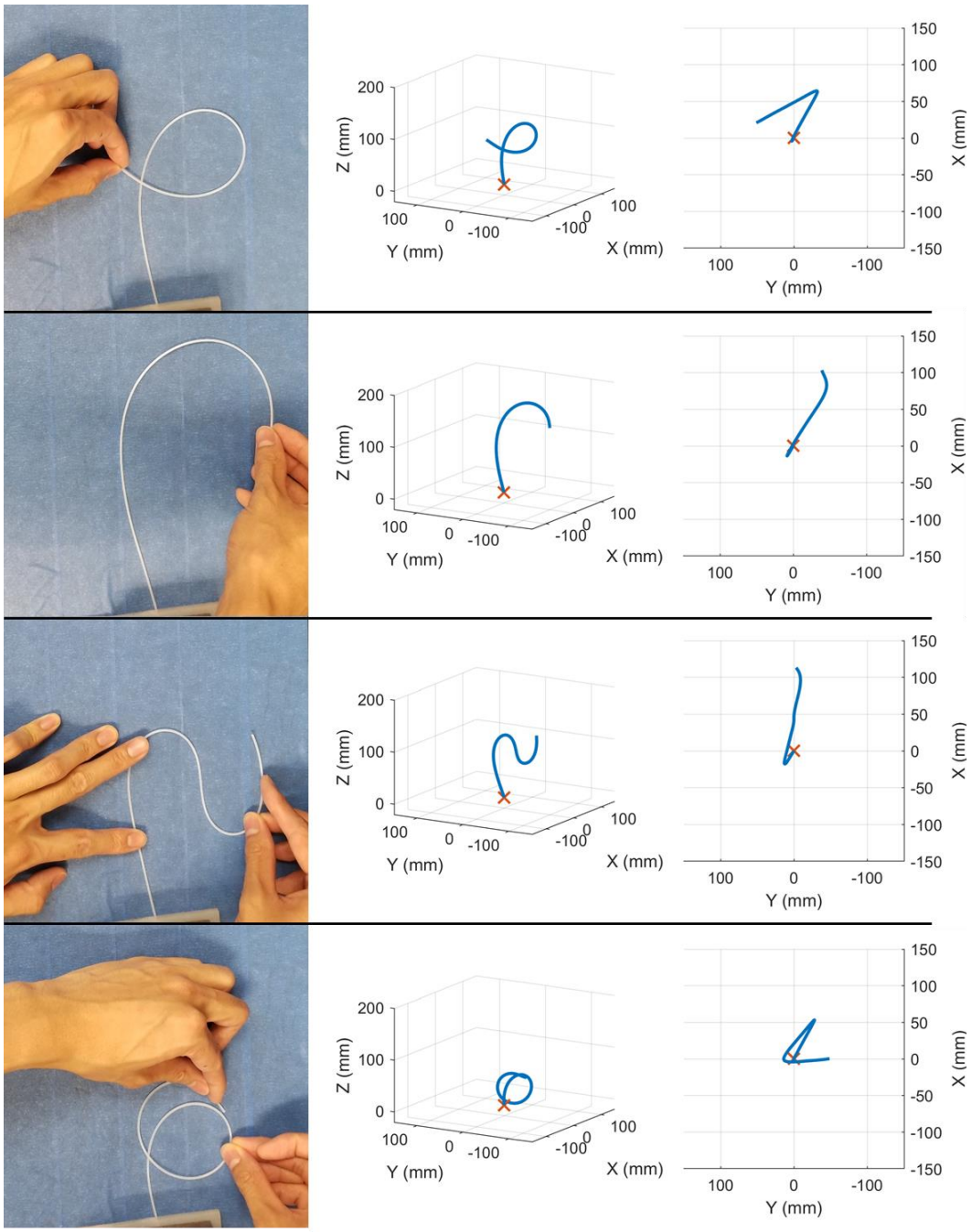

Figure 3.27 Shape reconstruction plots for various sensor shapes with outer Teflon sheath. The sensing length used is 300 mm. The **left** column is the photographed shapes of the manually deformed fibre. The **middle** and **right** columns are the corresponding reconstructed shapes from a diagonal and top-down view, respectively.

3.2.3.3 Limitations

In its presented state, the shape sensor is able to generally reconstruct the fibre shape, albeit with significant deviation in bending direction. The primary limitations of the current shape sensor include the fibre design/layout, reconstruction algorithm, calibration method, and sheath design. An inherent limitation of using un-twisted multi-core fibre is

the lack of sensitivity to twisting. To minimise the effect of twisting on the current shape sensor, the sensor length that is used can be shortened to improve overall accuracy. Additionally, an ideal outer sleeve should impart zero frictional forces to the fibre, which allows the fibre to remain untwisted along a certain length. Alternatively, a twisted-core fibre design can be adopted, which has uniform twisting along the fibre length introduced during fabrication.

Back-reflection caused by the interface between the tip of the fibre and air also renders a short length of the sensor tip unusable for taking measurements. This limits the fibre's uses in certain applications such as measuring the bending section of flexible surgical instruments, as the pose of the instrument tip is often most needed. The noise can in theory be mitigated by methods that interrupt the sensor-tip interface, with examples such as low-levels of abrasion applied to the tip or an index-matching gel which aims to approximate the refractive index of the fibre.

For more complex shapes with multiple tight turns, under-sampling of strain may also induce errors. Currently, the strain measurements are taken at 6.35 mm intervals and the shape reconstruction algorithm assumes a constant bending curvature over a segment, which is typically not the case. Researchers have demonstrated that with much higher spatial resolution the overall shape sensing accuracy would be improved [105]. Furthermore, the PCC-based approach is only a simple reconstruction algorithm that serves as an entry-point to more robust and complex shape reconstruction methods.

3.2.4 Conclusions and Future Work

Preliminary studies into shape sensing with multi-core FBG optical fibre is presented in this work. Optical fibre-based sensing provides numerous benefits such as small form-factor and high multiplexing ability making it an attractive choice for applications in the aerospace industry, civil engineering, and the medical robotics industry. Although FBG-based sensing as a whole is widely available, interrogators that can read high density measurements from continuous grating fibre is only developed by a few companies due to the know-how and technical complexity required for OFDR interrogation.

Preliminary studies into the shape reconstruction of a multi-core continuous grating fibre is demonstrated in this work. The shape reconstruction algorithm makes use of the differential strains measured in sensor triplets to calculate the bending radius, bending direction, and the resulting relative displacement of each sensor. By taking the sum of these values along the length of the fibre, the overall shape of the fibre can be found. 3D printed templates with fixed curvature were used for testing the bending radius and

direction. The average bending radius error recorded was 1.62 mm, with an average MAE of 3.13 mm. Two bending direction tests were performed, the first which used an inner Teflon sheath in addition to the outer Teflon sheath on the curvature templates, and the second set of tests which only used the outer Teflon sheath. The results indicated larger fluctuation of bending direction along the length of the fibre, likely due to the higher friction between the fibre and inner Teflon sheath.

In future work, the aim will be to incorporate the shape sensing fibre into medical robotic applications. The fibre could be integrated into miniature soft robotic systems for surgery, for example MRI-guided transoral laser surgery, where the sensing systems should have minimal impact on the robot mechanical performance and should be easy to implement. We also aim to measure the 3D bending shape of a flexible catheter tip during cardiac ablation for feedback control of an MRI-compatible cardiac catheter robot [106]. The thin diameter would allow less-intrusive integration with the existing catheter systems and provide high spatial resolution information of its shape which can be used to assist surgeons or for autonomous feedback control. The sensing length of the fibre can also be shortened to only measure the active bending portion of the catheter and improve reconstruction accuracy. MRI-based tracking markers can provide the reference point of the shape sensing and facilitate registration with the MRI coordinate frame. However, prior to integration with any system, the reconstruction accuracy of the standalone fibre must be improved by further investigation into the reconstruction algorithm, calibration methods, and sheath design. Researchers have demonstrated alternative shape reconstruction algorithms that could have improved accuracy over the implemented PCC-based approach. Kim *et al.* [107] compares the shape reconstruction accuracy between three different approaches: PCC, PCA, and polynomial regression. They also aimed to optimise the sensor locations to minimize reconstruction error when applied to their concentric tube robot. The polynomial regression and PCA-based methods outperformed PCC by a large margin, which could guide our reconstruction algorithm development in the future. The Frenet-Serret equations [103, 108, 109] also have potential as the formulation implicitly includes parameters for twist, which could aid in calibration and overall reconstruction accuracy. Therefore, further investigation into reconstruction methods will be done, alongside more in-depth evaluation of the overall reconstruction accuracy.

CHAPTER 4
CONCLUSION

4.1 OVERALL CONCLUSIONS AND FUTURE WORK

In this thesis, two main areas of soft robotic systems were investigated: control and sensing. Soft and hyper-elastic structures are inherently flexible, deformable, and can safely and passively interact with their environment. However, these same properties make them difficult to model and control accurately particularly when interacting with the environment. In **Chapter 2**, we aimed to fully utilise these features of soft robots such that accurate control could be maintained. A learning-based modelling approach was used to control a redundant two-segment soft robot while under the effects of unmodelled external disturbances. To handle the redundancy of the manipulator, a constrained optimization problem was formulated where incoming training data were given costs based on the desired null-space behaviour. Experiments were performed to validate the effect of online updates on trajectory tracking accuracy, including scenarios without any disturbance to the robot, added static tip load, and an increasing fluid load at the robot tip. In general, the robot's tracking performance improved in all cases, with instability avoided in the fluid load test due to the online learning updates. In this work, feedback of the robot's posture was done using a simple EM sensor measuring the position of the robot tip, however, in practice the robot's body may be undergoing complex deformations that are not taken into account in the control scheme. This is a common trend seen in the validation of soft robotic

control due to its convenience and accuracy, but the ability to know the shape of the robot body (as in typical rigid-link robots) opens opportunities for more dextrous and precise manipulation. For the purpose of closed-loop control in environments where external sensing equipment is not practical, such as an operating theatre or underwater, the use of standalone/self-contained sensing is required.

A soft sensor design framework was presented in **Chapter 3**, with the aim to provide a general method for designing and fabricating soft sensors for multi-purpose applications, including soft robotic control. A flat prototype surface shape sensor was designed, fabricated, and validated in this work. FBGs were used for their numerous benefits: customizability, flexibility, small form factor, and high multiplexing ability, with the additional benefit of electromagnetic immunity. In the presented sensor design framework, the implementation of machine learning-based modelling is a key that allows reconstruction of the surface shape without explicit knowledge of the underlying sensor locations. By leveraging a data-driven approach, it can adapt to manual fabrication errors, and unpredictable interactions between the fibre, adhesive, and substrate material.

Preliminary investigation into shape sensing with multi-core fibre was also presented. Fixed-curvature templates were used in the evaluation of curvature and bending direction measurements. Multi-core fibre is a sensor modality that provides high density strain measurements in a small form factor. This makes it a promising choice for applications where size is a critical factor, such as in minimally invasive surgery.

On the basis of this work, a number of future research directions could be taken that would involve the integration of FBG-based sensing in combination with soft robotic and flexible systems. Examples include the sensing fusion between FBG-based shape sensing with visual servo-based control of a soft robot [46]. This approach has potential to improve the compensation of external disturbances while also determining its location for improved motion planning. Methods for integrating multi-core optical fibre into flexible systems will also be of interest, in particular towards shape sensing of clinical cardiac catheters and other minimally invasive instruments with steerable end effectors. Quantitative comparison between different integration approaches and reconstruction algorithms will also be performed.

REFERENCES

[1] W. M. Kier and K. K. Smith, "Tongues, tentacles and trunks: the biomechanics of movement in muscular-hydrostats," *Zoological journal of the Linnean Society*, vol. 83, no. 4, pp. 307-324, 1985.

[2] C. Laschi, B. Mazzolai, and M. Cianchetti, "Soft robotics: Technologies and systems pushing the boundaries of robot abilities," *Science Robotics*, vol. 1, no. 1, 2016.

[3] D. Rus and M. T. Tolley, "Design, fabrication and control of soft robots," *Nature*, vol. 521, p. 467, 05/27/online 2015.

[4] D. Trivedi, C. D. Rahn, W. M. Kier, and I. D. Walker, "Soft robotics: Biological inspiration, state of the art, and future research," *Applied bionics and biomechanics*, vol. 5, no. 3, pp. 99-117, 2008.

[5] S. Kim, C. Laschi, and B. Trimmer, "Soft robotics: a bioinspired evolution in robotics," *Trends in biotechnology*, vol. 31, no. 5, pp. 287-294, 2013.

[6] J. Wilson, D. Li, Z. Chen, and R. George, "Flexible robot manipulators and grippers: Relatives of elephant trunks and squid tentacles," in *Robots and Biological Systems: Towards a New Bionics?*: Springer, 1993, pp. 475-494.

[7] C. Laschi, M. Cianchetti, B. Mazzolai, L. Margheri, M. Follador, and P. Dario, "Soft Robot Arm Inspired by the Octopus," *Advanced Robotics*, vol. 26, no. 7, pp. 709-727, 2012.

[8] W. McMahan, V. Chitrakaran, M. Csencsits, D. Dawson, I. D. Walker, B. A. Jones, M. Pritts, D. Dienno, M. Grissom, and C. D. Rahn, "Field trials and testing of the OctArm continuum manipulator," in *Proceedings 2006 IEEE International Conference on Robotics and Automation, 2006. ICRA 2006.*, 2006, pp. 2336-2341: IEEE.

[9] E. Tumino, "Endotics system vs colonoscopy for the detection of polyps," *World Journal of Gastroenterology*, vol. 16, no. 43, 2010.

[10] B. Vucelic, D. Rex, R. Pulanic, J. Pfefer, I. Hrstic, B. Levin, Z. Halpern, and N. Arber, "The aer-o-scope: proof of concept of a pneumatic, skill-independent, self-propelling, self-navigating colonoscope," *Gastroenterology*, vol. 130, no. 3, pp. 672-7, Mar 2006.

[11] F. Cosentino, E. Tumino, G. R. Passoni, E. Morandi, and A. Capria, "Functional

evaluation of the endotics system, a new disposable self-propelled robotic colonoscope: in vitro tests and clinical trial," *The International journal of artificial organs*, vol. 32, no. 8, pp. 517-527, 2009.

[12] M. Cianchetti, T. Ranzani, G. Gerboni, T. Nanayakkara, K. Althoefer, P. Dasgupta, and A. Menciassi, "Soft Robotics Technologies to Address Shortcomings in Today's Minimally Invasive Surgery: The STIFF-FLOP Approach," *Soft Robotics*, vol. 1, no. 2, pp. 122-131, 2014.

[13] K. C. Galloway, K. P. Becker, B. Phillips, J. Kirby, S. Licht, D. Tchernov, R. J. Wood, and D. F. Gruber, "Soft robotic grippers for biological sampling on deep reefs," *Soft robotics*, vol. 3, no. 1, pp. 23-33, 2016.

[14] A. D. Marchese, C. D. Onal, and D. Rus, "Autonomous soft robotic fish capable of escape maneuvers using fluidic elastomer actuators," *Soft Robotics*, vol. 1, no. 1, pp. 75-87, 2014.

[15] M. T. Tolley, R. F. Shepherd, B. Mosadegh, K. C. Galloway, M. Wehner, M. Karpelson, R. J. Wood, and G. M. Whitesides, "A resilient, untethered soft robot," *Soft Robotics*, vol. 1, no. 3, pp. 213-223, 2014.

[16] R. J. Webster and B. A. Jones, "Design and Kinematic Modeling of Constant Curvature Continuum Robots: A Review," *The International Journal of Robotics Research*, vol. 29, no. 13, pp. 1661-1683, 2010.

[17] I. D. Walker, "Continuous Backbone “Continuum” Robot Manipulators," *ISRN Robotics*, vol. 2013, pp. 1-19, 2013.

[18] T. George Thuruthel, Y. Ansari, E. Falotico, and C. Laschi, "Control Strategies for Soft Robotic Manipulators: A Survey," *Soft robotics*, 2018.

[19] H. Wang, C. Wang, W. Chen, X. Liang, and Y. Liu, "Three-dimensional dynamics for cable-driven soft manipulator," *IEEE/ASME Transactions on Mechatronics*, vol. 22, no. 1, pp. 18-28, 2017.

[20] P. Qi, C. Liu, A. Ataka, H. K. Lam, and K. Althoefer, "Kinematic Control of Continuum Manipulators Using a Fuzzy-Model-Based Approach," *IEEE Transactions on Industrial Electronics*, vol. 63, no. 8, pp. 5022-5035, 2016.

[21] B. A. Jones and I. D. Walker, "Kinematics for multisection continuum robots," *IEEE Transactions on Robotics*, vol. 22, no. 1, pp. 43-55, 2006.

[22] D. B. Camarillo, C. F. Milne, C. R. Carlson, M. R. Zinn, and J. K. Salisbury, "Mechanics Modeling of Tendon-Driven Continuum Manipulators," *IEEE*

Transactions on Robotics, vol. 24, no. 6, pp. 1262-1273, 2008.

[23] R. J. Webster, J. P. Swensen, J. M. Romano, and N. J. Cowan, "Closed-form differential kinematics for concentric-tube continuum robots with application to visual servoing," in *Experimental Robotics*, 2009, pp. 485-494: Springer.

[24] S. Neppalli, M. A. Csencsits, B. A. Jones, and I. D. Walker, "Closed-form inverse kinematics for continuum manipulators," *Advanced Robotics,* vol. 23, no. 15, pp. 2077-2091, 2009.

[25] D. Trivedi, A. Lotfi, and C. D. Rahn, "Geometrically exact dynamic models for soft robotic manipulators," in *Intelligent Robots and Systems, 2007. IROS 2007. IEEE/RSJ International Conference on*, 2007, pp. 1497-1502: IEEE.

[26] F. Renda, M. Giorelli, M. Calisti, M. Cianchetti, and C. Laschi, "Dynamic model of a multibending soft robot arm driven by cables," *IEEE Transactions on Robotics,* vol. 30, no. 5, pp. 1109-1122, 2014.

[27] M. Rolf, J. J. Steil, and M. Gienger, "Goal babbling permits direct learning of inverse kinematics," *IEEE Transactions on Autonomous Mental Development,* vol. 2, no. 3, pp. 216-229, 2010.

[28] A. T. Hasan, A. M. S. Hamouda, N. Ismail, and H. Al-Assadi, "An adaptive-learning algorithm to solve the inverse kinematics problem of a 6 DOF serial robot manipulator," *Advances in Engineering Software,* vol. 37, no. 7, pp. 432-438, 2006.

[29] R. Köker, C. Öz, T. Çakar, and H. Ekiz, "A study of neural network based inverse kinematics solution for a three-joint robot," *Robotics and autonomous systems*, vol. 49, no. 3-4, pp. 227-234, 2004.

[30] J. Peters and S. Schaal, "Learning to Control in Operational Space," *The International Journal of Robotics Research,* vol. 27, no. 2, pp. 197-212, 2008.

[31] D. Nguyen-Tuong and J. Peters, "Model learning for robot control: a survey," *Cogn Process,* vol. 12, no. 4, pp. 319-40, Nov 2011.

[32] M. Giorelli, F. Renda, M. Calisti, A. Arienti, G. Ferri, and C. Laschi, "Neural network and jacobian method for solving the inverse statics of a cable-driven soft arm with nonconstant curvature," *IEEE Transactions on Robotics,* vol. 31, no. 4, pp. 823-834, 2015.

[33] A. Melingui, O. Lakhal, B. Daachi, J. B. Mbede, and R. Merzouki, "Adaptive neural network control of a compact bionic handling arm," *IEEE/ASME Transactions on Mechatronics*, vol. 20, no. 6, pp. 2862-2875, 2015.

[34] O. Lakhal, A. Melingui, and R. Merzouki, "Hybrid approach for modeling and solving of kinematics of a compact bionic handling assistant manipulator," *IEEE/ASME Transactions on Mechatronics,* vol. 21, no. 3, pp. 1326-1335, 2016.

[35] T. Thuruthel, E. Falotico, M. Cianchetti, F. Renda, and C. Laschi, "Learning global inverse statics solution for a redundant soft robot," in *Proceedings of the 13th International Conference on Informatics in Control, Automation and Robotics,* 2016, vol. 2, pp. 303-310.

[36] D. Braganza, D. M. Dawson, I. D. Walker, and N. Nath, "A neural network controller for continuum robots," *IEEE transactions on robotics,* vol. 23, no. 6, pp. 1270-1277, 2007.

[37] K. H. Lee, D. K. C. Fu, M. C. W. Leong, M. Chow, H. C. Fu, K. Althoefer, K. Y. Sze, C. K. Yeung, and K. W. Kwok, "Nonparametric Online Learning Control for Soft Continuum Robot: An Enabling Technique for Effective Endoscopic Navigation," *Soft Robotics,* vol. 4, no. 4, pp. 324-337, Dec 2017.

[38] A. D'Souza, S. Vijayakumar, and S. Schaal, "Learning inverse kinematics," in *Intelligent Robots and Systems, 2001. Proceedings. 2001 IEEE/RSJ International Conference on,* 2001, vol. 1, pp. 298-303: IEEE.

[39] K.-H. Lee, M. C. Leong, M. C. Chow, H.-C. Fu, W. Luk, K.-Y. Sze, C.-K. Yeung, and K.-W. Kwok, "FEM-based soft robotic control framework for intracavitary navigation," in *Real-time Computing and Robotics (RCAR), 2017 IEEE International Conference on,* 2017, pp. 11-16: IEEE.

[40] S. Vijayakumar, A. D'souza, and S. Schaal, "Incremental online learning in high dimensions," *Neural computation,* vol. 17, no. 12, pp. 2602-2634, 2005.

[41] S. Klanke, S. Vijayakumar, and S. Schaal, "A library for locally weighted projection regression," *Journal of Machine Learning Research,* vol. 9, no. Apr, pp. 623-626, 2008.

[42] D. E. Whitney, "Resolved motion rate control of manipulators and human prostheses," *IEEE Transactions on Man-machine Systems,* vol. 10, no. 2, pp. 47-53, 1969.

[43] B. Espiau, F. Chaumette, and P. Rives, "A new approach to visual servoing in robotics," *IEEE Transactions on Robotics and Automation,* vol. 8, no. 3, pp. 313-326, 1992.

[44] S. Sareh, Y. Noh, M. Li, T. Ranzani, H. Liu, and K. Althoefer, "Macrobend optical

sensing for pose measurement in soft robot arms," *Smart Materials and Structures*, vol. 24, no. 12, p. 125024, 2015.

[45] S. C. Ryu and P. E. Dupont, "FBG-based shape sensing tubes for continuum robots," in *Robotics and Automation (ICRA), 2014 IEEE International Conference on*, 2014, pp. 3531-3537: IEEE.

[46] G. Fang, X. Wang, K. Wang, K.-H. Lee, J. D. Ho, H.-C. Fu, D. K. C. Fu, and K.-W. Kwok, "Vision-based online learning kinematic control for soft robots using local gaussian process regression," *IEEE Robotics and Automation Letters*, vol. 4, no. 2, pp. 1194-1201, 2019.

[47] M. C. Yip and D. B. Camarillo, "Model-less feedback control of continuum manipulators in constrained environments," *IEEE Transactions on Robotics*, vol. 30, no. 4, pp. 880-889, 2014.

[48] K. H. Lee, K. C. D. Fu, Z. Guo, Z. Dong, M. C. W. Leong, C. Cheung, P. W. A. Lee, W. Luk, and K. w. Kwok, "MR Safe Robotic Manipulator for MRI-guided Intra-cardiac Catheterization," *IEEE/ASME Transactions on Mechatronics*, vol. PP, no. 99, pp. 1-1, 2018.

[49] Z. Guo, Z. Dong, K.-H. Lee, C. L. Cheung, H.-C. Fu, J. D. Ho, H. He, W.-S. Poon, D. T.-M. Chan, and K.-W. Kwok, "Compact design of a hydraulic driving robot for intra-operative MRI-guided bilateral stereotactic neurosurgery," *IEEE Robotics and Automation Letters*, vol. 3, no. 3, pp. 2515-2522, 2018.

[50] Y. Elsayed, A. Vincensi, C. Lekakou, T. Geng, C. Saaj, T. Ranzani, M. Cianchetti, and A. Menciassi, "Finite element analysis and design optimization of a pneumatically actuating silicone module for robotic surgery applications," *Soft Robotics*, vol. 1, no. 4, pp. 255-262, 2014.

[51] P. Polygerinos, Z. Wang, K. C. Galloway, R. J. Wood, and C. J. Walsh, "Soft robotic glove for combined assistance and at-home rehabilitation," *Robotics and Autonomous Systems*, vol. 73, pp. 135-143, 2015.

[52] H. K. Yap, J. H. Lim, F. Nasrallah, J. C. Goh, and R. C. Yeow, "A soft exoskeleton for hand assistive and rehabilitation application using pneumatic actuators with variable stiffness," in *2015 IEEE international conference on robotics and automation (ICRA)*, 2015, pp. 4967-4972: IEEE.

[53] C. Laschi, B. Mazzolai, and M. Cianchetti, "Soft robotics: Technologies and systems pushing the boundaries of robot abilities," *Sci. Robot.*, vol. 1, no. 1, p. eaah3690, 2016.

[54] J. D. Ho, K.-H. Lee, W. L. Tang, K.-M. Hui, K. Althoefer, J. Lam, and K.-W. Kwok, "Localized online learning-based control of a soft redundant manipulator under variable loading," *Advanced Robotics*, vol. 32, no. 21, pp. 1168-1183, 2018.

[55] G. Sansoni, M. Trebeschi, and F. Docchio, "State-of-the-art and applications of 3D imaging sensors in industry, cultural heritage, medicine, and criminal investigation," *Sensors*, vol. 9, no. 1, pp. 568-601, 2009.

[56] M. Rothermel, K. Wenzel, D. Fritsch, and N. Haala, "SURE: Photogrammetric surface reconstruction from imagery," in *Proceedings LC3D Workshop, Berlin*, 2012, vol. 8, p. 2.

[57] F. Remondino, "Heritage recording and 3D modeling with photogrammetry and 3D scanning," *Remote sensing*, vol. 3, no. 6, pp. 1104-1138, 2011.

[58] F. Saunders, E. Golden, R. D. White, and J. Rife, "Experimental verification of soft-robot gaits evolved using a lumped dynamic model," *Robotica*, vol. 29, no. 6, pp. 823-830, 2011.

[59] P. Polygerinos, K. C. Galloway, E. Savage, M. Herman, K. O'Donnell, and C. J. Walsh, "Soft robotic glove for hand rehabilitation and task specific training," in *2015 IEEE international conference on robotics and automation (ICRA)*, 2015, pp. 2913-2919: IEEE.

[60] H. Huang, J. Chai, X. Tong, and H.-T. Wu, "Leveraging motion capture and 3D scanning for high-fidelity facial performance acquisition," in *ACM Transactions on Graphics (TOG)*, 2011, vol. 30, no. 4, p. 74: ACM.

[61] W. Yuan, S. Dong, and E. H. Adelson, "GelSight: High-Resolution Robot Tactile Sensors for Estimating Geometry and Force," *Sensors (Basel)*, vol. 17, no. 12, Nov 29 2017.

[62] K. Sato, K. Kamiyama, N. Kawakami, and S. Tachi, "Finger-Shaped GelForce: Sensor for Measuring Surface Traction Fields for Robotic Hand," *IEEE Trans Haptics*, vol. 3, no. 1, pp. 37-47, Jan-Mar 2010.

[63] A. Hermanis, R. Cacurs, and M. Greitans, "Acceleration and magnetic sensor network for shape sensing," *IEEE Sensors Journal*, vol. 16, no. 5, pp. 1271-1280, 2016.

[64] A. Hermanis and K. Nesenbergs, "Grid shaped accelerometer network for surface shape recognition," in *Electronics Conference (BEC), 2012 13th Biennial Baltic*, 2012, pp. 203-206: IEEE.

[65] P. Mittendorfer and G. Cheng, "3D surface reconstruction for robotic body parts with artificial skins," in *Intelligent Robots and Systems (IROS), 2012 IEEE/RSJ International Conference on*, 2012, pp. 4505-4510: IEEE.

[66] N. Saguin-Sprynski, L. Jouanet, B. Lacolle, and L. Biard, "Surfaces reconstruction via inertial sensors for monitoring," in *EWSHM-7th European Workshop on Structural Health Monitoring*, 2014.

[67] C. Rendl, D. Kim, S. Fanello, P. Parzer, C. Rhemann, J. Taylor, M. Zirkl, G. Scheipl, T. Rothländer, and M. Haller, "FlexSense: a transparent self-sensing deformable surface," in *Proceedings of the 27th annual ACM symposium on User interface software and technology*, 2014, pp. 129-138: ACM.

[68] Y.-L. Park, B.-R. Chen, and R. J. Wood, "Design and fabrication of soft artificial skin using embedded microchannels and liquid conductors," *IEEE Sensors Journal*, vol. 12, no. 8, pp. 2711-2718, 2012.

[69] J. T. Muth, D. M. Vogt, R. L. Truby, Y. Mengüç, D. B. Kolesky, R. J. Wood, and J. A. Lewis, "Embedded 3D printing of strain sensors within highly stretchable elastomers," *Advanced Materials*, vol. 26, no. 36, pp. 6307-6312, 2014.

[70] V. Wall, G. Zöller, and O. Brock, "A method for sensorizing soft actuators and its application to the RBO hand 2," in *Robotics and Automation (ICRA), 2017 IEEE International Conference on*, 2017, pp. 4965-4970: IEEE.

[71] H.-N. Li, D.-S. Li, and G.-B. Song, "Recent applications of fiber optic sensors to health monitoring in civil engineering," *Engineering structures*, vol. 26, no. 11, pp. 1647-1657, 2004.

[72] G. C. Kahandawa, J. Epaarachchi, H. Wang, and K. Lau, "Use of FBG sensors for SHM in aerospace structures," *Photonic Sensors*, vol. 2, no. 3, pp. 203-214, 2012.

[73] K. O. Hill and G. Meltz, "Fiber Bragg grating technology fundamentals and overview," *Journal of lightwave technology*, vol. 15, no. 8, pp. 1263-1276, 1997.

[74] P. Wei, J. Liu, Z. Dai, and M. Li, "Monitoring the Shape of Satellite Wing Frame Using FBG Sensors in High Electronic Noise, Vacuum, and− 196° C Environment," *IEEE Transactions on Industrial Electronics*, vol. 64, no. 1, pp. 691-700, 2017.

[75] B. A. Childers, M. E. Froggatt, S. G. Allison, T. C. Moore, D. A. Hare, C. F. Batten, and D. C. Jegley, "Use of 3000 Bragg grating strain sensors distributed on four 8-m optical fibers during static load tests of a composite structure," in *Smart*

Structures and Materials 2001: Industrial and Commercial Applications of Smart Structures Technologies, 2001, vol. 4332, pp. 133-143: International Society for Optics and Photonics.

[76] M. Amanzadeh, S. M. Aminossadati, M. S. Kizil, and A. D. Rakić, "Recent Developments in Fibre Optic Shape Sensing," *Measurement*, 2018.

[77] C. Shi, X. Luo, P. Qi, T. Li, S. Song, Z. Najdovski, T. Fukuda, and H. Ren, "Shape sensing techniques for continuum robots in minimally invasive surgery: A survey," *IEEE Transactions on Biomedical Engineering*, vol. 64, no. 8, pp. 1665-1678, 2017.

[78] A. F. da Silva, A. F. Gonçalves, P. M. Mendes, and J. H. Correia, "FBG sensing glove for monitoring hand posture," *IEEE Sensors Journal*, vol. 11, no. 10, pp. 2442-2448, 2011.

[79] L. Xu, J. Ge, J. H. Patel, and M. P. Fok, "3-Dimensional soft shape sensor based on dual-layer orthogonal fiber Bragg grating mesh," in *Optical Fiber Communications Conference and Exhibition (OFC), 2017*, 2017, pp. 1-3: IEEE.

[80] H. Zhang, X. Zhu, Z. Gao, K. Liu, and F. Jiang, "Fiber Bragg grating plate structure shape reconstruction algorithm based on orthogonal curve net," *Journal of Intelligent Material Systems and Structures*, vol. 27, no. 17, pp. 2416-2425, 2016.

[81] S. Rapp, L.-H. Kang, U. C. Mueller, J.-H. Han, and H. Baier, "Dynamic shape estimation by modal approach using fiber Bragg grating strain sensors," in *Sensors and Smart Structures Technologies for Civil, Mechanical, and Aerospace Systems 2007*, 2007, vol. 6529, p. 65293E: International Society for Optics and Photonics.

[82] W. Xiong, C. Cai, and X. Kong, "Instrumentation design for bridge scour monitoring using fiber Bragg grating sensors," *Applied Optics*, vol. 51, no. 5, pp. 547-557, 2012.

[83] M. Kreuzer, "Strain measurement with fiber Bragg grating sensors," *HBM, Darmstadt, S2338-1.0 e*, 2006.

[84] R. Kashyap, *Fiber bragg gratings*. Academic press, 2009.

[85] T. L. T. Lun, K. Wang, J. D. Ho, K.-H. Lee, K. Y. Sze, and K.-W. Kwok, "Real-Time Surface Shape Sensing for Soft and Flexible Structures Using Fiber Bragg Gratings," *IEEE Robotics and Automation Letters*, vol. 4, no. 2, pp. 1454-1461, 2019.

[86] P. Moseley, J. M. Florez, H. A. Sonar, G. Agarwal, W. Curtin, and J. Paik,

"Modeling, design, and development of soft pneumatic actuators with finite element method," *Advanced Engineering Materials*, vol. 18, no. 6, pp. 978-988, 2016.

[87] D. Coric, M. Lai, J. Botsis, A. Luo, and H. G. Limberger, "Distributed strain measurements using fiber Bragg gratings in small-diameter optical fiber and low-coherence reflectometry," *Optics express*, vol. 18, no. 25, pp. 26484-26491, 2010.

[88] C. Shi, S. Giannarou, S.-L. Lee, and G.-Z. Yang, "Simultaneous catheter and environment modeling for trans-catheter aortic valve implantation," in *2014 IEEE/RSJ International Conference on Intelligent Robots and Systems*, 2014, pp. 2024-2029: IEEE.

[89] H. Liu, A. Farvardin, R. Grupp, R. J. Murphy, R. H. Taylor, I. Iordachita, and M. Armand, "Shape tracking of a dexterous continuum manipulator utilizing two large deflection shape sensors," *IEEE sensors journal*, vol. 15, no. 10, pp. 5494-5503, 2015.

[90] Y.-L. Park, S. Elayaperumal, B. Daniel, S. C. Ryu, M. Shin, J. Savall, R. J. Black, B. Moslehi, and M. R. Cutkosky, "Real-time estimation of 3-D needle shape and deflection for MRI-guided interventions," *IEEE/ASME Transactions On Mechatronics*, vol. 15, no. 6, pp. 906-915, 2010.

[91] S. Elayaperumal, J. C. Plata, A. B. Holbrook, Y.-L. Park, K. B. Pauly, B. L. Daniel, and M. R. Cutkosky, "Autonomous real-time interventional scan plane control with a 3-D shape-sensing needle," *IEEE transactions on medical imaging*, vol. 33, no. 11, pp. 2128-2139, 2014.

[92] K. Feng, J. Cui, H. Dang, H. Zhang, S. Zhao, and J. Tan, "Four-cores FBG probe based on capillary self-assembly fabrication technique for 3D measurement," *IEEE Photonics Technology Letters*, vol. 28, no. 21, pp. 2339-2342, 2016.

[93] S. Sefati, F. Alambeigi, I. Iordachita, M. Armand, and R. J. Murphy, "FBG-based large deflection shape sensing of a continuum manipulator: Manufacturing optimization," in *2016 IEEE SENSORS*, 2016, pp. 1-3: IEEE.

[94] C. Ledermann, H. Pauer, H. Woern, M. Seyfried, G. Domann, and H. Wolter, "Using ORMOCER® s as casting material for a 3D shape sensor based on Fiber Bragg gratings," in *2014 IEEE Ninth International Conference on Intelligent Sensors, Sensor Networks and Information Processing (ISSNIP)*, 2014, pp. 1-6: IEEE.

[95] M. Xu, J. Archambault, L. Reekie, and J. Dakin, "Thermally-compensated bending

gauge using surface-mounted fibre gratings," *International Journal of Optoelectronics*, vol. 9, no. 3, pp. 281-283, 1994.

[96] M. Gander, W. MacPherson, R. McBride, J. Jones, L. Zhang, I. Bennion, P. Blanchard, J. Burnett, and A. Greenaway, "Bend measurement using Bragg gratings in multicore fibre," *Electronics Letters*, vol. 36, no. 2, pp. 120-121, 2000.

[97] G. Flockhart, W. MacPherson, J. Barton, J. Jones, L. Zhang, and I. Bennion, "Two-axis bend measurement with Bragg gratings in multicore optical fiber," *Optics letters*, vol. 28, no. 6, pp. 387-389, 2003.

[98] R. Xu, A. Yurkewich, and R. V. Patel, "Curvature, torsion, and force sensing in continuum robots using helically wrapped FBG sensors," *IEEE Robotics and Automation Letters*, vol. 1, no. 2, pp. 1052-1059, 2016.

[99] C. Waltermann, J. Koch, M. Angelmahr, J. Burgmeier, M. Thiel, and W. Schade, "Fiber-optical 3d shape sensing," in *Planar Waveguides and other Confined Geometries*: Springer, 2015, pp. 227-250.

[100] E. M. Lally, M. Reaves, E. Horrell, S. Klute, and M. E. Froggatt, "Fiber optic shape sensing for monitoring of flexible structures," in *Sensors and Smart Structures Technologies for Civil, Mechanical, and Aerospace Systems 2012*, 2012, vol. 8345, p. 83452Y: International Society for Optics and Photonics.

[101] R. G. Duncan and M. T. Raum, "Characterization of a fiber-optic shape and position sensor," in *Smart Structures and Materials 2006: Smart Sensor Monitoring Systems and Applications*, 2006, vol. 6167, p. 616704: International Society for Optics and Photonics.

[102] B. Childlers, D. Gifford, R. Duncan, M. Raum, and M. Vercellino, "Fiber optic position and shape sensing device and method relating thereto," ed: Google Patents, 2006.

[103] J. P. Moore and M. D. Rogge, "Shape sensing using multi-core fiber optic cable and parametric curve solutions," *Optics express*, vol. 20, no. 3, pp. 2967-2973, 2012.

[104] M. D. Rogge and J. P. Moore, "Shape sensing using a multi-core optical fiber having an arbitrary initial shape in the presence of extrinsic forces," ed: Google Patents, 2014.

[105] R. G. Duncan, M. E. Froggatt, S. T. Kreger, R. J. Seeley, D. K. Gifford, A. K. Sang, and M. S. Wolfe, "High-accuracy fiber-optic shape sensing," in *Sensor Systems*

and Networks: Phenomena, Technology, and Applications for NDE and Health Monitoring 2007, 2007, vol. 6530, p. 65301S: International Society for Optics and Photonics.

[106] Z. Dong, Z. Guo, K.-H. Lee, G. Fang, W. L. Tang, H.-C. Chang, D. T. M. Chan, and K.-W. Kwok, "High-Performance Continuous Hydraulic Motor for MR Safe Robotic Teleoperation," *IEEE Robotics and Automation Letters*, vol. 4, no. 2, pp. 1964-1971, 2019.

[107] B. Kim, J. Ha, F. C. Park, and P. E. Dupont, "Optimizing curvature sensor placement for fast, accurate shape sensing of continuum robots," in *2014 IEEE international conference on robotics and automation (ICRA)*, 2014, pp. 5374-5379: IEEE.

[108] H. Moon, J. Jeong, S. Kang, K. Kim, Y.-W. Song, and J. Kim, "Fiber-Bragg-grating-based ultrathin shape sensors displaying single-channel sweeping for minimally invasive surgery," *Optics and Lasers in Engineering*, vol. 59, pp. 50-55, 2014.

[109] H. Yamada and S. Hirose, "Study on the 3D shape of active cord mechanism," in *Proceedings 2006 IEEE International Conference on Robotics and Automation, 2006. ICRA 2006.*, 2006, pp. 2890-2895: IEEE.